Modeling and Analysis of Distortion in Milling of Aerospace Parts

by

Waseem Akhtar

A Dissertation Submitted to the
Graduate School of Sciences and Engineering
in Partial Fulfillment of the Requirements for
the Degree of

Doctor of Philosophy

in

Mechanical Engineering

KOÇ ÜNİVERSİTESİ

September 13, 2023

Modeling and Analysis of Distortion in Milling of Aerospace Parts

Koç University

Graduate School of Sciences and Engineering

This is to certify that I have examined this copy of a doctoral dissertation by

Waseem Akhtar

and have found that it is complete and satisfactory in all respects,

and that any and all revisions required by the final

examining committee have been made.

Committee Members:

Prof. İsmail Lazoğlu, Ph.D. (Advisor)

Prof. Mustafa Bakkal, Ph.D.

Assoc. Prof. Lütfi Taner Tunç, Ph.D.

Assoc. Prof. Arif Karabeyoğlu, Ph.D.

Assist. Prof. Levent Beker, Ph.D.

Date: 13/09/2023

To my Parents

Wife

Daughter (my princess)

and

Son (Ibrahim)

ABSTRACT

Modeling and Analysis of Distortion in Milling of Aerospace Parts
Waseem Akhtar
Doctor of Philosophy in Mechanical Engineering
September 13, 2023

The issue of distortion of parts manufactured by machining is a long-standing problem in the aerospace industry. Especially in the case of large, thin-walled machined structural components, post-machining distortions result in a loss worth billions of dollars to the aerospace industry. Control of distortions is, therefore, very critical to ensure the conformity of these parts and the efficiency of the process. Effective control of the process necessitates efficient models and simulation techniques for predicting distortion of the workpiece after machining. Very high cutting force and temperature loads generated during machining affect the workpiece in several ways. These cutting loads are dictated by the parameters of machining and the material characteristics of the cutting tool and the workpiece. Moreover, the initial stress of the blank also dictates the distortion behavior. Accurate modeling of all these factors is crucial to the precise prediction of distortion of the workpiece.

Milling is a very important process for the machining of aerospace parts. In this thesis, modeling of the milling process is carried out for efficient prediction of various aspects of the process. A novel analytical algorithm is proposed to predict the cutting temperature of the workpiece. The proposed algorithm allows accurate calculation of the workpiece temperature by duly incorporating the drop in temperature of the workpiece during the non-engagement periods of the cutting tool. Another novel contribution of this thesis is developing a hybrid FEM-analytical model for predicting distortions of machined thin-walled parts. The model considers loads due to cutting as well as the effect of the initial bulk residual stresses of the material. The measurement of the initial stresses of the material is carried out by the crack compliance method, whereas machining-induced loads are calculated analytically. A novel strategy is devised to incorporate these loads in a FEM model. The results of the proposed models are validated with machining experiments. Another

contribution of this thesis is the development of a novel method for monitoring of the machining process using a low-cost infrared sensor. Three critical aspects of the machining process, i.e., tool wear, chatter, and workpiece deformations, are detected using a single infrared sensor. Different signal processing techniques are applied in time and frequency domains to analyze the data collected from the sensor. The results of the proposed method are verified by carrying out machining experiments.

ÖZETÇE

Doktora Tez Başlığı
Waseem Akhtar
Mechanical Mühendisliği, Doktora
13 Eylül 2023

Hassas işlenmiş parçaların çarpılması, havacılık ve uzay endüstrisinde yaygın karşılaşılan önemli problemlerdendir. Özellikle, büyük ve ince kalınlığa sahip yapısal parçalarda talaşlı İmalat sonrasında yaşanan çarpılmalar havacılık ve uzay enüstrisinde milyarlarca dolarlık zarara sebep olmaktadır. Çarpılmaların kontrolü, bu parçaların kalitesini ve sürecin verimliliğini sağlamak için çok önemlidir. Üretim işleminin etkili kontrolü, işleme sonrasında iş parçasındaki çarpılmayı tahmin etmek için verimli modeller ve simülasyon teknikleri gerektirir. İşleme sırasında oluşan çok yüksek kesme kuvveti ve sıcaklık yükleri, iş parçasını çeşitli şekillerde etkiler. Bu kesme yükleri, iş parçasının ve takımın malzemesinin kesme parametreleri ve özellikleri ile doğrudan ilişkilidir. Ayrıca, iş parçası malzemesinin ilk gerilim durumu da çarpılma davranışını belirler. Tüm bu faktörlerin doğru bir şekilde modellenmesi, iş parçasının çarpılmasını kesin olarak tahmin edilmesi için çok önemlidir.
Frezeleme, havacılık ve uzay endüstrisindeki parçalarının işlenmesi için çok önemli bir süreçtir. Bu doktora tezinde, sürecin çeşitli yönlerinin verimli bir şekilde tahmin edilmesi için freze işleminin modellenmesi gerçekleştirilmiştir. İş parçasının kesme sıcaklığını öngörmek için yeni bir analitik algoritma önerilmiştir. Önerilen algoritma, kesici takımın devrede olmadığı zamanlarda iş parçasının sıcaklığındaki düşüşü usulüne uygun olarak dahil ederek iş parçası sıcaklığının doğru hesaplanmasına olanak tanır. Bu tezin bir başka yeni katkısı, ince duvarlı iş parçalarının işlenmesindeki çarpılmaları tahmin etmek için hibrit bir FEM-analitik modeli geliştirmektir. Model, kesme yüklerinin etkisinin yanı sıra malzemenin başlangıçtaki toplu artık gerilmelerini de göz önünde bulundurur. Malzemenin başlangıç gerilmeleri, çatlak uyma yöntemi kullanılarak ölçülürken, talaşlı imalattan kaynaklanan yükler analitik olarak hesaplanır. Bu yükleri bir FEM modeline dahil etmek için yeni bir strateji tasarlanmıştır. Önerilen modellerin sonuçları talaşlı üretim deneyleri ile doğrulanmıştır.

Bu tezin bir diğer katkısı, düşük maliyetli bir kızılötesi sensör kullanarak işleme sürecinin izlenmesi için yeni bir yöntemin geliştirilmesidir. İşleme sürecinin üç kritik yönü yani takım aşınması, tırlama ve iş parçası deformasyonları, tek bir kızılötesi sensör kullanılarak tespit edilir. Sensörden toplanan verileri analiz etmek için zaman ve frekans alanlarında farklı sinyal işleme teknikleri uygulanmaktadır. Önerilen yöntemin sonuçları talaşlı imalat deneyleri yapılarak doğrulanmıştır.

ACKNOWLEDGMENTS

This journey, marked by countless hours of research, self-discovery, and growth, would not have been possible without the unwavering support and encouragement from a multitude of individuals who have enriched my path to completing this Ph.D. thesis. First and foremost, I extend my deepest gratitude to my advisor, Prof. Ismail Lazoğlu, for his invaluable guidance, patience, and expertise. His mentorship has been a beacon of light, illuminating my way through the complexities of research.

I am indebted to the members of my thesis committee, Prof. Mustafa Bakkal, Assoc. Prof. Lütfi Taner Tunç, Assoc. Prof. Arif Karabeyoğlu and Assist. Prof. Levent Beker, for their insightful feedback, rigorous assessments, and for challenging me to push the boundaries of my work. Your collective expertise elevated the quality of this work and broadened its horizons. My sincere appreciation goes to all my colleagues and fellow researchers at the Manufacturing and Automation Research Center (MARC), especially Dr. Anjum Malik, Dr. Shaheryar Khan, Dr. Mostafa Saleh, Dr. Ehsan Layegh, Shams Torabnia, Pooya Pashak, Berkay Demiryulek, Cemile Besirova, and our lab engineer Muzaffar Butun, who provided a stimulating environment for intellectual exchange and camaraderie. The discussions and debates we shared were instrumental in refining my ideas and expanding my horizons. I wish to extend a special acknowledgment to Hammad ur Rahman for his unwavering dedication, insightful conversations, and priceless contributions.

My heartfelt gratitude goes to my late father, as well as my mother and siblings, for their unwavering love, encouragement, and understanding. Most importantly, to my wife, daughter, and son for their unending love, patience, and sacrifice – thank you for standing by me throughout this arduous journey. Your belief in me has been my driving force. I dedicate this thesis to you.

Last but not least, I extend my heartfelt thanks to all the friends who offered their moral support and encouragement. Your presence in my life brought moments of respite and joy, reminding me of the importance of balance in this academic endeavor. This thesis is a testament to the collective efforts of many, and while their names may not all be mentioned here, their impact is embedded in every word written and every discovery made. To each person who has played a part in this journey, I offer my deepest appreciation.

TABLE OF CONTENTS

LIST OF TABLES

LIST OF FIGURES

ABBREVIATIONS

x, z	x, z coordinates
l_s	Length of shear plane
k_{wp}	Thermal conductivity of the workpiece
a_{wp}	Thermal diffusivity of the workpiece
K_0	Modified Bessels function of 2nd kind zero-order
da_p	Discretized axial depth of cut
V	Cutting velocity
ϕ_n	Normal shear angle in oblique cutting
D	Tool diameter
ϕ_w	Current immersion angle
β	Helix angle of the tool
q_{shear}	Intensity of shear heat source
q_{pl}	Intensity of plowing heat source
dF_t, dF_r and dF_a	Discretized tangential, radial, and axial forces due to shearing
K_{tc}, K_{rc} and K_{ac}	Coefficients for tangential, radial, and axial cutting forces
K_{te}, K_{re}	Edge coefficients for forces in cutting and radial direction
h_c	Uncut chip thickness
f_t	Feed per tooth
ϕ_i	Oblique shear angle
α_n	Normal rake angle
l_p	Length of plowing heat source
P_{cut}	Plowing force in cutting velocity direction
P_{thr}	Plowing force in thrust direction
h_p	Heat partitioning ratio for plowing heat source

ρ_{wp}	Density of the workpiece material
c_{wp}	Specific heat capacity of the workpiece material
k_t	Thermal conductivity of the tool material
ρ_t	Density of the tool material
c_t	Specific heat capacity of the tool material
τ	Time constant of the system
a_p	Axial depth of cut
δ	Wall thickness of the workpiece
n	Spindle speed
a_e	Radial depth of cut
N	Number of cutting edges
ϕ_p	cutter pitch angle
$\Delta\theta_{\text{fine}}$	Angular increment fine
$\Delta\theta_{\text{coarse}}$	Angular increment coarse
L	Length of sample
B	Width of sample
t	Thickness of sample
a	Depth of slit
w	Width of slit
l	Gauge length
s	Distance between slitting plane and center of the strain gauge
$\sigma(x)$	Normal component of stress for slit depth a
$\epsilon(a)$	Strain measured at slit depth a
a	Depth of slit
$P_j(x)$	Legendre polynomial functions at depth x
A_j	coefficients of terms of Legendre polynomial
x	Depth of strain measurement
j	Order of the polynomial

m	Highest order of the polynomial
C	Compliance matrix
C_{ij}	Element of compliance matrix
ϵ	Strain measured at strain gauge location
a_i	Slit depth
σ	Stress corresponding to a single term of Legendre polynomial
P_j	Term of Legendre polynomial
$\{A\}$	Vector of coefficients
$\{\epsilon_{meas}\}$	Vector of measured strains
$[C]$	Compliance matrix
WEDM	Wire electric discharge machining
f_z	Feed per tooth
θ	Immersion angle of the tool
$\dot{Q}_s$	Shearing power
$\dot{Q}_f$	Friction power
$\dot{Q}_{pl}$	Ploughing power
$\dot{Q}_T$	Total power due to cutting
H_m	Mean value of surface heat flux
P_m	Mean value of surface pressure
l	Width of the moving load source
θ_{st}	Tool immersion angles at the start
θ_m	Tool immersion angles in middle
θ_{ex}	Tool immersion angles at the exit
F_s	Shear force on shear plane
F_u	Friction force on rake face
F_{tc}	Tangential cutting force
F_{rc}	Radial cutting force
F_{ac}	Axial cutting force

F_R	Resultant cutting force
V_s	Shear velocity
V_c	Chip velocity
V	Cutting velocity
τ_s	Average shear flow stress
α_n	Normal rake angle
ϕ_n	Normal shear angle
ϕ_i	Oblique shear angle
h_s	The heat partitioning ratio due to shearing
L	Lenght of the projection of the arc of engagement
P_m	Mean cutting pressure
H_m	Mean heat flux
α	Coefficient of thermal expansion
E	Modulus of elasticity
ν	Poisson's ratio
$\varDelta$	Measured deflection
v	IR sensor voltage
a, b, c	Coefficients of the correlation function
CAD	Computer aided design
CAM	Computer-aided manufacturing
CNC	Computer numeric control
FEM	Finite element method
IBRS	Initial bulk residual stresses
MIRS	Macining induced residual stresses
Al	Aluminum
FE	Finite element
XRD	X-ray diffraction
XFEM	Extended FEM

GOM	Geometrical optical measurement
3D	3 dimensional
SECM	Spring element constraint method
ANN	Artificial neural network
MLRM	multi-layer removal method
CFRP	Carbon fiber reinforced plastics
ALE	Arbitrary Lagrangian-Eulerian
SHPB	Split Hopkinson pressure bar
PCD	Polycrystalline diamond
RSM	Response surface method
FDM	Finite difference method
DSLD	Dynamic stability lobe diagram
CNN	Conventional neural network
RNN	Recurrent neural network
ms	Millisecond
m/min	Meter per minute
mm	Millimeter
μm	Micrometer
W/mK	Watt per meter per kelvin
AI	Artificial intelligence
AE	Acoustic emission
HHT	Hilbert Huang transform
CES	Curved edge sensor
VMD	Variational mode decomposition
WPD	Wavelet packet decomposition
CMM	Coordinate measuring machine
IR	Infrared sensor
FFT	Fast Fourier transform

SRF	Spindle rotation frequency
TPF	Tooth passing frequency

Chapter 1

PREDICTION AND CONTROL OF DISTORTIONS IN THE MACHINING OF AEROSPACE PARTS: LITERATURE REVIEW

1.1 Overview

One of the big challenges of the industries manufacturing aerospace components is the distortion of machined thin-walled parts. Significant resources are wasted annually due to distortion-related rejections of the parts. Therefore, accurate prediction and distortion control are essential to prevent substantial time and financial losses. Avoiding these distortions is difficult because of the machining process's complicated dynamics and the unpredictability of bulk material fabrication processes. Numerous investigations have been conducted on this matter; nonetheless, achieving full control of the machining process and, hence, machining distortions seems an uphill task. To determine the advancements in the field and emphasize the present limits of the area, earlier works on the subject are examined in this chapter. Fundamental mechanisms that cause the machined parts' distortions are recognized, and current techniques to mitigate these distortions are examined. It is observed that initial bulk residual stresses and stresses induced due to the cutting process are the leading causes of distortions in aerospace parts. In addition, static deflection of the cutting tool and workpiece also influences the sizes of the machined parts. Each of these different mechanisms plays its role in the distortion of machined thin-walled parts. The main reason for the distortion of parts during the roughing operation is the initial bulk residual stress redistribution. In the case of finishing operations of thin-walled parts, machining-induced stress, and static workpiece deflections are found to dominate.

All of these mechanisms need to be considered during process planning for implementing effective, adequate measures for distortion control. Application of deep learning-based process optimization techniques, use of adaptive fixtures, in-process part-shape-based error control, and optimization of the toolpath and part location in the blank considering the profile of the initial bulk residual stresses are recognized as ensuring options for control of distortions for machined parts. However, a few related obstacles must be solved before the appropriate adoption of these measures.

1.2 Introduction

Modern aerospace designs have undergone a paradigm change as a result of advancements in computer-aided design (CAD), computer-aided manufacturing (CAM), and precision machine tool technologies. These technological developments have made it possible to replace assemblies or sub-assemblies of old designs with single parts having better structural characteristics. Thanks to the modern CNC (computer numeric control) multi-axis machining centers, the precise machining parts having profiled shapes has also become a regular activity. However, manufacturing ultra-precision components for contemporary aerospace designs still presents difficulties, and many completed or semi-finished components must be discarded because of machining process-related non-conformances.

It is well acknowledged that the aerospace industry suffers losses of up to billions of dollars as a result of machining distortions of aircraft parts. Research by Boeing [37] found that the cost of rejections and reworks attributable to component distortions for four separate aircraft programs was 290 million USD. Another analysis [6] states that the German manufacturing industry spends 850 million euros annually on expenditures connected to part distortions. Most machining part distortions occur during the semi-finishing and finishing steps. Before the final finishing stage, a typical aerospace component goes through a number of processes, including rolling, forging, heat treatment, etc. The distortion-related rejection of the components at the final finishing step results in a significant time and financial loss. Therefore, it is required to enhance the regulation of the machining process to prevent distortions and consequential loss of resources.

The machining process has complex dynamics that depend on factors related to the machining parameters, workpiece material, and machining environment. Due to this complex nature of the machining process, controlling distortions of machined parts is quite challenging. Much research has been conducted to investigate the reasons for machining distortions and provide efficient prediction and control solutions. A comprehensive review of these investigations is provided in the sections that follow. Each study has attempted to identify and address one or more sources of machining distortions. From the reviewed literature, the most critical processes causing part distortions are determined. The state of the art is then determined by summarizing the works on these methodologies. Each of these mechanisms has a discussion part where the research achievements and present limitations are highlighted.

1.3 Mechanisms of distortion of machined parts

Research on distortion prediction and control may be categorized into two main categories: (i) based on distortion mechanisms, and (ii) based on analysis techniques, such as finite element method (FEM), analytical, statistical, etc., [38]. The first categorization is focussed in this investigation. The following primary mechanisms of distortions/deviation in sizes and their control might be noticed from the thorough analysis of the literature:

- Initial bulk residual stresses (IBRS)
- Machining induced residual stresses (MIRS)
- The combined effect of IBRS and MIRS
- Static deflection of tool and workpiece
- Miscellaneous factors

1.3.1 Initial bulk residual stresses (IBRS)

Initial bulk residual stresses are the inherent stresses in blanks caused its previous processing. Casting, rolling, extrusion, forging, and quenching are the most common processing techniques for machining blanks. During these operations, the material is subjected to complicated thermo-mechanical loading and metallurgical changes, causing residual stresses. Although stress-relieving procedures are frequently performed after these production processes, it is unlikely to reach a stress-free condition [7]. In the machining of thin-walled aerospace components, almost 90 to 95% of the workpiece blank is removed. This massive amount of material removal disrupts the existing state of stress balance in the blank, leading to distortion of the part once it is removed from the fixture. The primary reason for these distortions of parts in the aerospace sector is the IBRS, as mentioned by [3]. IBRS has also been cited as the primary reason for distortion of machined thin-walled parts in a number of other studies such as [8, 10, 12, 39–43].

Different production techniques lead to different stress profiles in the material. Figure 1.1 shows a typical initial stress distribution within an aluminum blank as a result of its prior production history. Initially, the machining blank has a stress balance condition characterized by the uniform distribution of the stresses inside it. On machining a specific region "M" from the blank, the stresses in the cut section (illustrated with the blue-colored curve) are eliminated, as described in Figure 1.2 disrupting the stress balance within the remaining blank. This unstable stress imbalance leads to a quick redistribution of stresses to create a new equilibrium state. In most instances, the part's shape changes in tandem with this new condition of stress. This section discusses multiple research approaches that identified IBRS as the primary contributor to part distortions.

Wei and Wang [39] examined the impact of initial blank stress redistribution on deflections of a machined thin-walled aerospace component. To observe the deflection of the aluminum alloy Al 7050-T7451, FEM simulations were performed. It was supposed that IBRS were symmetric around the part's midplane and that every plane parallel to it had an identical value. Simulated findings were contrasted

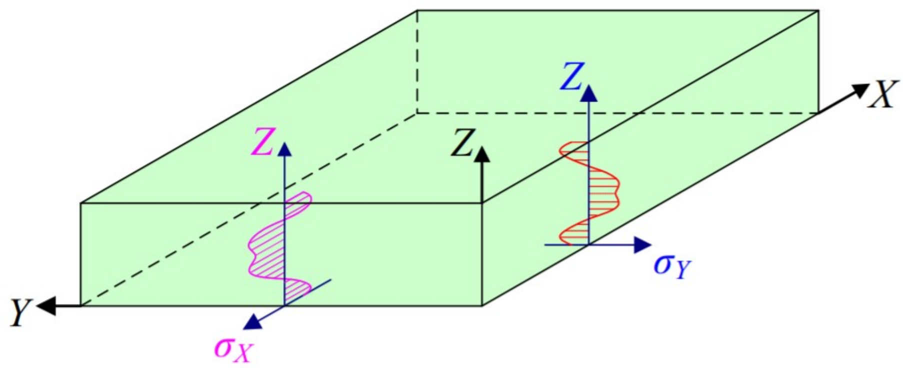

Figure 1.1: Typical distribution of stresses in an aluminum workpiece [2].

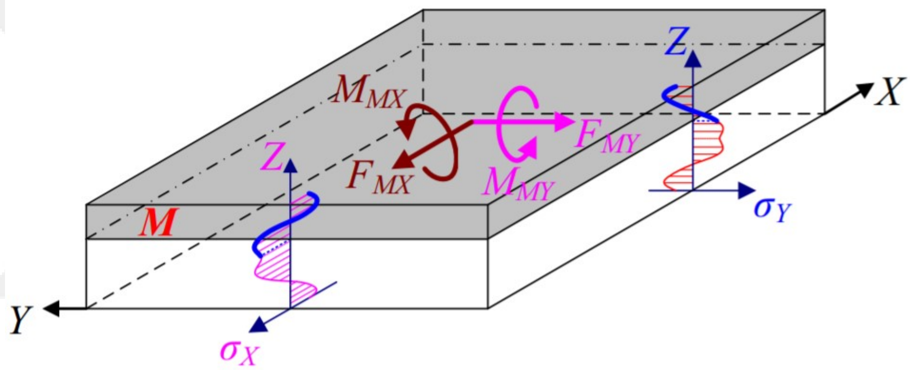

Figure 1.2: Release of stresses due to material removal [2].

with those from experiments. The findings demonstrated that IBRS significantly impacted the machined part's deflections.

To reduce component distortion caused by the redistribution of initial stresses due to the rolling process, Chantzis et al. [3] presented an industrial procedure. The proposed methodology involved the analytical calculation of initial stresses from the observed component distortions by using a linear elastic model. After each layer removal, component distortions were measured using a machine probe and a linear displacement sensor. The part model was then subjected to residual stresses fitted with a sum-of-cosines function and applied longitudinally and transversely. Based on the identified residual stress profile, the best location for the part inside the blank to produce minimal distortions was determined as shown in Figure 1.3. The usage of the simulation approach by a shop floor technician was envisioned during its development. It was, however noted that the approach needed to be improved for a more accurate specification of the boundary conditions related to the process as well as for the phenomenon of material removal.

For the alloy Al 7050-T7451, Zhang et al. [4] examined the impact of IBRS on

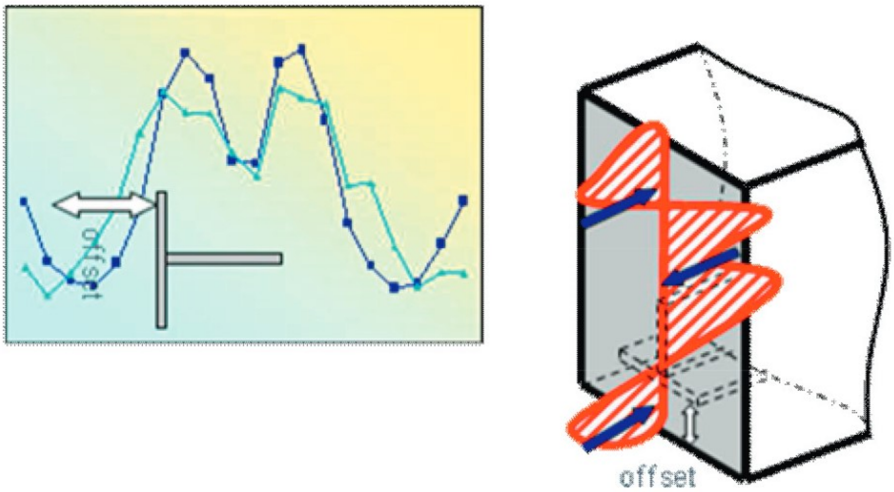

Figure 1.3: Optimization of part location in the blank [3].

part distortions. To determine part deformation caused by stress redistributions, contour method and layer removal techniques were employed. Commercial software MSC MARC was used to determine measured part deformation-based 2D stress distribution. The findings demonstrated that the redistribution of IBRS impacted part distortions. Based on the blank's stress profile, as shown in Figure 1.4, the optimal part layout in the blank was discovered.

For estimating the residual stress profile of Al 7075-T651, Dreier and Denkena [5] presented an approach based on layer removal. As demonstrated in the setup used for the experiment in Figure 1.5, the machine probe was utilized to detect component deflections as opposed to the traditional layer removal approach, which uses strain gauges. The Bernoulli beam theory was then applied to convert the measured deflections into residual stresses. Layers (of 1 mm thick) were removed using the milling process. Stresses due to the machining of layers were measured using the

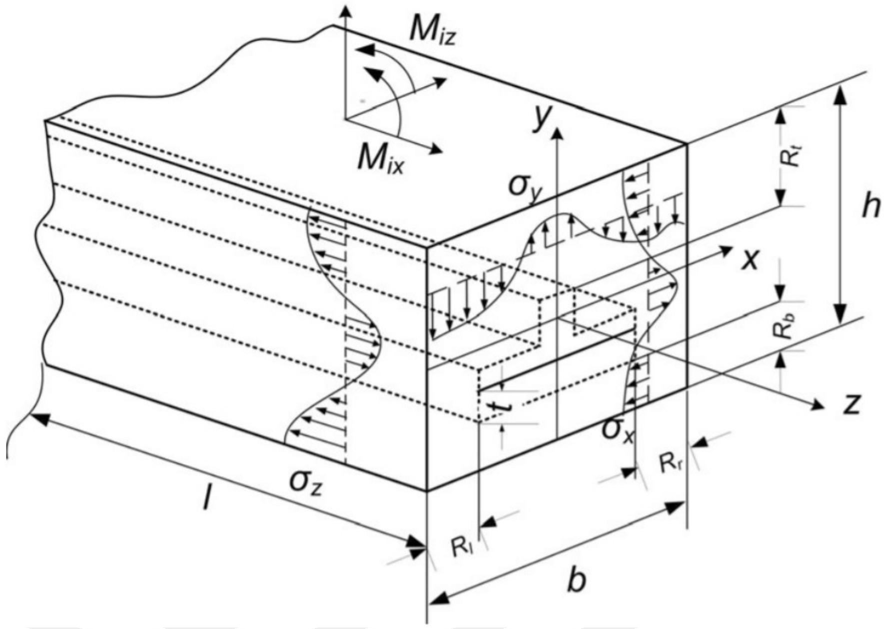

Figure 1.4: Part location optimization [4].

technique of x-ray diffraction (XRD) and incorporated into the FEM model to get the IBRS profile of the blank.

Based on level set extended-FEM (XFEM) theory, L. D'Alvise et al. [6] suggested

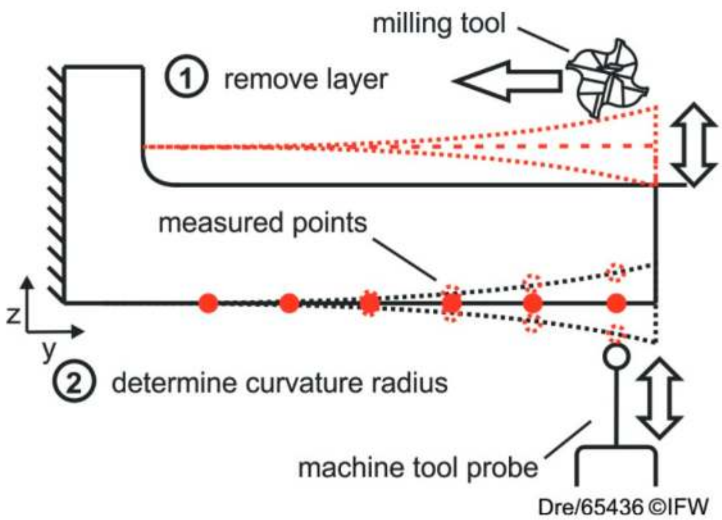

Figure 1.5: Setup for proposed layer removal based method [5].

a technique to predict part deformities resulting from redistribution of IBRS in the milling process. The suggested approach is summarized in the Figure 1.6. The need to re-mesh the entire workpiece following each cut pass was avoided, thanks to XFEM based on level-set; the surface layer needed to be re-meshed only. Significant computational efficiency was attained by avoiding re-meshing thoroughly after each cutting run. Validation of the proposed method was carried out on Al 2024-T3 aerospace components. Given the part's 50 mm thickness, the impact of MIRS that typically evolve within a very shallow depth (a few hundred micrometers (μm) from the surface) was disregarded, and only the IBRS redistribution mechanism was considered.

Cerutti and Mocellin [7] came up with a FEM method for predicting part dis-

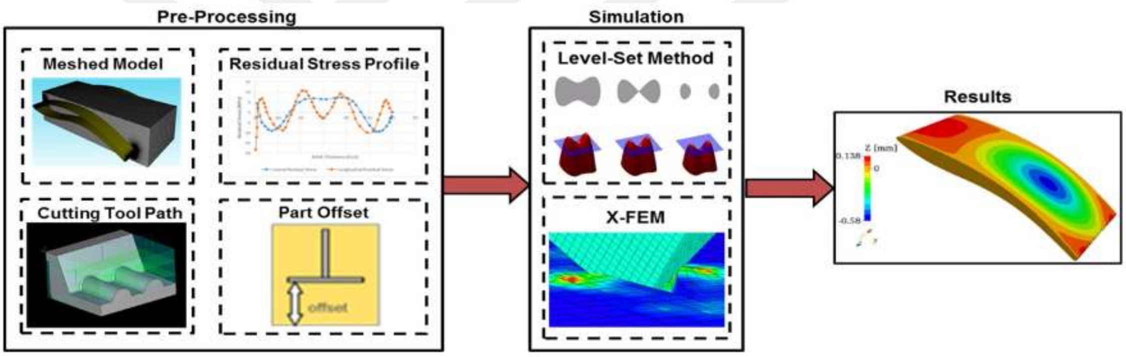

Figure 1.6: Overview of the deformation prediction method [6].

tortion driven by IBRS redistribution. The numerical modeling of the process on the Al 2050-T84 part was carried out using FORGE software. For material removal, a Boolean operation-based adaptive re-meshing approach was used. As seen in Figure 1.7, the material was removed in accordance with the direction of the node's distance from the cut border. Following each cutting operation or pass, the part's actual deformed geometry was taken into account for removal in the following phase. To increase the performance of parallel calculations, mesh partitioning was also done in cores. Based on the premise that machining-induced stresses had very little impact on distortions of components with a wall thickness of more than 5 mm, and considering their shallow penetration depth of 200–250 μm, these stresses were ignored.

For the Al 7050-T651 workpiece, Llanos et al. [44] developed an agile analytical

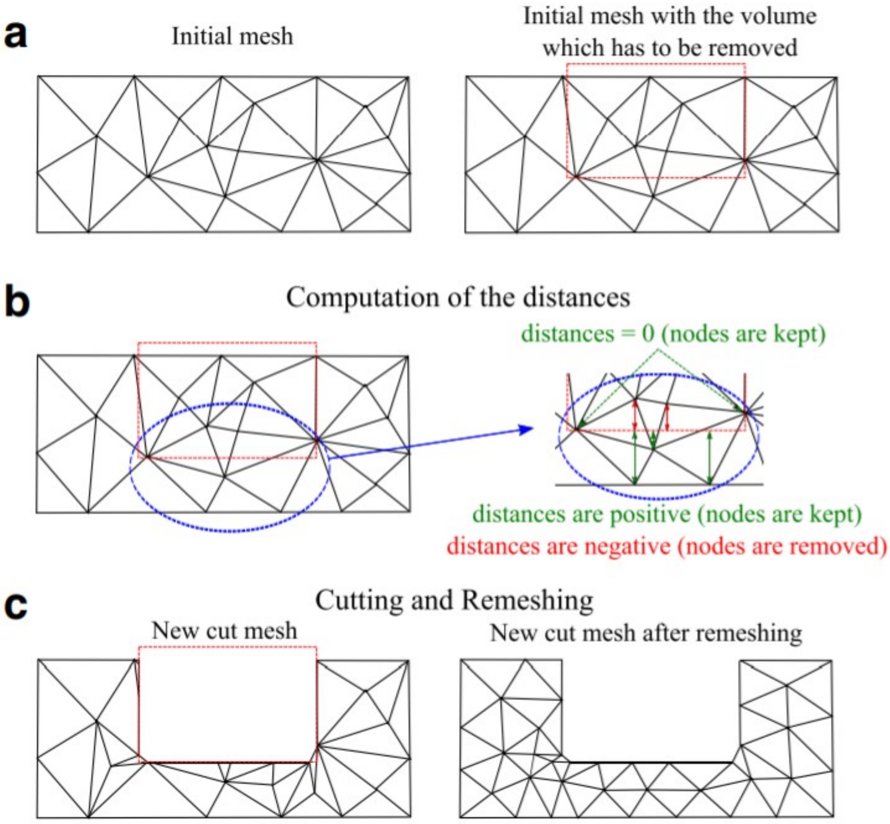

Figure 1.7: Steps for removing large material using the proposed method [7].

model for identifying part distortions caused by IBRS. The stresses and distortions only in the longitudinal direction of the blank were addressed. The measurement of stresses was based on the measurement of part curvature during the layer removal process. Euler-Bernoulli beam theory was then used to determine part distortions from the determined stresses. Further validations are needed to support the validity of this approach, which neglects the stresses in the transverse direction. Values of the distortion assessment were reported close to the experimental findings.

Saleem et al. [8] investigated the impact of initial stress redistribution during machining stages for Al 7075-T6 using part distortion models in Ansys. The initial stresses due to quenching heat treatment were also determined by FEM simulations, as shown in Figure 1.8. The simulated results of stress redistribution during layer removal were compared with milling trials. The element deactivation method was employed to mimic the removal of material via machining. It was discovered that the predicted distortions were larger as compared to the experimental values. This discrepancy was linked to the simplified model assumptions for cutting and disregarding the clamping forces.

A semi-analytical method for the prediction of part deformation was presented by

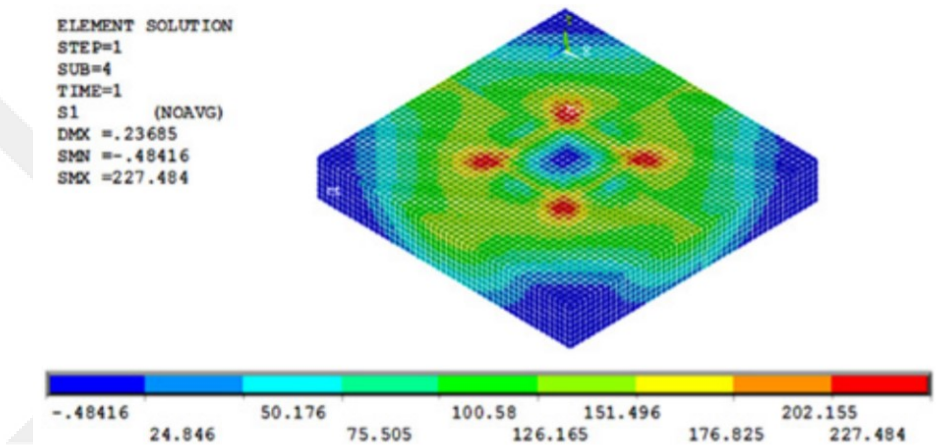

Figure 1.8: Simulation of residual stresses due to quenching process [8].

Gao et al. [45]. The impacts of IBRS and the bending stiffness of the workpiece were integrated into the model derived from the static theory of plates. Due to its assumptions, the proposed model was stated to be only suitable for the prediction of deformation under bending of thin-walled components machined from rectangular-shaped workpieces under large removal rates (in excess of 60% in each layer). Chen et al. [46] also used an analytical model built on the bending theory of plates and shells to estimate the deformation of the Al 7075-T651 multi-frame component. The model ignored the cutting loads while accounting for the redistribution of IBRS during material removal. A noteworthy phenomenon of time-varying IBRS redistribution and accompanying part distortion after machining was described. Varying distortion values for different process sequences were also noted. The distortion of a cylinder turn machined from an Al 2219 alloy rolled ring was predicted by Xue et al. [47]. A mathematical model that takes the impact of IBRS into account was given. IBRS caused by rolling was simulated using the SIMUFACT 13.2 program, and the hole drilling method was used for the measurement of these stresses. The results of analytical prediction of deformation were compared with deformation analysis in Ansys.

Werke et al. [9] performed a simulation-based distortion study of an aerospace part of a nickel-based alloy. By employing geometric optical measurement (GOM), out-of-plane deformations were initially measured by cutting planar sections at specified distances as indicated in Figure 1.9. The stress values within the sections were mapped using the stresses that were measured at the location of the cut sections. A numerical iterative method for estimating 3D (3-dimensional) stresses was also put forth. Distortion of the part in 3D was obtained by spring-back calculations, and the impact of several parameters, such as component position inside the workpiece and component shape modification, was analyzed. Ignoring machining-induced distortions was attributed to the 25% disparity between simulated and measured distortion.

A machining distortion model was implemented by Bilkhu et al. [48] to study

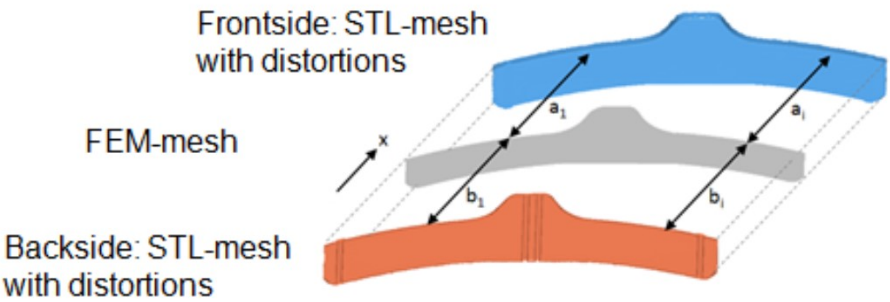

Figure 1.9: Determination of stresses based on GOM and the contour method [9].

the impact of redistributing non-symmetrical initial stresses in the machining of a part of Al 7050. Newton-Raphson and Lagrangian incremental techniques were used with an elastic-plastic heat treatment model to create non-symmetrical profiles of residual stresses. Machining stresses and resulting distortion were simulated in

DEFORM. While the part distortion assessments differed by up to 42%, the findings of asymmetrical residual stresses had a difference of 28% from the experimental measurements. The unreliability in the stress distribution prediction framework was cited as the reason for the difference in the findings.

When cutting AISI 316 stainless steel, Cherif et al. [49] analyzed the effects of changing the depth of cut, clamping force, and toolpath sequence on part deformation. IBRS were measured using neutron diffraction and layer removal methods, whilst FEM and Kistler load washers were used to estimate clamping forces. The 3D model for part distortions was created with the help of the SYSWELD program. Their findings demonstrated that the depth of cut and toolpath sequencing influenced the redistribution of initial strains and, therefore, part deformation.

Zhang et al. [41] developed a control technique for deformation due to the redistribution of IBRS. An adaptive fixture was used for the machining of the Ti6Al4V alloy part. The forces at several clamping sites of the fixture were measured to determine the part's in-process deformation. The distortions of the part were then predicted using the estimated forces as input in the Abaqus model. The choice was made to continue machining, to unclamp and release the stresses, or to adjust the clamping force based on the anticipated distortions. The technology was demonstrated to be effective in reducing blade part distortions. The drawback of this approach was the demand for a unique fixture for every part. Additionally, cutting forces and temperatures had little impact on how residual stresses evolved. The usefulness of this approach has to be further supported as distortions in the y direction were only considered moreover; the approach needs to be tried on complicated geometries.

Li et al. [10] analyzed the impact of finishing allowance and IBRS on the distortion of the Al 7050-T7451 alloy component. For the purpose of calculating initial residual stresses, the crack compliance approach was adopted. A distortion model was built in Abaqus, where the initial stress profile was applied after fitting it with a six-peak Gaussian function. The effect of various finishing allowance values was studied, and a Simplex algorithm-based linear model was used for optimizing the finishing allowance at the end. As may be seen in Figure 1.10, there was a significant decrease in component distortions.

Using Al 7075-T6 as their test material, Song et al. [42] investigated the effec-

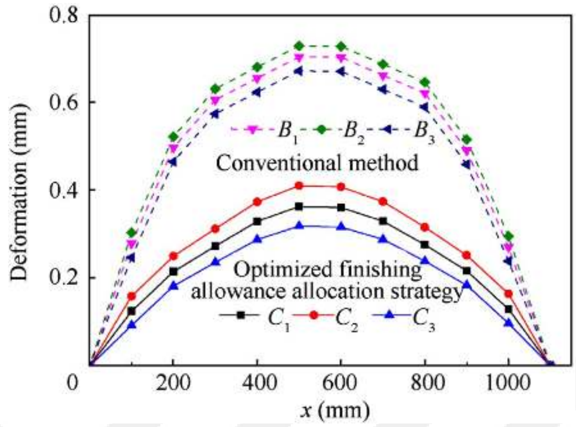

Figure 1.10: Reduction of distortion by optimization of finishing allowance [10].

tiveness of controlling distortions based on IBRS. A low-stiffness spring element constraint method (SECM) was employed instead of the 3-2-1 constraint principle for defining the boundary conditions related to the clamping of the machined part. FEM was utilized to simulate component deformation, whilst layer removal and hole drilling were employed to assess IBRS. In contrast to the 3-2-1 principle, their findings showed that the SECM better represented the actual boundary conditions.

Barcenas et al. [50] optimized the component location within the blank while taking into account the determined IBRS profile of the blank of Al 7050-T7451. The IBRS were experimentally determined using the multi-layer removal technique (MLRM). The sum-of-cosines function was used to fit the measured stress data. The calculated residual stress distribution was then defined in an FE model of part deformation built in the Calculix software. After establishing the FE model, the part's distortions were examined by altering its location within the blank in the z (workpiece depth) direction. For a typical aircraft rib, optimal part arrangement within the blank was found using FEM analysis.

For Al 7075-T651 parts, Casuso et al. [43] used the extended-finite-element-method (XFEM) employing the theory of level-set to model distortions caused by the IBRS and machining process. The close-to-surface IBRS were measured using the hole drilling method, and the stresses in the workpiece depth (z-direction) were extrapolated using a cubic spline function. The cosinusoidal function was then used to match the stresses observed in the planar (x and y) axes. Virfac® Machining was used as the interface for the MORFEO software employed to conduct XFEM analysis. The findings of distortion prediction using the suggested approach deviated by a scale of 10 from experimentally determined values. As a result, only a qualitative understanding of the connection between process sequence and distortions was achieved. The disparity in findings was ascribed to potential errors in the measurements of IBRS.

Haichao et al. [2] estimated the distortions of the machined part due to IBRS by employing static bending stress formulations. An Al 7075-T7451 part was used for the investigation. A numerical approach was created for optimizing part position inside the blank. Part distortions were observed to decrease by 99.79% when the component was located using the suggested step reduction iterative solution approach as opposed to the widely utilized mid-position strategy. Furthermore, it was discovered that the part distortion simulation findings were within 20% of the experimental results.

To minimize distortions of a machined part of Al 7050-T7451, Rodrguez-Sánchez et al. [11] took into account IBRS and part position in the blank. Figure 1.11 illustrates the scheme mapping of IBRS and locating of part in the blank. Artificial neural networks (ANN) were employed to build a model that linked distortions with the part location and stress. The Ansys APDL-based FEM simulation of the distortions provided the part distortions data needed for ANN training. The FE model was given the profile of the IBRS as input to calculate distortion. The positioning of the component inside the blank was then optimized using simulated annealing and ANN. Workpiece distortions were predicted to be within 3%, and the reduction in distortions was claimed to be as much as 80%.

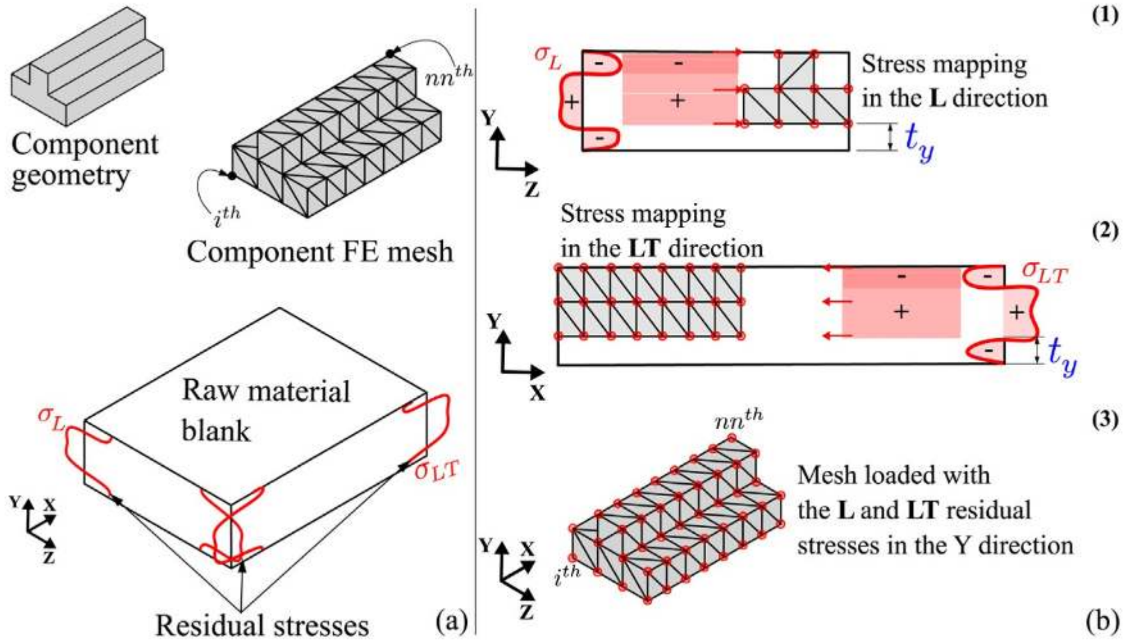

Figure 1.11: Method of stress mapping: (a) raw blank and meshed model of the component, and (b) methodology of stress mapping [11].

Discussion on IBRS Mechanism

From the literature reviewed above, it is clear that redistribution of IBRS plays a substantial role in the distortions of thin-walled machined parts. IBRS dominates the distortion phenomenon, particularly in components machined from aluminum alloys. It is thus crucial to characterize and regulate these stresses to anticipate and avoid distortions of aerospace parts. Different material production techniques, e.g., rolling, forging, quenching, etc., leave different stresses due to different thermomechanical loadings. Figure 1.12 and Figure 1.13 show typical stress profiles ("M"-shaped) that were the result of the rolling process carried out on two distinct aluminum alloys.

The layer removal approach was most often used to determine IBRS profiles practically. Less often used methods include those that can measure deep into the part, including synchrotron radiation, neutron diffraction, ultrasonic method, magnetic technique, and deep hole drilling. The first three suffer from a relative lack of availability of highly specialized equipment, while the latter two suffer from limited depth

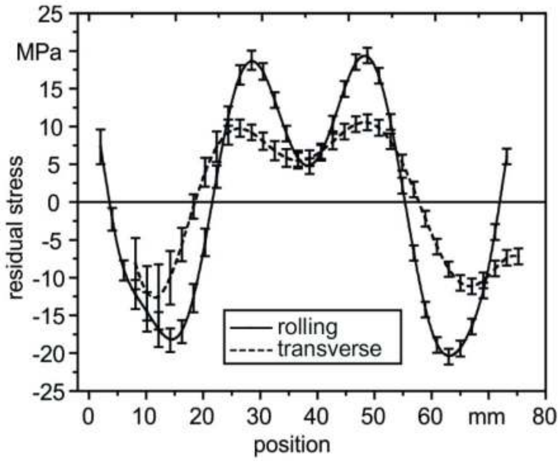

Figure 1.12: IBRS profile of EN AW-7050 T7451 [5].

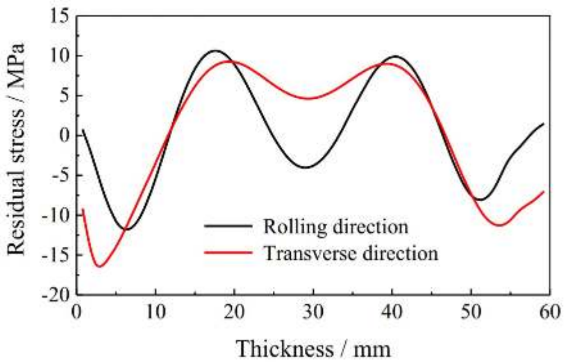

Figure 1.13: IBRS profile of Al 7075-T7451 [2].

resolution and material constraints. In [51] and [52], detailed assessments of several residual stress measuring techniques and their constraints were provided. A typical layer removal method involves layer-by-layer removal of material and measurement of resulting strains using strain gauges. The stresses associated with each level are then determined from the measured strains. The chemical etching method is typically used to remove very thin layers that range in thickness from 5 to 10 μm. The procedure is started from the top surface of the blank, going down layer by layer. The advantage of using chemical etching for layer removal is that, essentially, no new stresses are introduced during the process; thus, the obtained stress profile accurately represents the IBRS in the blank. However, it requires an expert understanding for analysis of strain gauge data; furthermore, it is a laborious task.

Some research removed the material layers by machining and performed on-machine measurements with a probe. The findings of the measured stress, however, are subject to some uncertainties when using this approach. In a research on the uncertainty evaluation of measuring IBRS by layer removal technique, Aurrekoetxea et al. [53] found on-machine probing as the major cause of inaccuracy. To improve the accuracy of the results generated by the layer removal approach, they put forth a method based on data filtering. Decoupling IBRS from the MIRS induced during layer cutting is another important source of uncertainty. However, this method provides a quick substitute for chemical etching that removes layers; additional research is required to make this process a reliable technique for measuring IBRS for various materials. New methods must also be explored for the depth characterization of these stresses. Coupled thermo-mechanical FEM analysis of different material production processes can be an alternative to the physical measurements. The drawback of FEM-based evaluations is the requirement of simulating the entire material processing sequence, including forging, rolling, quenching, etc., which is computationally time-consuming and inefficient.

After obtaining the residual stress values at different locations on the part's surface, mapping of the measured data using distribution functions is carried out to define the stress profiling of the material. It was found that a variety of functions were utilized to fit the IBRS profiles, with the 6-peak Gaussian, cubic spline, sum-of-cosines, and cosinusoidal functions being a few examples. Once the profile of stress existing in the blank is established, minimization of the distortion of the parts can be carried out using appropriate approaches. The two most frequently used strategies found in the literature are (i) toolpath or cutting sequence optimization and (ii) optimization of the placement of the part inside the blank. Both techniques have an impact on IBRS redistribution, allowing the elastic potential to release gradually. Therefore, regulating the final forms of machined components within the tolerance limits is possible by managing the liberation of static elastic potential.

Another significant conclusion that can be drawn from the aforementioned evaluation is that none of the studies could make an accurate prediction of distortion based only on the analysis of IBRS. This has two significant indications: (1) techniques and approaches for correlating IBRS with distortions need improvement; (2) additional sources, such as cutting loads, clamping loads, and static deflection of tool and workpiece, etc., need to be considered too. Finally, most of the research on the impact of IBRS focuses on aluminum alloys with thin walls. Even though aluminum has traditionally been the choice structural parts of the aircraft, alternative materials, such as alloys of titanium, are quickly replacing aluminum in these parts. This is because of their better compatibility with composites, such as carbon fiber-reinforced polymers (CFRP). Thus, investigation on the deformation of parts machined from these materials should also be carried out.

1.3.2 Machining-induced residual stress (MIRS)

Machining involves material cutting by shearing at excessively high strain rates. High temperatures and cutting forces involved may lead to residual stresses realized by (i) mechanical load-based plastic deformation, (ii) thermal gradient-based plastic deformation, and (iii) changes in the phase of the material. According to Grzesik [54], the residual stresses left in a machined part are the result of the competition between these phenomena. Despite their existence within a few hundred micrometers from the surface, these stresses are pretty significant in magnitude, especially when cutting challenging materials at rapid cutting rates. This finding was supported by the studies of Ulutan et al. [55], Lazoglu et al. [56], and Akhtar et al. [57]. Figure 1.14 illustrates a typical profile of the MIRS distribution. Part distortions are the result of these residual stresses generated during machining. MIRS and IBRS often work in tandem; the establishment of a steady state of energy in the material causes deformations of the part once it is freed from the clamping forces.

The role of MIRS in the deformation of machined parts has been established by several researchers. Using FEM, Zhang et al. [4] investigated how IBRS affected the distortion of an Al 7050-T7451 part. Ignorance of MIRS was cited as the cause of the difference in the predicted and measured residual stress results. Denkena et al. [58]

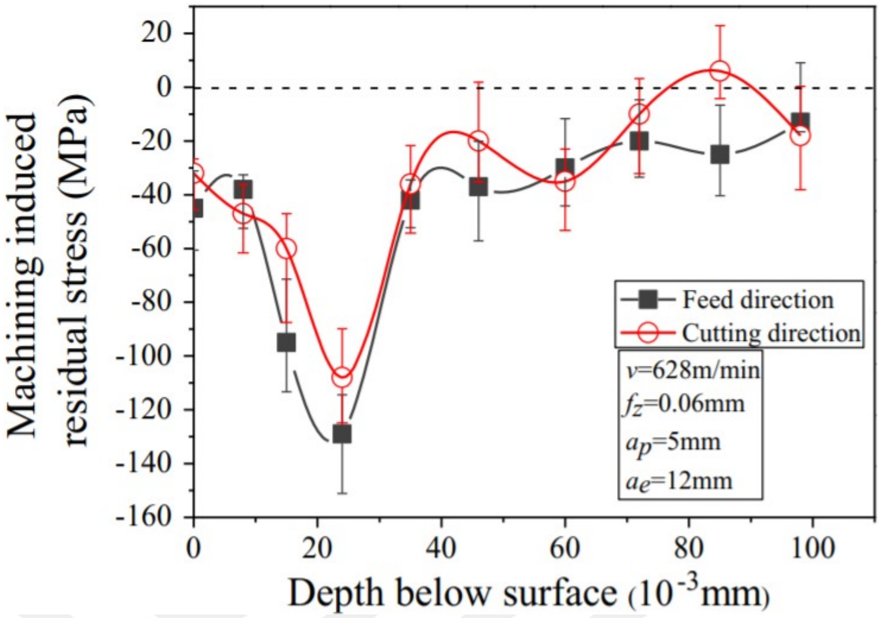

Figure 1.14: MIRS profiles of 7050-T7451 [12].

acknowledged the role of the machining-induced stresses in causing deviations in the dimensions of thin-walled parts. Brinksmeier and Solter [59] pointed out a broader contribution of MIRS in deciding the likelihood of distortion in parts machined with higher cutting speeds. Ulutan and Ozel [60] emphasized the significance of machining stresses to control the distortion and surface integrity of machined parts of titanium and nickel alloys. The importance of machining-induced stresses for controlling distortion of precision of machined parts was also emphasized by Zhang et al. [61]. These stresses were identified as one of the primary causes of part deviations in their study. The literature that identified machining-induced stresses as the primary cause of part distortions is outlined in this section, and state-of-the-art is discussed in the following section.

Gulpak et al. [13] suggested a hybrid model based on FEM to estimate deviation in shape of components caused by MIRS for 42CrMo4 steel material. The role of the variable removal rate due to the thermal expansion was incorporated. Figure 1.15, provides the summary of the suggested model. The difference in curvature recorded before and after the machining process was used to identify the stresses induced by the machining process. Measured thermal load and stresses were fitted with regression functions and incorporated into the distortion model of the part. Depending on the distribution profile of the source stresses, the results were stated to provide estimations of the part distortion that were within 1% to 5% of the observed value.

Milling simulations of a cantilevered part to predict surface error were performed

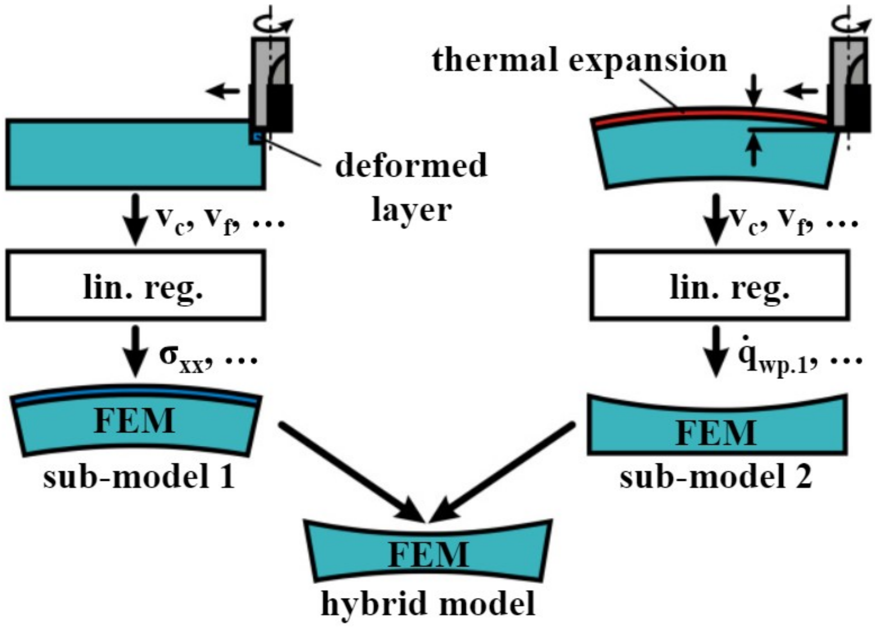

Figure 1.15: Hybrid model for prediction of shape deviation [13].

by Gang [62] in Abaqus. The separation of the chip was accomplished using the Arbitrary Lagrangian-Eulerian (ALE) meshing, and the tool was taken as rigid. The Split Hopkinson Pressure Bar (SHPB) test was utilized for the determination of true stress-strain curves corresponding to strain rates of 10000, 5000, 1000, and 0.001 $\frac{1}{s}$. The maximum discrepancy between the experimental and modeled surface errors was determined to be 21.56%.

IBRS and MIRS were investigated by Yang et al. [63] in the deformation analysis of monolithic parts. FE analysis models were defined for the milling process by taking in to account the cutting loads, IBRS, and the combined impact of both. FE simulations were run in the Abaqus by taking into account the individual and combined effects of IBRS and MIRS. Experiments were also used to validate the

FEM results. Analysis of their findings revealed that in the analysis of the annealed Ti6Al4V titanium alloy, MIRS were the primary cause of component deformation. Masoudi et al. [14] conducted an experiment-based analysis on the machining of an Al 7075-T6 thin-walled cylinder. The study was aimed at determining the influence of machining parameters on cutting temperature and force, which in turn would affect residual stresses and part distortions. By using different tool materials and altering the machining parameters, twenty-four tests were conducted. Their findings demonstrated that, compared to the carbide tool, the lower friction coefficient of the PCD tool significantly lowered the cutting temperatures and forces. Moreover, tensile and compressive stresses were related to cutting temperatures and cutting forces, respectively. As demonstrated in Figure 1.16, another significant conclusion was that the cutting forces and distortion of the workpiece were more responsive to cutting temperatures than machining stresses.

For an aged Ti6Al4V part, a method for predicting the deformation of milled

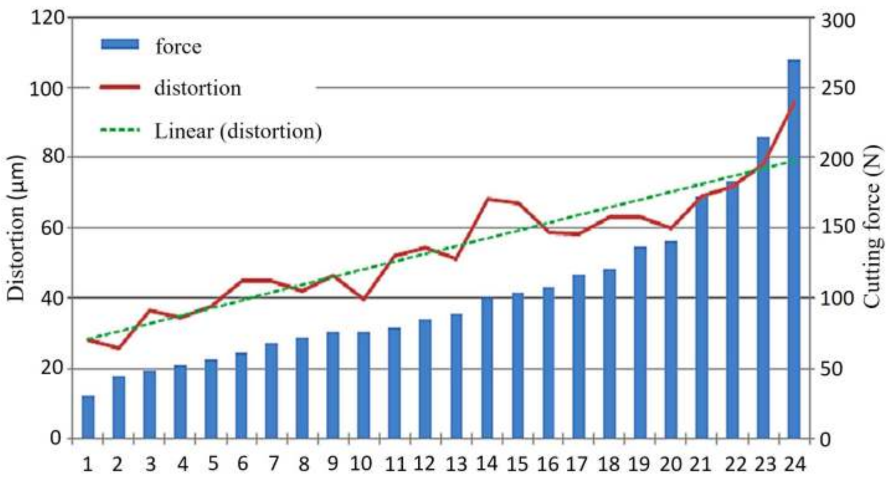

Figure 1.16: Effect of cutting force on distortion [14].

thin-walled parts based on MIRS was presented by Zhang et al. [61]. IBRS were considered extremely low due to the annealing step before cutting. By using the correlations between curvature, bending moment, and stress, an indirect estimation of MIRS was carried out based on the distortion of the machined part. Then, a polynomial fit was used to fit the measured MIRS for the FEM analysis. MIRS layer thickness was measured and compared with literature to quantify the error related to it. Part deformations were predicted by defining the estimated MIRS in the Abaqus model. The suggested model was tested on a blade and a simple part; the results were found within 10% and 20% for the respective case.

Yao et al. [15] performed deformation simulations for a milled and shot peened fan blade as shown in Figure 1.17. For the thin-walled blade of Ti6Al4V alloy, uneven distribution of stresses was considered in various regions/layers. As shown in Figure 1.18, the front and rear blade surfaces were segmented into parts to measure the stresses following the processing. FEM simulation of residual stresses and deformations was then performed in Abaqus. Figure 1.19 provides the outcomes of the deformation simulation. Measurement of the through-thickness residual stress was done by chemical etching and XRD techniques. Deformation results were determined to be within 25% of experimental values. A strategy for distortion correction for thin-walled blades based on feedrate optimization was given by Zhang et al. [64]. An asymmetrical MIRS profile was created by optimizing feedrate for various areas of the blade surface. On various sections of the blade surface, different MIRS corresponding to various process conditions were mapped using FEM. It was reported that the asymmetry in the MIRS served to compensate for the imbalance in the removal of material. The stated deflection value decreased by 43.87%.

In order to correlate parameters of the milling process with deformities of an EN AW-7022 T652 (aluminum alloy Al-Zn-Mg) part, Karsten et al. [65] did an experiment-based analysis. Experiments with end milling and face milling were carried out. The effect of milling parameters on the cutting temperatures and forces was analyzed. According to their findings, the biggest factor determining part deformations was cutting temperature. Toubhans et al. [66] investigated the influence of elastic deformation of the workpiece and machining-induced stresses on the geometrical accuracy and distortion of thin Inconel 718 turning parts. A laser-based profilometer system was employed for in-situ measurement of deformations and geometric errors of the workpiece. The influence of machining-induced residual stresses

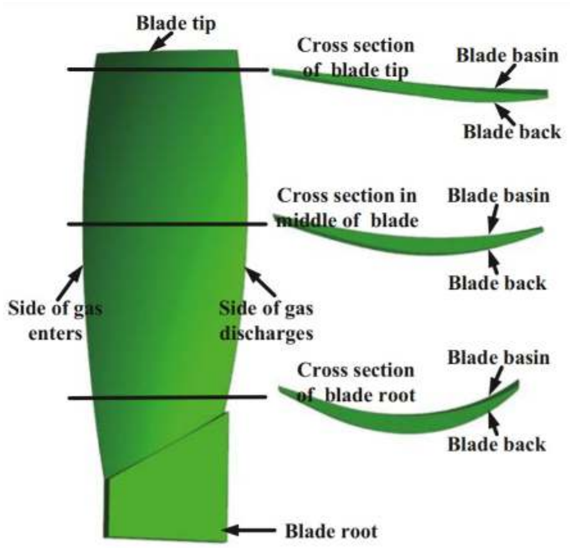

Figure 1.17: Thin-walled blade [15].

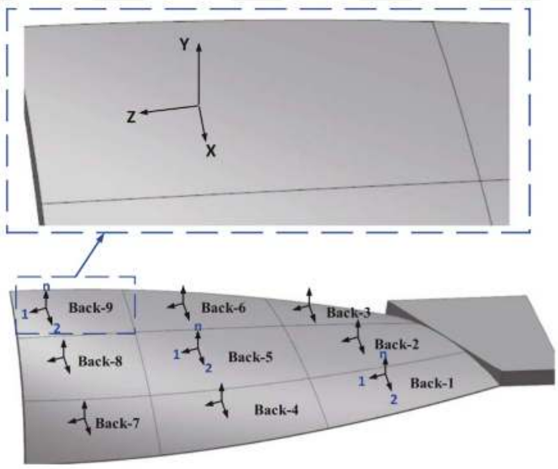

Figure 1.18: Segmentation of blade surface for analysis [15].

was stated to be significant, accounting for 3% to 32% of the total geometrical error. Hussain and Lazoglu [67] and Lazoglu and Mamedov [68] employed hybrid (analytical and FEM-based) techniques to estimate distortions of milled thin-walled part of Al 7050-T7451 and micro-milled part of Ti6Al4V, respectively. The findings of these studies proved the involvement of the MIRS in the deformation of the parts. Fergani et al. [69, 70] presented analytical techniques for estimating distortions for thin-walled parts of Al 7050 for conventional milling operations and micro-milling

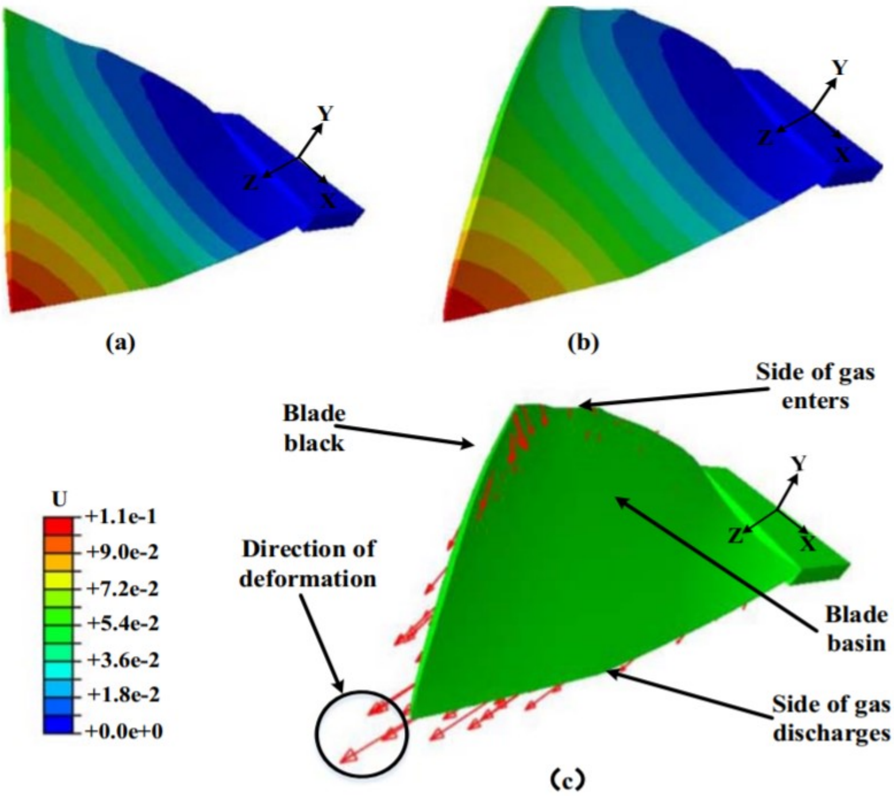

Figure 1.19: Deformation simulation: a) blade model, b) deformation of blade profile, and c) deformation vectors [15].

processes. It was stated that the inaccuracy in the distortion predictions had a difference of 30% from the experiment results. These studies indicated that MIRS significantly contributed to part distortion.

Discussion on MIRS mechanism

The aforementioned literature analysis makes clear that MIRS has been mentioned in several investigations as a key factor affecting the distortion of aeronautical components. Large cutting forces and high temperatures are observed during the machining of hard-to-machine materials, such as nickel and titanium alloys. These high cutting loads give rise to substantially high MIRS, which need to be considered for distortion analysis. For instance, Toubhans et al. [66] concluded that the distortion in the turning of a thin-walled section of Inconel 718 was caused by MIRS to the extent of up to 32%. By comparing MIRS-based distortion predictions with experimental values, the impact of MIRS on part distortions was demonstrated. As a result, it is clear that MIRS must be taken into account for effective distortion control as it significantly contributes to the distortion of machined components. Masoudi et al. [14] reported that machining forces played the primary role, whereas Karsten et al. [65] observed that cutting temperatures were the primary factor in MIRS-based distortions. Additionally, Brinksmeier and Solter [59] noticed a greater role of MIRS in part distortion as a result of increased cutting speed, hinting towards the increased influence of machining temperature. The fact that machining forces and temperatures may vary due to several variables, such as cutting parameters, cutting tool material, usage of coolant, the shape of the workpiece, etc., may help to explain these opposing viewpoints. For instance, increased cutting speed results in higher cutting temperatures and lower cutting forces. Depending on the variation of the process variables, the contribution of cutting forces and temperatures towards MIRS may change, resulting in a consequent change in the part deformations.

Despite the fact that MIRS have been the subject of several studies, much of the research used finite element simulations to estimate these stresses. There are a few works that used a hybrid or totally analytical method. The primary reason for this is the intricacy of modeling the residual stresses and distortion of the 3D milling operations. The inapplicability of these models to complicated forms was also discussed by Zhao et al. [71]. Furthermore, it was found that the combined impact of mechanical and thermal processes on the deformation and surface integrity of thin-walled parts is challenging to represent in machining process models. The study also stressed the need for collaborative manufacturing technologies that aim to take into account how different process mechanisms affect the integrity and form of thin-walled structures. In contrast to analytical models, doing FE simulations of machining using commercial programs, such as Abaqus, Ansys, DEFORM, etc., is rather straightforward. Some FE programs, e.g., AdvantEdge, even have the special capabilities of simulating machining processes. The main disadvantage of FEM-based machining simulations is the requirement of large computing capabilities and long simulation times. The convergence issues due to very high strain rates and the requirement of re-meshing after material removal are two major hurdles in the efficient simulations of machining processes. Therefore, more effective analytical models must be established to enable effective distortion prediction simulations.

The fact that the majority of the modeling approaches employ the common mechanical constitutive rules of a stress-free material is another factor putting a question mark on the reliability of FE simulations of MIRS. This assumption is applicable if all the IBRS have been eliminated during the stress-relieving carried out before machining. But this is rarely the case; even after stress-relieving procedures, certain residual stresses may still exist, although their levels might not be as high as before stress-relieving. Therefore, to improve the prediction accuracy of simulations, it is significant to properly quantify these residual stresses. Some studies have indicated towards the impact of IBRS on mechanical characteristics such as yield stress [72,73]. As a result, it is anticipated that a more accurate measurement of the IBRS, along with the use of constitutive laws for stressed materials, may increase the predictability of these simulations.

1.3.3 Combined effect of MIRS and IBRS

The discussions up to this point have made it evident that IBRS and MIRS are both very important for forecasting the distortion of a machined part. According to [6], both of these might cause dimensional deviations as well as in-service mechanical performance issues. To obtain a more accurate understanding of the distortions of machined components, it is crucial to take into account the impact of both mechanisms. This section reviews the research that looked at the impact of IBRS and MIRS and discusses the state of the art on the subject.

Hui-yue and Ying-lin [74] investigated the distortion of a machined monolithic part of Al 7075 in end milling. FEM was used to calculate the initial stresses generated by the quenching heat treatment and stretching. Deform 3D was employed to determine the cutting loads due to a single-edged end mill. The computed cutting loads were imposed on the part mesh in Abaqus. In contrast to the gradually changing chip thickness, a more straightforward rectangular chip geometry was adopted. Application of cutting loads was carried out at the beginning of each cutting step, whereas BIRS were defined as initial conditions at the beginning of the simulation. For subsequent passes, the deformed part geometry from the previous pass was considered (a process known as restart calculation). The active cutting layer was only meshed with fine mesh to speed up computation. It was stated that the distortion simulation findings were satisfactory. The computation of initial stress error and oversimplified part geometry assumptions were cited for the discrepancy between FEM and actual experiment findings.

The architecture of the system for machining simulation proposed by Rai and Xirouchakis [16] is depicted in Figure 1.20. For the Al 7075 part, the framework took into account the transient thermo-mechanical loads of cutting as well as the IBRS and the clamping forces. For thermo-mechanical calculations, cutting loads were applied at nodes in the Ansys solver. FEM simulations for a part with a simple shape comprised of pockets and slots were only provided. It was, however, claimed that the suggested system had been verified for various parts. With various adjustments in the magnitudes, the system appeared to be able to predict the trend of cutting forces, temperatures, and part deformities in the case study that was provided. The vibrations of the workpiece/tool and tool wear were assumed to be negligible; furthermore, back-and-forth tool passes were only considered. The proposed framework might address the issue of component distortions, but additional research is needed to confirm its viability for complicated geometries, such as profiled parts.

A technique for predicting machining distortions for Al 7050-T7451 was published by BI et al. [75] that considered the phenomena of clamping, IBRS, and MIRS. IBRS were measured by adopting the layer removal approach. Cutting temperatures were determined analytically using band heat source theory, whereas cutting forces were determined in DEFORM-3D. Time domain application of the MIRS and cutting temperature in the blank model was realized in Abaqus. The simulation of distortion was done in two steps. The two-step procedure employed for simulations consisted of applying cutting loads with fixture constrains followed by removal of

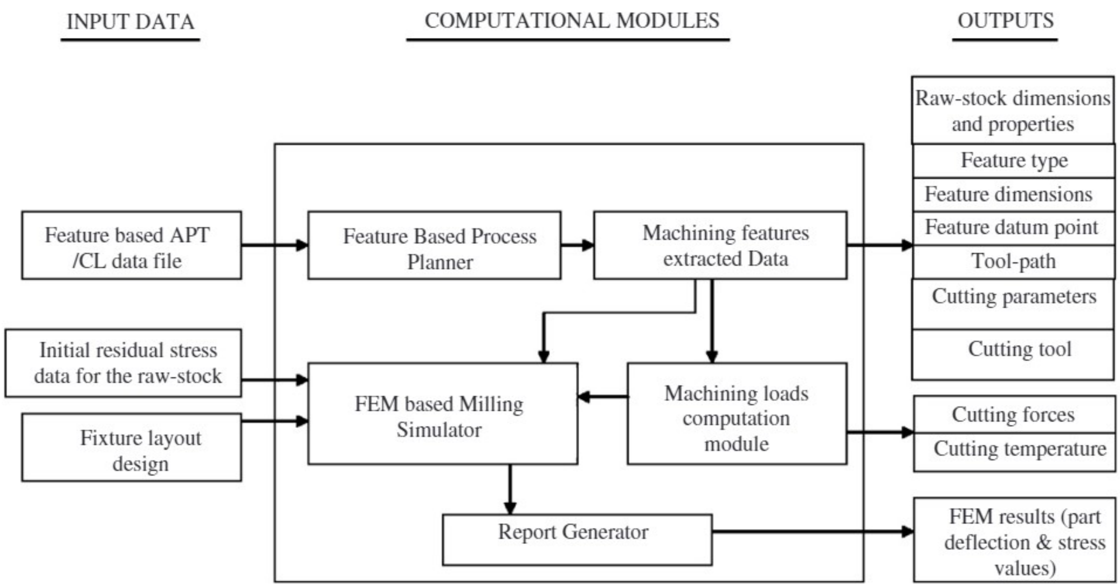

Figure 1.20: Architecture of the simulation system [16].

fixture constraints and allowing the component to deform due to the applied loads. The simulated values were reported to be within 19% of the experimentally measured results.

Guo et al. [17] performed distortion simulations for a multi-frame part milled from thick plates of the alloy Al 7075-T7351. Based on experimental data collected using the improved layer removal approach, the impact of initial stresses was predicted. The FEM platform used Ansys with APDL programming, and simulations of part deformation were conducted. The simulation results as depicted in Figure 1.21, were reported to deviate from experimental results by 18%. This disparity in outcomes was linked to ignoring the cutting temperatures.

Jayanti et al. [18] proposed physics-based models dynamic tool deflection and deformation of an Al 7050 part. The model considered the effects of both bulk and residual stresses generated by machining. Using AdvantEdge FEM software, stresses caused by machining were determined. Toolpath analysis was said to be done in a commercial mechanistic model of five-axis milling. A FEM solver was then used to apply the predetermined stress data of MIRS and IBRS. The final geometry of the part derived using the toolpath analysis model, was used to build the mesh of the

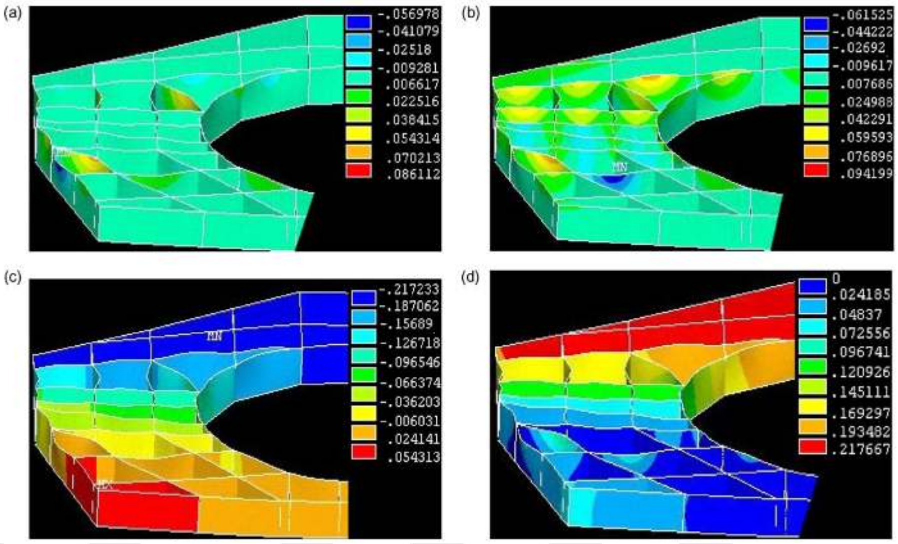

Figure 1.21: Simulated distortions in different directions: (a) x-dir (b) y-dir (c) z-dir (d) the total distortion [17].

part distortion model. Figure 1.22 shows the outline of the presented approach.

A technique for predicting machining distortions for Al 7050-T7451 was presented

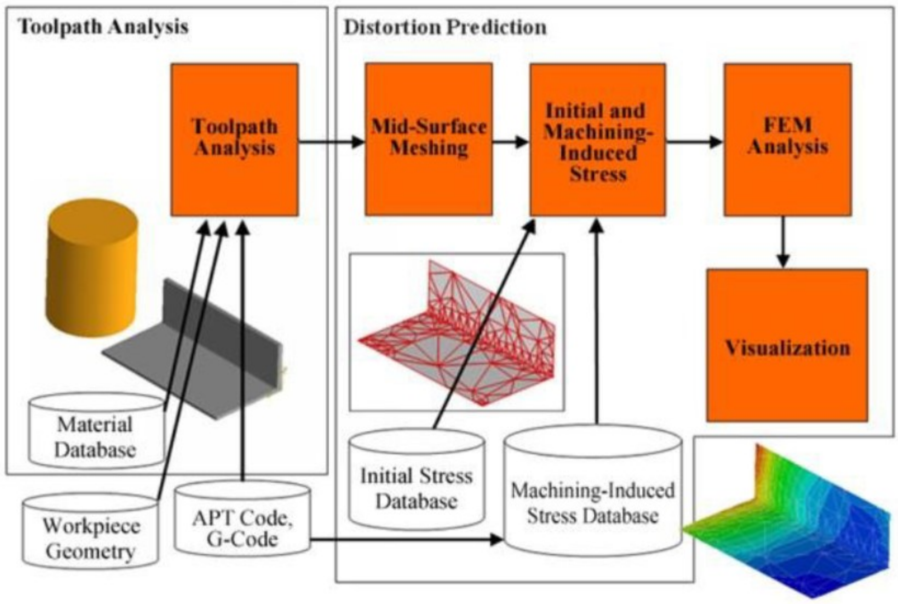

Figure 1.22: Outline of the approach for distortion prediction [18].

by Tang et al. [19] that took into account the contributions of clamping, IBRS, and the MIRS. Forces due to clamping were applied as contact pressure and displacements. IBRS characterized by the crack compliance method were imposed on the part model in Abaqus. The MIRS due to a single tooth milling tool were simulated using Deform-3D, and the cutting temperature was modeled as a moving linear heat source. The part distortion model in Abaqus was then subjected to cutting forces and temperatures in the time domain. The results of distortion analysis, depicted in Figure 1.23, were reported to deviate from the experimental results by 20%. The disparity in results was associated with the assumptions regarding simplified chip geometry, cutting load calculation, tool wear, and uniform distribution of residual stresses in each layer of the blank (as illustrated in Figure 1.24).

Li et al. [76] studied the impact of the depth of cut on the control of distortions

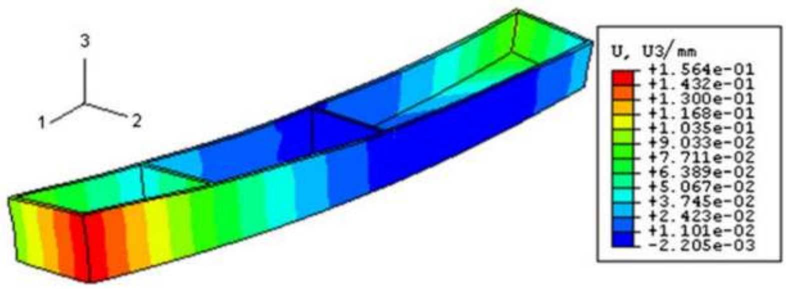

Figure 1.23: Deformation simulation for frame component [19].

for thin-walled parts of Al 2024-T3. The redistribution of IBRS and MIRS were considered. The investigation made use of both AdvantEdge simulations and experiments. IBRS were calculated from total stresses identified after the machining experiment, whereas MIRS were acquired via FE simulation. It was claimed that optimizing the depth of the cut might reduce the distortion of the finished part. It was found that the same had a nonlinear impact on the MIRS and the distortions due to the machining process. The occurrence of redistribution of IBRS was deduced when considering the observation that the final residual stresses of the part with or without considering the IBRS was not the same as the original IBRS.

By carrying out FEM analysis in Abaqus, Huang et al. [12] investigated the impact of IBRS and machining-induced stresses on the deformation of a machined mono-

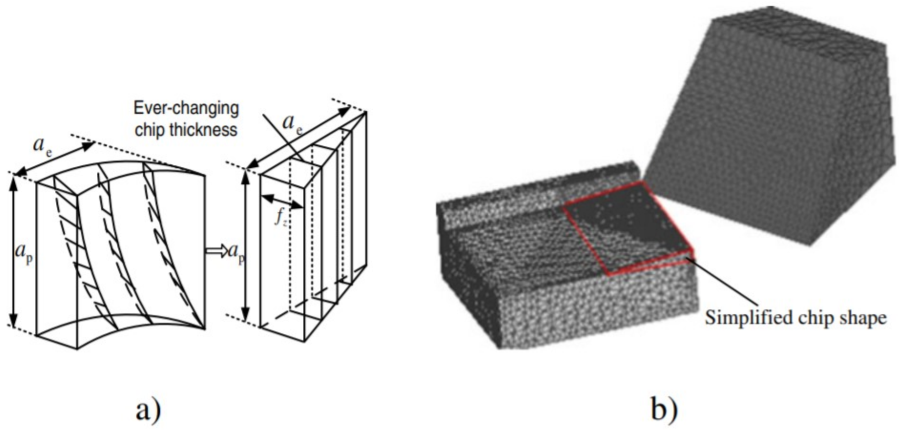

Figure 1.24: FEM model of oblique cutting: a) simplified chip shape and b) cutting model [19].

lithic frame part of alloy Al 7050-T7451. IBRS were quantified using the crack compliance technique and fitted with a double-peak Gaussian function. The FEM model, as seen in Figure 1.25, was fed with quantified values of IBRS and MIRS. The results indicated that 90% of the deformation was due to the IBRS. The outcomes of distortion simulations considering the impact of IBRS, MIRS, and the combined impact of the two are shown in Figure 1.26.

In a different investigation, Huang et al. [77] examined the impact of IBRS and

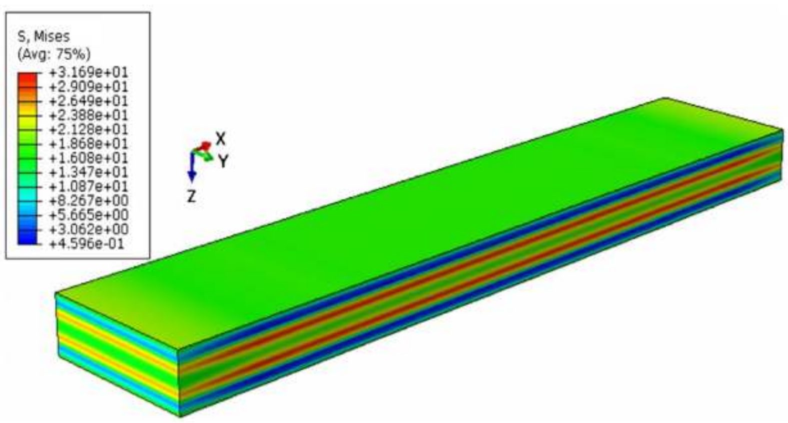

Figure 1.25: FEM model for IBRS of 7050-T7451 alloy blank [12].

machining-induced stresses on the deformations of an Al 7050-T7451 part. Mea-

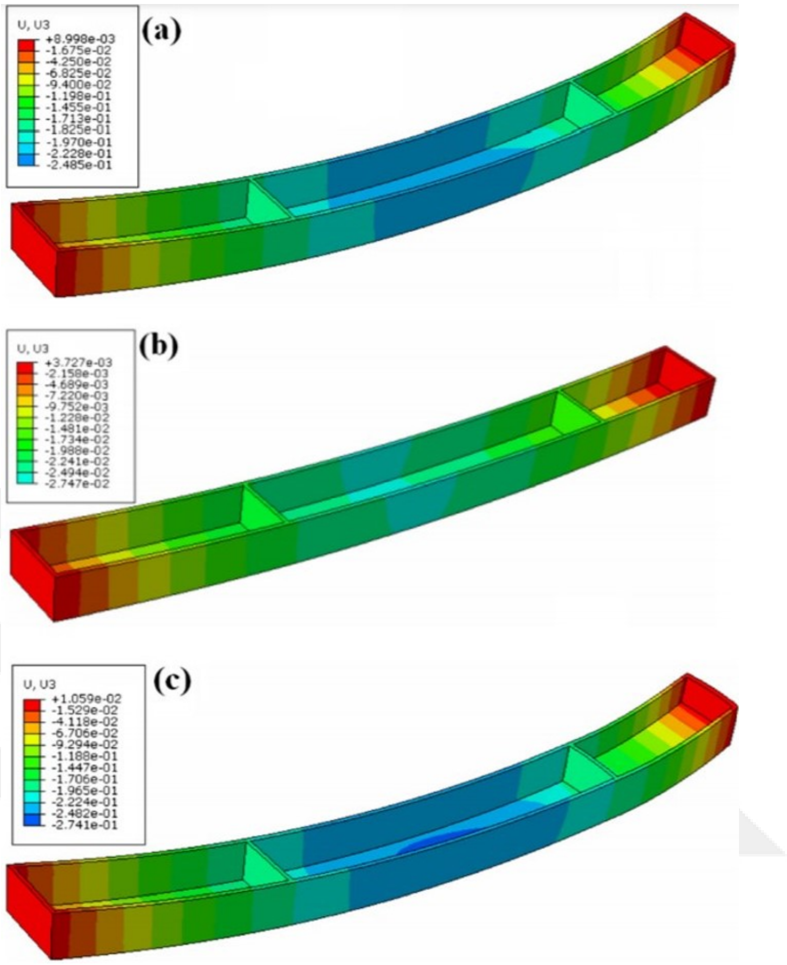

Figure 1.26: FEM simulations of machining deformations (×100): a) considering IBRS, b) considering MIRS, and c) considering the coupling of the IBRS and MIRS [12].

sured IBRS and machining stresses were used as the initial conditions for FEM simulations in Abaqus. While MIRS were determined by using XRD and chemical layer removal methods, IBRS were determined by the crack compliance technique. It was stated that MIRS were the primary reason for part distortion. A comparison of their two investigations reveals that the amount of material removed, the final machined component's form, and its placement inside the blank all affect how IBRS and MIRS contribute to part distortion. They stated that the impact of MIRS was more noticeable for plate thickness of less than 1.25 mm.

Jiang et al. [20] employed Abaqus, AdvantEdge, and DEFORM for simulating the stress state of the forged Al 7050 part. To examine their influence on workpiece deformation, residual stresses resulting from the machining and heat treatment processes were taken into consideration. IBRS were determined using the DEFORM-3D FEM modeling of heat treatment, while MIRS were determined using the AdvantEdge program. For workpiece distortion calculations, both estimated stresses were entered in Abaqus. According to their research, different profiles of the IBRS and sequences of cutting paths resulted in varying levels of part distortions, as seen in Figure 1.27. To optimize the machining process of the workpiece for less distortion, several machining sequences were taken into consideration.

The stress condition throughout each step of the production of an engine case

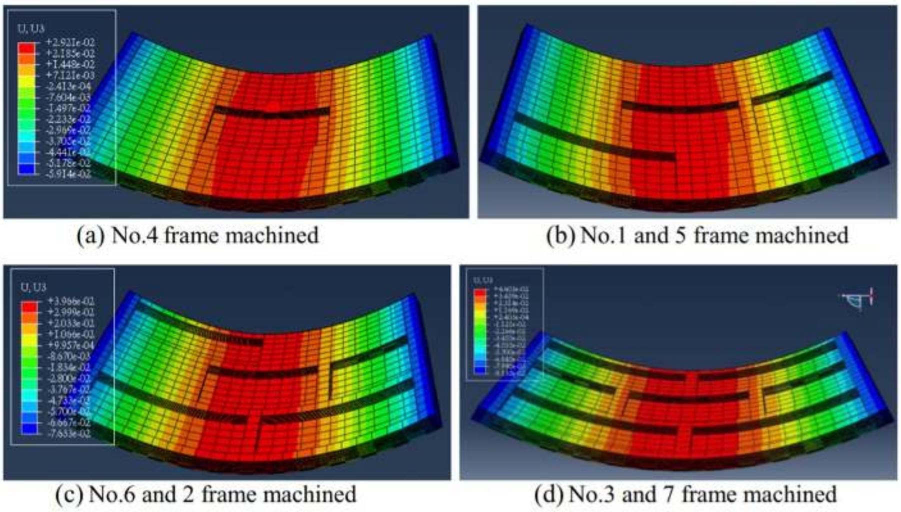

Figure 1.27: Effect of material removal on distortion [20].

of Ti6Al4V alloy was simulated by Wang et al. [21]. FEM was used to simulate how different procedures, such as forging, rolling, and machining, might affect the part's stress state. DEFORM-3D was employed to simulate IBRS caused by forging processes as shown in Figure 1.28, whereas AdvantEdge was utilized for simulating MIRS resulting from the turning operation, as shown in Figure 1.29. The material removal sequence was then optimized by feeding measurement data of IBRS and MIRS into an FE model. They also looked at how strain energy changed for different processes. An optimal machining sequence for material removal was determined by considering the zones of tensile and compressive stresses. Accordingly, it was stated that the process sequence involving a quick decrease of part's strain energy results in an optimized process. Additionally, greater distortion control was noted by eliminating zones of compressive stresses prior to eliminating the zones of tensile stresses. Their study also discovered a significant contribution of IBRS and MIRS and the stiffness of the part being machined. IBRS initially played a role in the deflection of the part to the extent of nearly 90%, but MIRS's effect increased to the extent of 47.1% with the decrease in the part stiffness after roughing.

An outline of a procedure for analyzing part distortions under the action of IBRS,

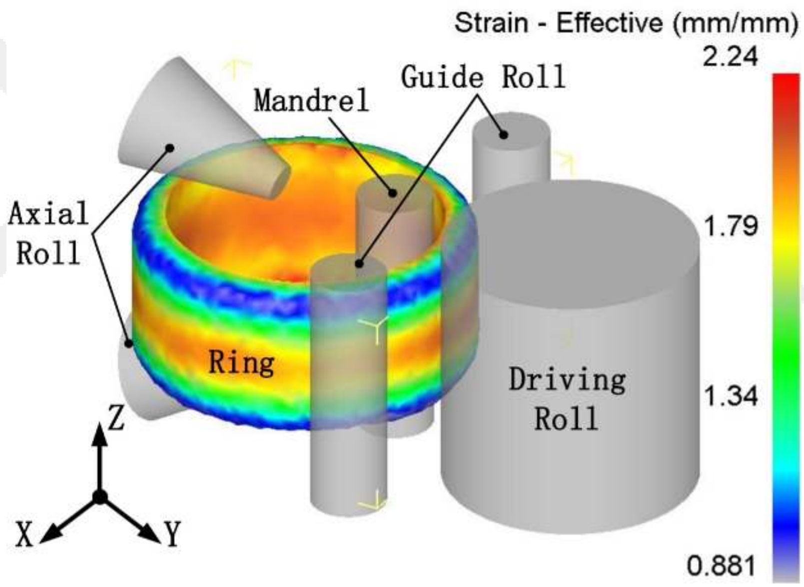

Figure 1.28: FEM of the rolling process [21].

MIRS, and both of these combined was provided by Weber et al. [78]. They used the slitting approach to measure IBRS and calculated MIRS using FEM in Abaqus. It was suggested to predict distortions using the Eigen strain field calculated from IBRS as well as from the combined impact of both types of stresses using the inverse analysis. Only the findings of experimental cutting force and MIRS measurements were given; validation of the efficacy of the proposed approach efficacy was not done. For the Al 7050-T7451 component, Aurrekoetxea et al. [79] provided an altered approach for the layer removal technique to assess the IBRS. IBRS were determined

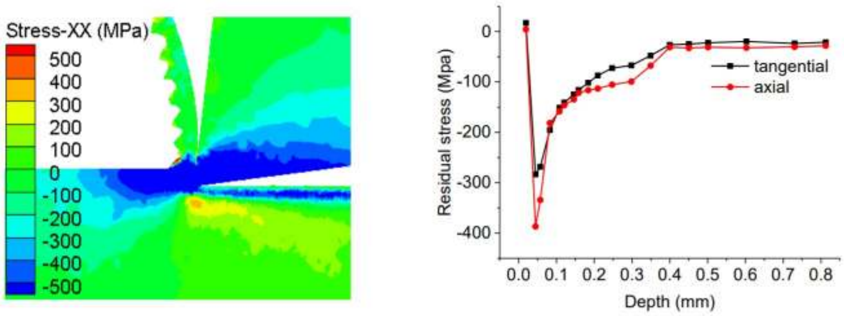

(a) Simulation Stress (b) Machining-induced residual stress varying with depth

Figure 1.29: Post turning residual stresses [21].

through layer-by-layer ($1mm$) machining of the material and subsequent on-machine measurement with a machine probe. To gauge the stress profile, the change in the curvature of the part with the removal of each layer was determined. To get the real IBRS of the blank, the impact of MIRS and the initial deflections of the component were also taken into consideration. Their research demonstrated that to obtain the accurate profile of IBRS, machining-induced stresses, and initial stresses due to clamping must be taken into consideration. The drawback of the proposed method was the requirement of measurement of MIRS carried out by the destructive hole-drilling technique.

An in-process active technique was proposed by Zhang et al. [22] to regulate the effect of IBRS and MIRS on the deformation of thin-walled parts. For the proof of concept, a blade part of Ti6Al4V having a simple geometry was employed, and a prototype design was also given for the active fixture system, as illustrated in Figure 1.30. The method relied on compensating the distortions caused by MIRS and IBRS following every cutting pass with the opposing distortion generated by the forces applied using the active fixture system. Reduction in distortion of 18.3% and 42.9%, respectively, was reported as compared to non-relaxation and full in-process relaxation cases.

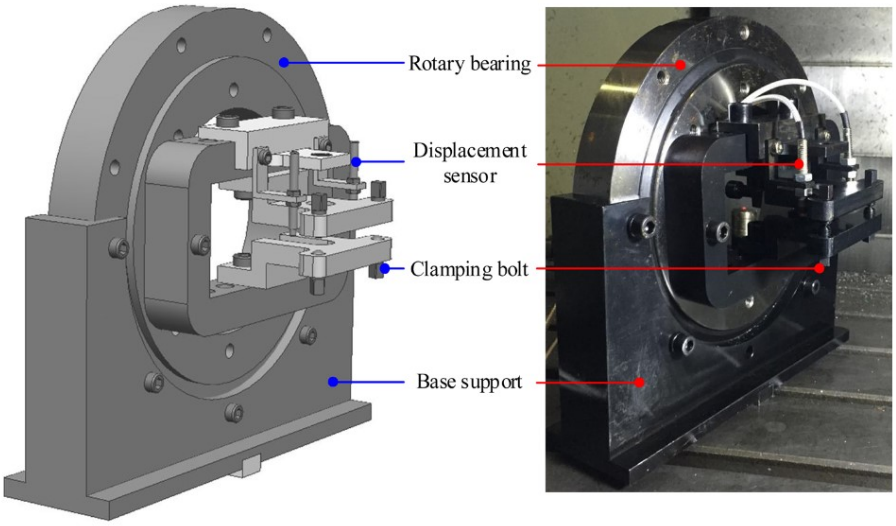

Figure 1.30: The proposed active control fixture [22].

Discussion on the combined effect of MIRS and IBRS mechanism

In multiple studies, the combined impact of MIRS and IBRS on distortions of parts has been assessed by adhering to a usual process. The procedure consisted of determining IBRS profiles using FEM. Similarly, FEM models and measurements were used to evaluate MIRS profiles. The determined IBRS distribution was fitted with appropriate functions and imposed on nodes of the FEM model for each level of the workpiece depth. The clamping of the workpiece during loading was modeled by fully constraining the workpiece. Material removal was accomplished in FEM utilizing element birth and death technology, and MIRS related to different cutting passes were also applied as nodal values. Redistribution of the stresses in the blank after each cutting pass was allowed. In each cutting pass, the MIRS measured in the former pass was applied as IBRS, and the MIRS of the current pass was applied. The process was repeated until all machining stages had been completed. In the end, the workpiece's rigid body motion was restrained by the 3-2-1 constraint method, and free deformation of the workpiece under the influence of residual stresses was allowed.

The following assumptions are commonly employed to circumvent the complexities of modeling complicated machining process dynamics. (1) IBRS value for every level in the workpiece depth is constant. This is supported by the premise that various material production methods equally influence each plane of the blank. (2) A simplified rectangular shape of the cutting chip is assumed instead of the real curved form produced by milling. This is done to facilitate assigning loads and stresses to the part mesh. (3) Deformation of the workpiece is determined after the completion of all cutting passes. Hui-yue and Ying-lin [74], in contrast, calculated the deformation due to every cutting pass, and the in-process deformed shape was remeshed for the subsequent cutting step. Calculating the distortion of the part following each cut and re-meshing the deformed part for the subsequent pass may look more realistic, but it might significantly extend the simulation time. Additionally, no evidence of any improvements by using this strategy over the widely used method of estimating distortions at the conclusion of machining was found. Investigations on examining its effectiveness and computational complexity may be helpful in this regard. (4) The role of the dynamic deflection of the cutting tool taken into account by Jayanti et al. [18] is regarded insignificant. (5) Tool wear and vibrations caused by the tool or workpiece are also assumed to be negligible. Despite carrying out investigations on simple part shapes in most of the studies, the results of prediction of distortions were typically observed to deviate up to 25% from the experimental values. It is possible that these assumptions are partially (if not entirely) to blame for deviations in predicted outcomes.

The discussions so far have made it abundantly clear that regulating the distortions of the machined component requires the use of both IBRS and MIRS phenomena. With the exception of a few studies, the contribution of each process is not well understood. It has been noted that these mechanisms' contributions are not fixed but change when the material's condition changes during the machining process. Xiaoming Huang et al. [12,77] observed that machining-induced stresses were the dominant cause for a plate part in two studies that were conducted under comparable cutting settings. On the other hand, an airframe monolithic component that required substantially greater material removal was 90% deformed due to IBRS. In roughing operations that involve substantial material removal, IBRS play a dominant role, whereas MIRS become increasingly relevant during finishing and semi-finishing steps as a result of the reduced thickness/stiffness of the part. Any mechanism that may alter the interaction of IBRS and MIRS may affect distortions; for example, Jiang et al. [20] and Wang et al. [21] found that the sequence of material removal, which may change the behavior of the residual stresses, affected part distortion.

The blank material is also a significant aspect that affects how these mechanisms behave. It was discovered that the influence of machining-induced stresses was predominated for components machined alloys of titanium and nickels, whereas the effect of IBRS was more obvious for aluminum blanks. The excessively high cutting loads generated while machining the high-temperature alloys were cited as reasons for the domination of MIRS.

Techniques and methods for adequate part distortion characterization before starting the actual machining process are essential due to the significance of both MIRS and IBRS in affecting distortions. The literature review above also indicates the dependence of various distortion prediction approaches (considering these mechanisms) on FE simulations. The majority of the research employed FE simulations to determine MIRS. These simulations required days to complete, even for simple machined parts. In a study of models and methods used in industry for machining thin-walled parts of light alloys, Sol et al. [80] also emphasized the limitations of simulation models for machining operations. It is consequently vital to create analytical models that take much less time and better capture the process's physical phenomena.

The layer removal technique turned out to be a reliable method for finding the IBRS of the blank. For each component, finding the IBRS profile using a destructive layer removal approach is very inefficient. This may be avoided by creating IBRS profiles for the common aerospace materials. This is quite feasible as the IBRS profiles of standard materials don't vary considerably due to the reason that these materials go through standard production and heat treatment procedures. However, a database including the IBRS profiles of frequently used aerospace materials is needed to make part distortion analysis more practical. Once IBRS and MIRS profiles have been established, these may be imposed in the part models built in FEM software for fast simulation of part distortions.

1.3.4 Static deflection of cutting tool/workpiece

The effect of MIRS and IBRS in distorting a machined part was discussed in the previous sections. Another important phenomenon that was frequently cited to affect the sizes of precision machined parts is the static deflection of the tool and/or the workpiece. Generally, cutting tools were modeled as rigid bodies, tool and workpiece deflection, static and dynamic compliance, and variable cutting forces were neglected in the analysis of the machining process. These simplifications often affect the accuracy of machining error predictions, hence affecting the control strategies [23]. Static deflection of the tool was normally found more prominent in the case of roughing operations involving large material removals or while machining difficult-to-machine materials where large cutting forces were involved. On the other hand, static deflection of the workpiece was dominant in the machining of thin-walled parts, especially in finishing/semi-finishing operations characterized by considerably reduced stiffness of the workpiece [65]. Several studies have found a substantial effect of cutting force-induced static deflection of the tool and workpiece on part deformations, primarily for thin-walled parts. Static and dynamic deflection of end milling cutter was said to cause form and surface errors, respectively, for jet engine impeller blades and rotor disks [24]. Another study [25] also attributed surface errors in the milling process to the deflection of the workpiece and the tool. Ratchev et al. [23] proposed a model for part deflection error measurement due to the static cutting forces. Cutting forces in the radial direction and corresponding part deflection in the radial direction was only considered. Variation of tool immersion caused by static deflection of the part and the related effect on cutting forces was accounted for in the model. The claimed flexible model illustrated in Figure 1.31 used an iterative procedure to converge to the final force and deflection value for each tool location. Cutting forces were calculated by an analytical method using orthogonal to oblique transformations for the milling process. Calculated cutting forces were applied in the Abaqus to get the part deflections.

Ratchev et al. [24] proposed an offline error compensation approach to modify the

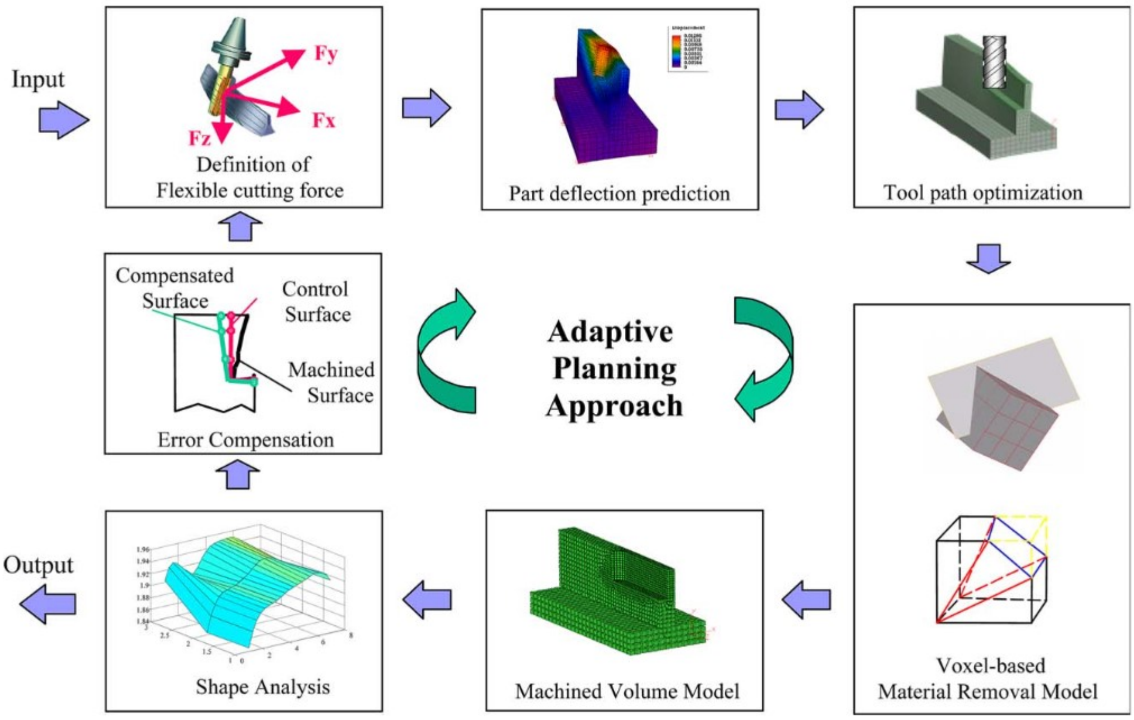

Figure 1.31: Outline of a system for adaptive planning of the machining process [23].

machining toolpath for compensating the part deflections due to static cutting forces for Al 6082 H30 alloy. An overview of the proposed model and optimization strategy for the milling tool path is given in Figure 1.32 and Figure 1.33 respectively. Part deflection in the radial direction due to radial cutting forces were only considered. Cutting forces were calculated by an analytical method using orthogonal to oblique transformations for the milling process. Calculated cutting forces were applied to the Abaqus to get the part deflections. A compensated tool path file was written in machine code based on the part deflections. Part deflections were imposed on the surface model of the original part for machining simulations with errors in the VERICUT software. Part deflection errors were reported to be reduced from 21% to 6% by the proposed error compensation strategy.

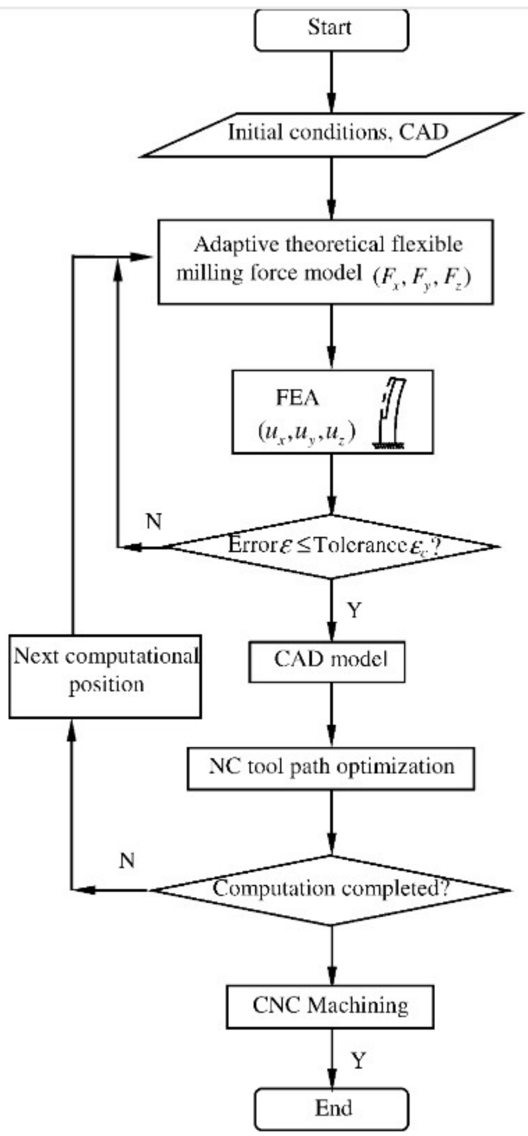

Figure 1.32: Flowchart of off-line error compensation based machining process optimization [24].

Aijun et al. [81] proposed a reciprocal theorem based analytical formulation for determining part static deflections due to end milling forces. Cutting forces calculated from the analytical model were input to the FEM, and part deflection simulations were performed in Ansys for the aluminum alloy part. The part was modeled as a cantilever beam, and cutter loads in the radial direction were applied as distributed loads along the axial direction. The deflection of each edge was analyzed at a time,

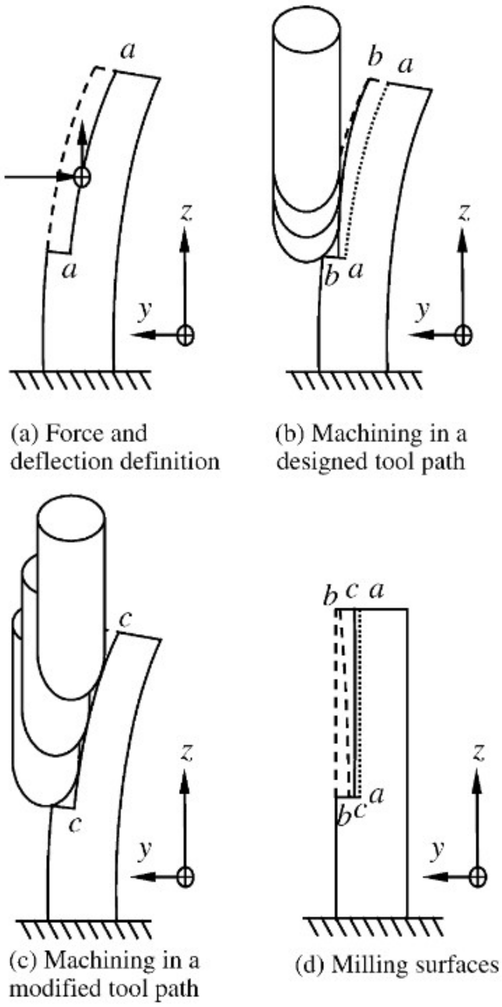

Figure 1.33: Optimization of end milling tool path (a) definition of deflection and force (b) cutting with normal tool path (c) cutting after modification of tool path (d) Surfaces of the machined part [24].

and the effect of cutter location, part thickness, and radial forces (considered as linear load) was considered in the simulations. All these factors were reported to influence part deformations. It was claimed that static deflection was a significant source of part deflection in machining.

Chen et al. [25] presented a method for error compensation by considering workpiece and tool deflection during each cutting pass/layer. Variations of axial cutting depth and corresponding cutting forces were considered the basic problem for error compensation. An iterative algorithm was used to convert static workpiece deflection and calculate corresponding cutting forces. The calculated cutting forces at each tool location were then applied using FEA to simulate the workpiece and tool deflections. It was shown that the active layer-by-layer compensation method gave less overall error than a single compensated pass at the end of the cutting process. The compensation strategy is presented in Figure 1.34. Here, lines a, b, c, and d represent the prior machining workpiece surface, the desired machined surface, the deformed surface without compensation, the surface after being machined without compensation, and the surface after being machined with compensation, respectively.

Gao et al. [26] presented a workpiece deformation control method based on cutter

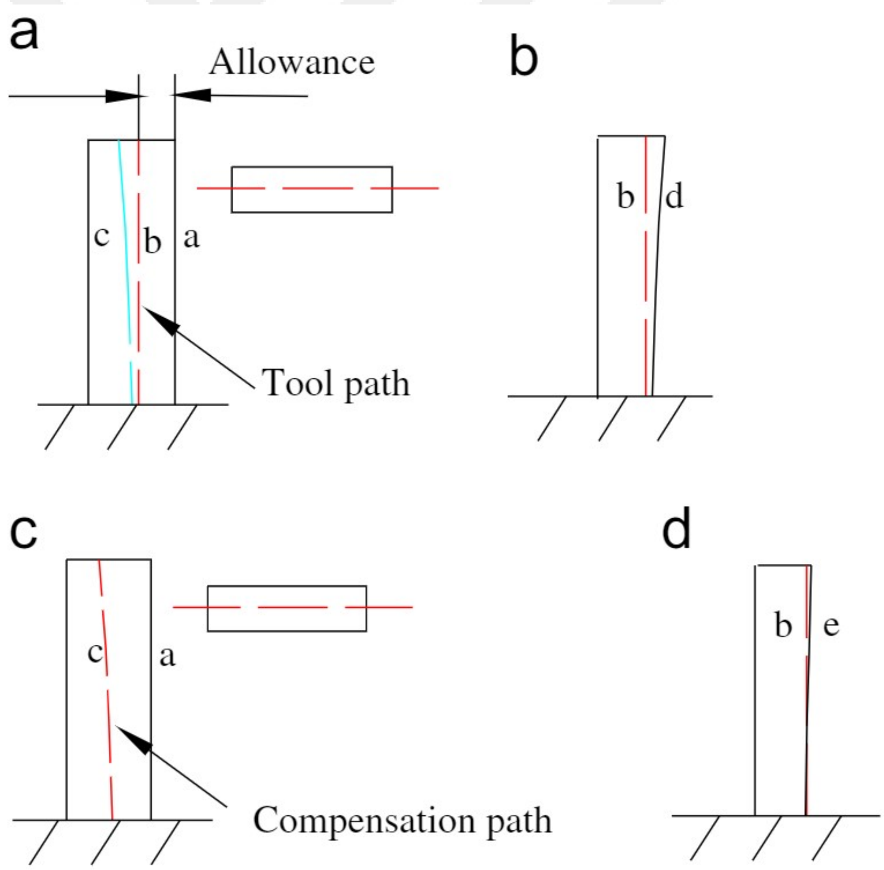

Figure 1.34: Full compensation of a layer [25].

path compensation for thin-walled arc-shaped parts of TC4 titanium alloy. The deformations due to cutting forces were only considered. A statistical cutting force model was built using the response surface method (RSM) against three cutting parameters, i.e., axial depth of cut, feed rate, and spindle speed. Based on the cutting forces determined using the regression analysis, the static deflection of the workpiece was analyzed in Ansys. Finally, toolpath compensation based on the mirror compensation principle is shown in Figure 1.35 was carried out to compensate for the deflection values as illustrated in Figure 1.36. The reduction in thickness variation of the thin-walled part after adopting the proposed methodology was reported to be 52.88%.

Wu et al. [82] analyzed workpiece deflection due to static and dynamic effects of

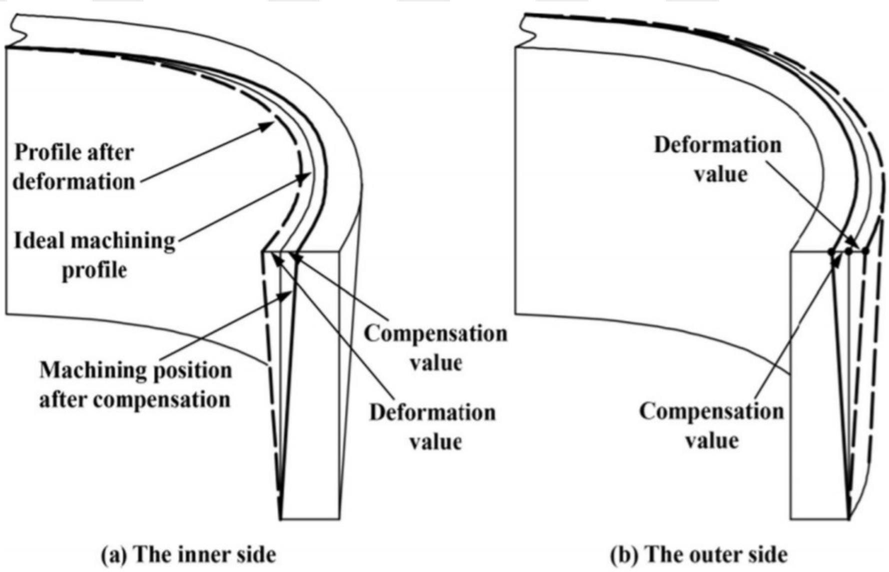

Figure 1.35: Mirror compensation principle [26].

milling forces using the finite difference method (FDM) and compared results with FEM for Al 7075 alloy. FDM was found to give similar results as that of FEM analysis in Ansys; errors were found to be within 10% as compared to experimental values. The study also established that vibration of the thin-walled surface had no significant influence on part distortion; however, it significantly affected surface quality. The effect of cutting temperatures was not considered.

Du et al. [83] proposed an offline error compensation method to control deformations due to cutting forces for thin-walled parts of Al 6061. The analytical model

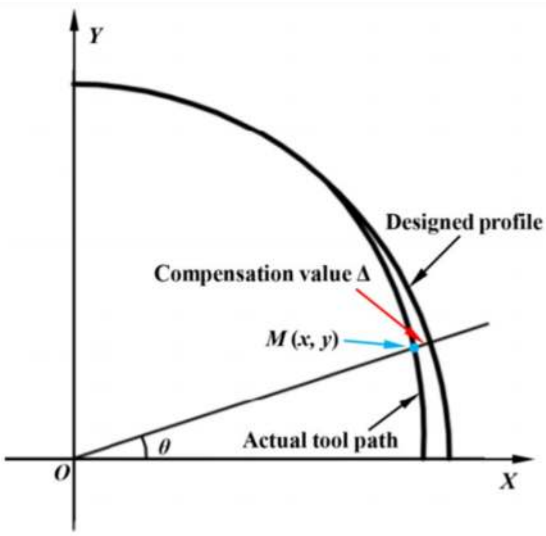

Figure 1.36: Principle of cutter location point compensation [26].

for cutting forces of peripheral milling was based on the Fourier series, whereas part deformations were optimized by an iterative FEM approach using APDL. According to the proposed strategy, cutting forces corresponding to the cutter engagement angle were calculated, and the corresponding deformation of the part was examined. Based on the result of part deformation, the decision to cut or change the cutting conditions was taken. The method was reported to give good results for deformation control.

Masmali et al. [84] put forth an analytical approach for modeling the dynamic chip thickness of thin-walled Al 6061 part in end milling. Cutting forces in normal to feed direction were only considered; Oxley's cutting force model and J-C model were used to model the cutting forces. The effect of change in the part stiffness due to material removal in each cutting pass was also considered. Finally, dynamic chip thickness at each cutting step was determined under the combined influence of cutting forces and workpiece stiffness. Differences in experimental and simulated results were attributed to several simplified assumptions, i.e., disregarding the effects of cutting force in the feed direction, workpiece wall damping, and assumption of the rectangular shape of the cutting chip.

Si-meng et al. [27] came up with a FEM-based technique illustrated in Figure 1.37

to predict the deformations of a thin-walled deep cavity 2A12 aluminum alloy part milling. The effect of the dynamic deflection of the workpiece and tool on the cutting forces was accounted for. The continuous dynamic state of the tool was modeled by a kinematic model of tool movement, and a hexahedral mapping algorithm was used for mapping the effect of deflection of corresponding nodes of the tool and workpiece on each other. Only forces in the radial direction were considered, whereas those in tangential and axial directions were ignored. The developed model was coded in the LS DYNA 3D software. The method was claimed to give an error of 15% in the values of predicted deformations.

Wang et al. [85] presented a method based on cutter workpiece engagement (CWE)

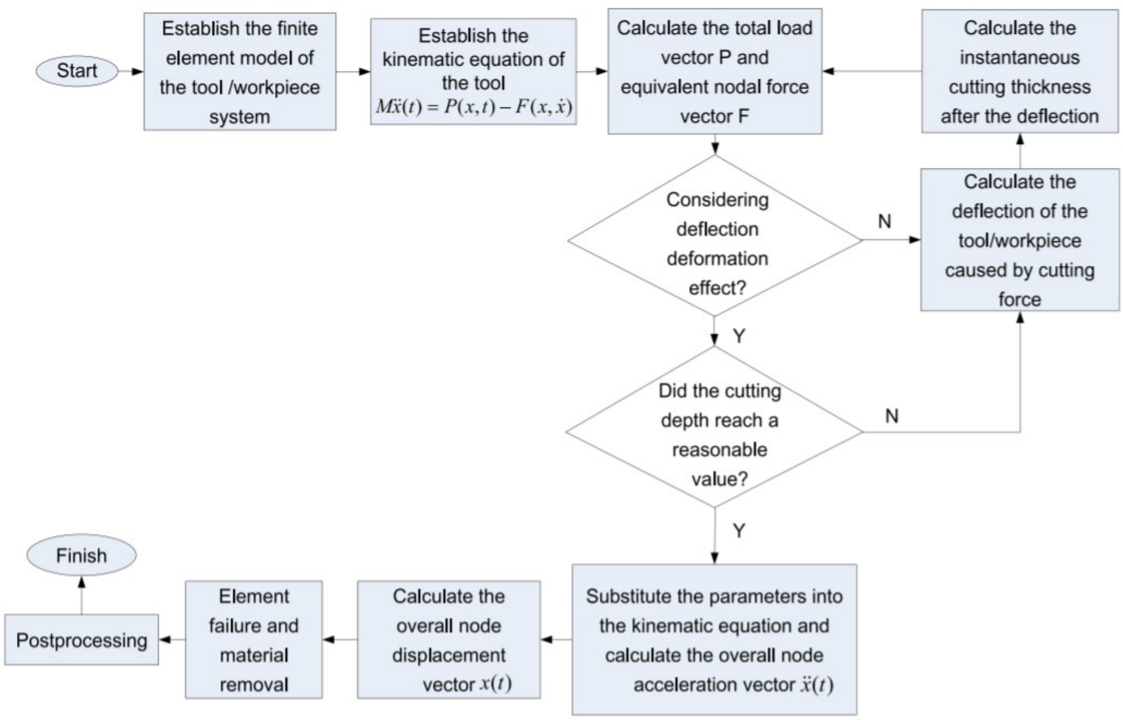

Figure 1.37: Procedure of the basic approach [27].

extraction to consider the deflection of the tool-workpiece system. Updated CWE allowed the estimation of actual cutting forces corresponding to each location of the tool. The deflections of the tool-workpiece system corresponding to different process cutting parameters were estimated by Ansys APDL. The cutter location data was obtained from computer-aided manufacturing (CAM) software. Based on that deflection value, the engagement of the cutter at each cutter location was found. The error between the simulated and experimental results was 13% to 25%; the same was attributed to neglecting the machining vibration and thermal loads.

Yue et al. [28] modeled machining error for thin-walled parts for single flute flank end milling operation for TC4 titanium alloy. The effect of workpiece deformation on tool-workpiece engagement and tool entry angle is illustrated in Figure 1.38 and Figure 1.39. An analytical model was used to determine the cutting force in the y-direction (transverse to feed). Based on the cutting force, part static deflections were calculated, and the corresponding change in tool entry-exit angle and, hence, the thickness of the chip was calculated. The cutting force and part deformations corresponding to the cutter rotation angle were calculated using an iterative algorithm. Milling surface error was estimated by taking into account the deformation of the workpiece corresponding to each engagement location of the tool. The predicted surface error was stated to deviate by 5% to 11% from the measured value. The predicted and actual profile of the machined surface is illustrated in Figure 1.40.

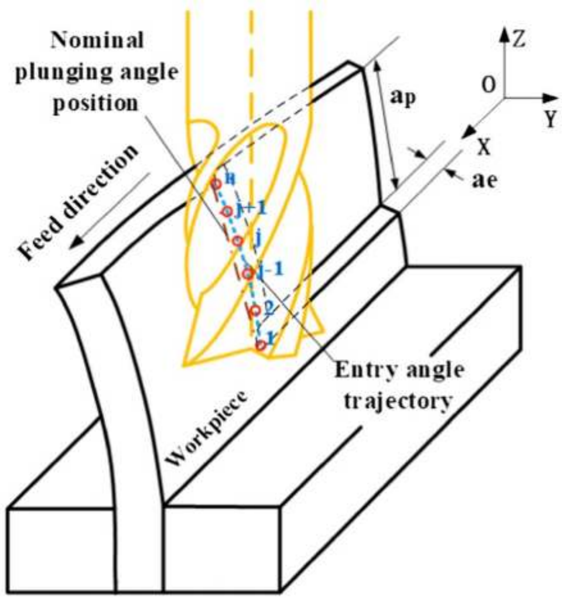

Figure 1.38: Effect of workpiece deformation on entry engagement of the tool [28].

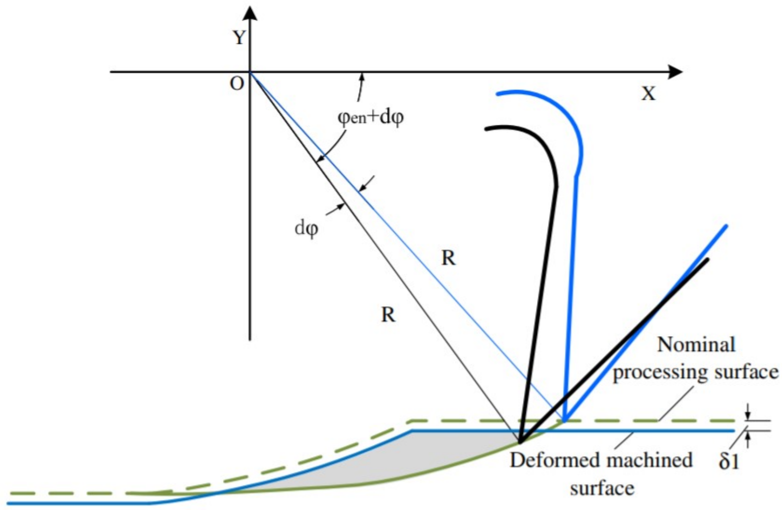

Figure 1.39: Effect of workpiece deformation on engagement of tool during cutting [28].

Hao et al. [29] used measurement data of part deformations for active control of

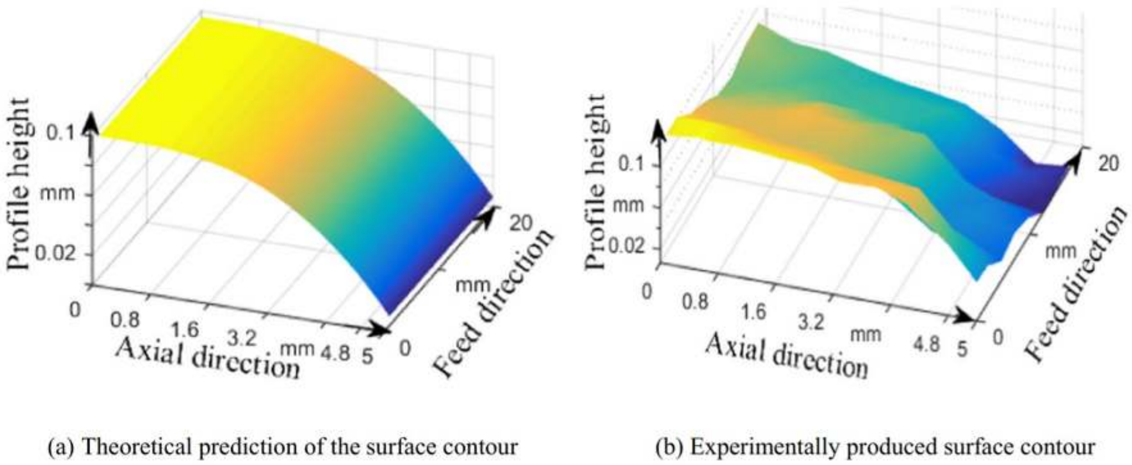

Figure 1.40: Predicted and measured profile of the machined surface. a) predicted contour b) measured contour [28].

pre-deformation in online mode. The proposed approach was validated on the Al 7075 aircraft structure part. Considering workpiece deformations as a gradual process, deformation data from the previous four machined layers was used to predict the following layer's deformation using the cubic spline fit. Monitoring of the deformation data was carried out by using the floating clamping system. Pre-determined deformation was applied to avoid distortion on stress release after the cutting pass using an adaptive fixture control system. The Kalman filter algorithm was employed for improving the accuracy of the prediction and control of deformations. Part deformations were reported to be considerably reduced by adopting the proposed methodology with a maximum error of 0.03 mm. However, the limitations of this methodology are that customized adaptive fixtures will be required for each part; this may not be economical, especially for profiled parts. The overall idea of the methodology is shown in Figure 1.41. Fei et al. [86] proposed a single-point

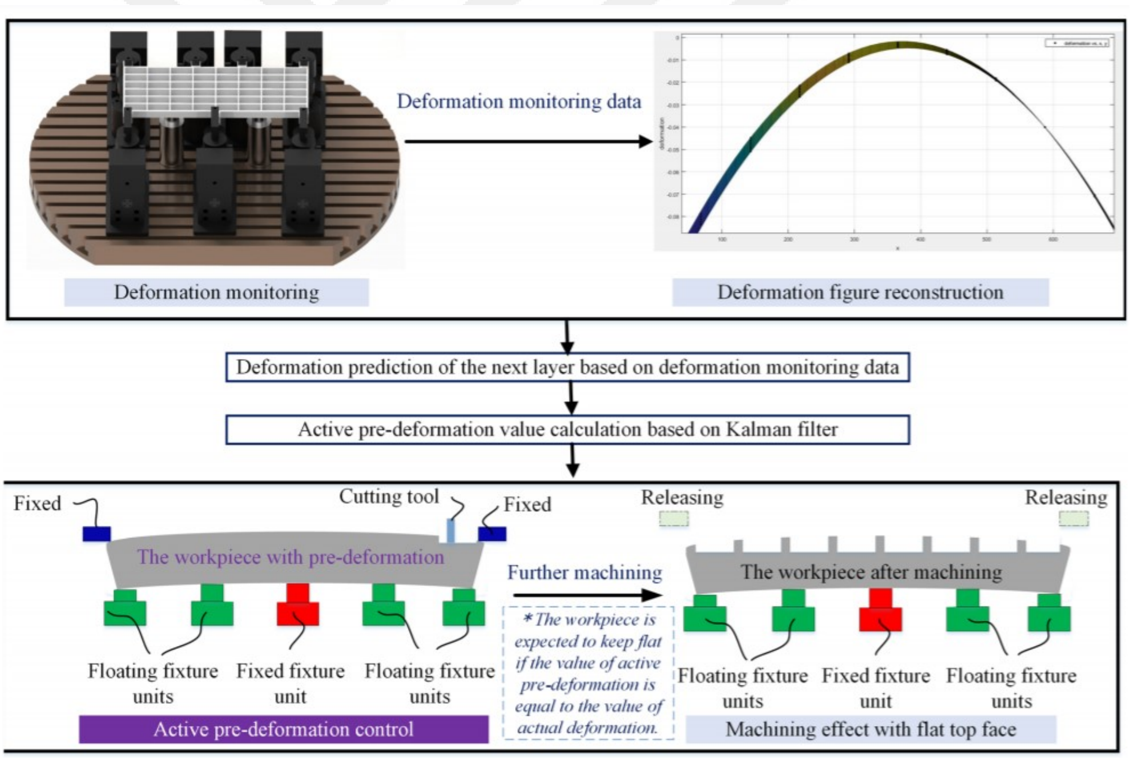

Figure 1.41: Overview of the proposed approach [29].

moving fixture support method to control thin-walled part deflections due to the cutting forces in the milling process. The proposed methodology was tested on simplified thin-walled part geometry. Though a reduction in the deflection of parts as compared to the un-supported case was reported, application of such a technique to complex engineering parts might require very sophisticated and customized designs of the moving fixture system.

Agarwal and Desai [30] presented a framework for the prediction of form error of the workpiece due to static deflection of the workpiece and tool. The schematic of measuring deflection and flatness error estimation is shown in Figure 1.42. A mechanistic force model was used for the calculation of cutting forces, and corresponding tool deflections were found from the static deflection theory of the cantilever beam. Ansys APDL was used to determine workpiece deflections corresponding to the calculated cutting forces. The points cloud of the tool and workpiece were then used to determine the error in the part's flatness. The outline of the complete methodology is illustrated in Figure 1.43. Their study also established the significance of consideration of tool, workpiece, and combined tool-workpiece deflections in determinations of flatness error. At large axial depths of cut, the effect of workpiece deflection was dominant due to reduced stiffness with the greater amount of removed material, whereas, at small axial depths of cut, the effect of tool deflection was dominant.

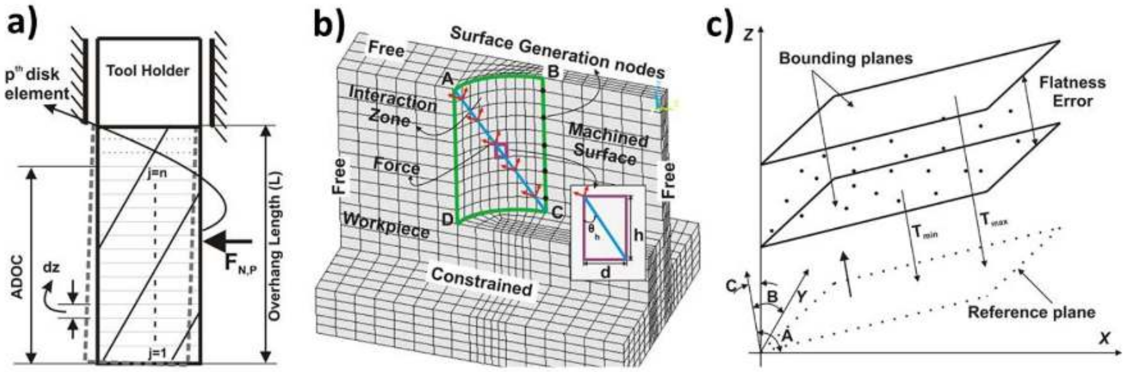

Figure 1.42: Flatness Error modeling: (a) tool Deflection; (b) deflection of workpiece; (c) estimation of error in flatness [30].

Discussion on static deflection mechanism

The above literature review confirms that static deflection of the workpiece and tool is a significant contributor to determining the final state of the machined sur-

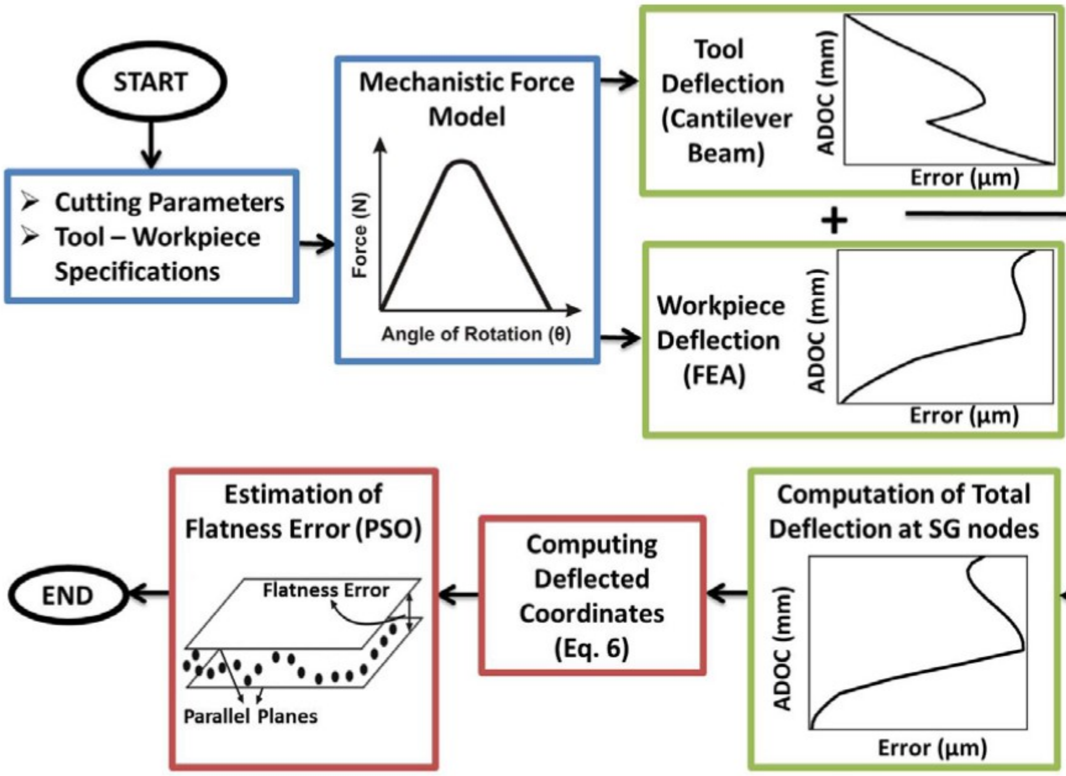

Figure 1.43: Methodology for estimation of flatness error [30].

face. Especially in the case of thin-walled machined parts, workpiece deflection needs to be considered for an accurate assessment of the machined part distortions. Although the available literature successfully established the importance of tool/workpiece static deflection in determining the quality of the finished part, certain limitations were also obvious. For the milling process, a simplified case of deflection of tool/workpiece in the y-direction (transverse to feed) was only considered, whereas deflection due to force in the x-direction (feed direction) was neglected. Since cutting forces in the x-direction are not negligible as compared to y-direction forces, ignorance of these forces might influence the accuracy of the results. Analysis of complex profiled parts was found to be another challenge limiting the consideration of this mechanism for the deflection of more realistic profiled components. Most of the studies were based on the analysis of simple T-shaped parts in which the deflection of the workpiece/tool was modeled as a cantilever under linear loads.

Thus, solutions related to more realistic workpiece shapes need to be developed to consider this aspect for real machining cases.

Some measures to control the effect of tool/workpiece deflection were also found in the literature. Online error compensation based on real-time measurement of deflection data and correction of tool path using the mirror compensation principle was found to give promising results. However, this technique needs to be further explored for more realistic part geometries. Another novel approach was to use an adaptive fixture system to apply pre-deformation to the parts to balance it with the deformation caused by the cutting process. However, the problem with this technique is the requirement of a separate fixture system according to the shape of each part. Furthermore, applying this technique to complex-shaped parts may not be easy.

1.3.5 Miscellaneous factors

In this section, studies that approached the problem differently are presented. Li and Melkote. [87] presented a clamping force optimization approach for quasi-static machining loads by considering the effect of the clamping forces on the error in the location of the part. The issue was addressed as an optimization problem in which an algorithm for clamping force optimization was proposed. The algorithm worked by reducing the error in the location of the workpiece by minimizing the weighted L2 norm of the resultant clamping force obtained using the contact mechanics model. Instantaneous milling forces were measured using a separately developed program and applied to the algorithm to account for the processing conditions. The algorithm was applied to a 3-2-1 clamping system to ascertain its effectiveness in optimizing clamping forces.

Song et al. [31] presented a method for predicting the dynamic stable lobe diagram (DSLD) in the milling process. Three parameters viz axial depth of cut, spindle speed, and tool position were considered while getting the stability lobe diagram as shown in Figure 1.44. The novelty in the DSLD-based method was the incorporation of change in the dynamics of the workpiece with tool position. It was stated that the proposed diagram was an improvement on the conventional stability diagrams, which took into consideration two parameters at a time. Workpiece time-dependent distortions were also analyzed for stable and unstable cutting conditions, as shown in Figure 1.45. Time-dependent distortions (measured after 170 hrs) of the thin wall part were shown to be considerably lower for stable conditions than unstable conditions for Al 7050 alloy.

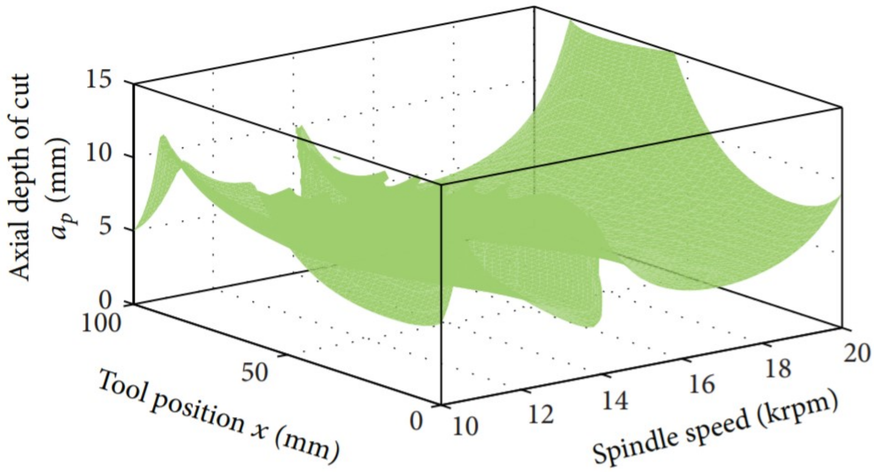

Figure 1.44: 3D stability diagram for the thin-walled part [31].

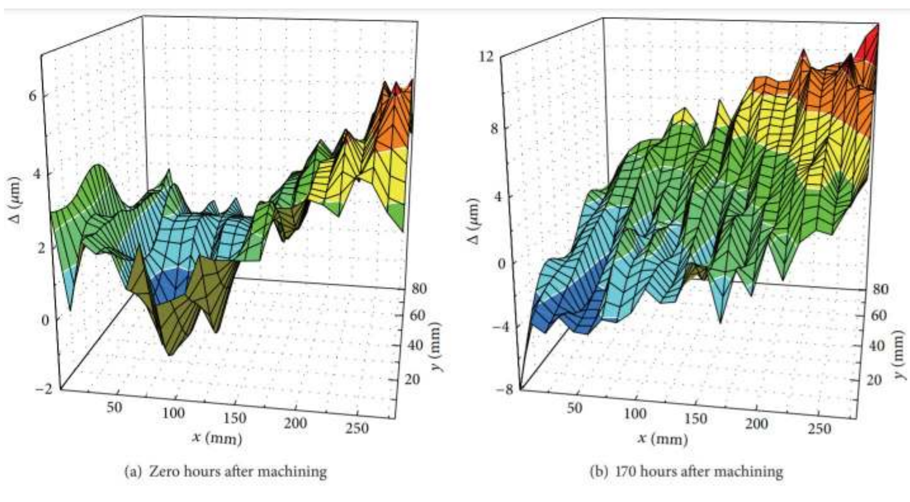

Figure 1.45: Distortions of machined part at different times after machining [31].

Liu et al. [32] presented an adaptive machining procedure based on interim measurement of part deformation to avoid any overcut in the following cutting pass, as shown in Figure 1.46. The methodology included measurement of the part in between the various machining passes and predicting the final state of the part theoretically based on those measurements as shown in Figure 1.47. The theoretical final state was then compared with the required dimensional tolerance requirements, and the decision was made on whether the process would lead to a qualified part. As a control measure, adaptive tool path adjustment based on the reconstructed part geometry was proposed for the in-process machining workpieces. Deformations of large thin-walled aluminum alloy parts were shown to be controlled using the proposed approach. Agarwal and Desai [33] compared the result of cutting coefficients

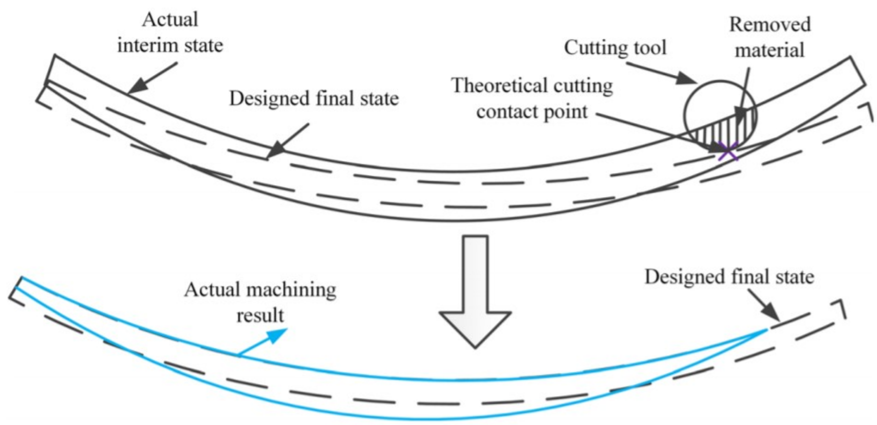

Figure 1.46: Overcut as a result of deformation of in-process workpiece [32].

of the end milling process obtained by mechanistic calibration and by a combination of mechanistic modeling and Artificial Neural Network (ANN). The presented approach is outlined in Figure 1.48. The latter method used ANN to relate the average cut thickness obtained from an analytical model with cutting coefficients. The only difference was that supervised ANN were used instead of a non-linear curve fitting function. Results of ANN were validated for Al 6061-T6 workpiece as shown in Figure 1.49. The results were reported to be better; however, no quantification of improvement was provided. Zhao et al. [34] presented a deep learning-based method

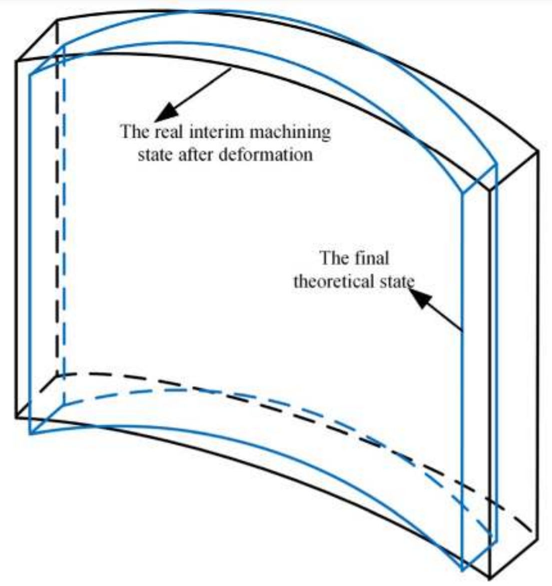

Figure 1.47: The deformation of interim machining state [32].

to predict and control distortions of an Al 7075 part. Monitoring data of process and part geometry were fed to the deep learning model. A deep learning model was trained by employing a conventional neural network (CNN) and a recurrent neural network (RNN). Monitored data related to part deformation, interim part geometry, and process parameters from 480 different aluminum parts of aircraft manufacturing industries was used for training. The extraction of relationships and features was carried out by CNN, whereas the deformation of the subsequent machining state was related to the current state of the workpiece by RNN. The methodology included the prediction of deformation of the next layer to be machined by the data obtained from the machining history of the previous parts, as shown in Figure 1.50. To feed sufficient data to the learning model, data augmentation techniques such as data rotation and translation were employed. The proposed model was reported to give an error of 10.61% as compared to 20% of a FEM-based study carried out with a relatively simpler part. Aurrekoetxea et al. [88] reviewed the literature on the prediction and control of distortion in machining. The lack of generality of the available approaches in terms of studied materials, structural shapes, and sources of distortions was highlighted as the major hindrance to distortion control. The

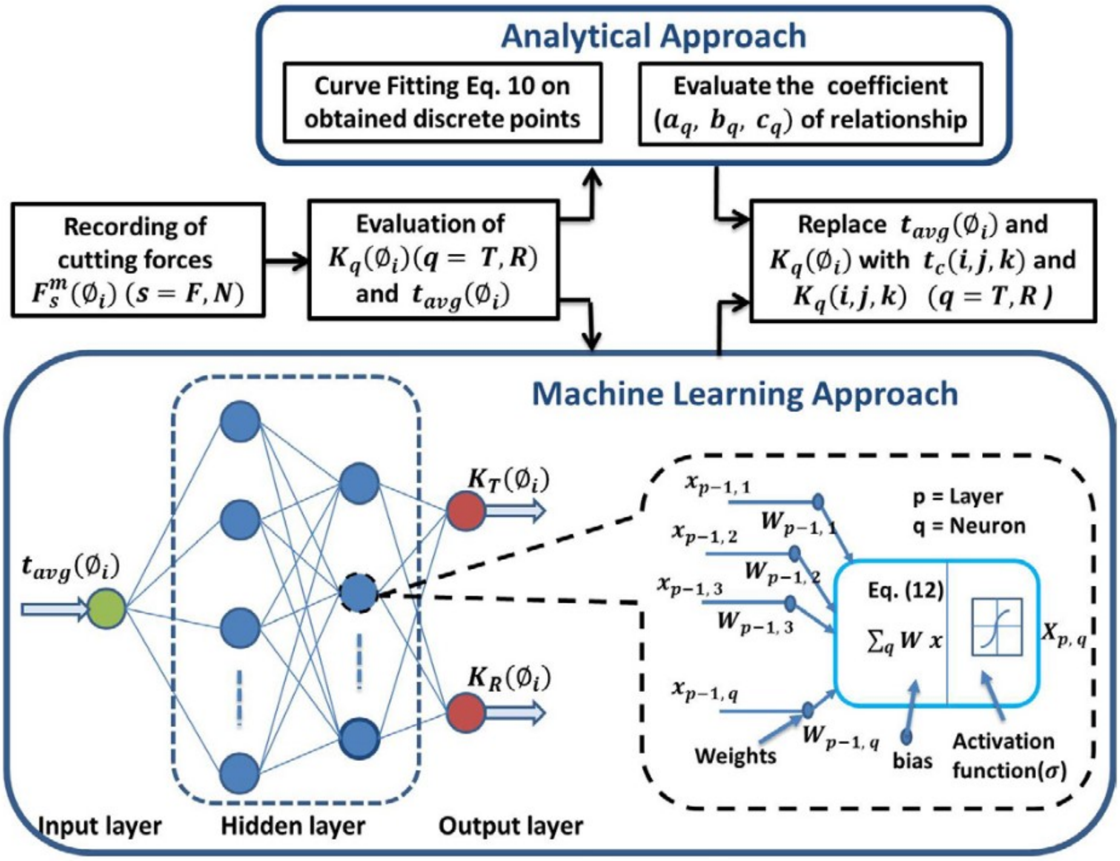

Figure 1.48: Calibration of cutting constants [33].

lack of generality of the available approaches in terms of studied materials, structural shapes, and sources of distortions was highlighted as the major obstacle to distortion control of machined parts. Smart clamping was identified as a potential solution to distortion control; however, the existing state of such systems was stated to be very premature. The complexity of models and lack of training data were identified as the main challenges for AI-based prediction and control of distortions. Optimizing part location and process sequence was reported as the most commonly applied strategy to control distortion. Furthermore, a difference of 19-50% between the predictions and experimental results of distortion was mentioned to be quite common.

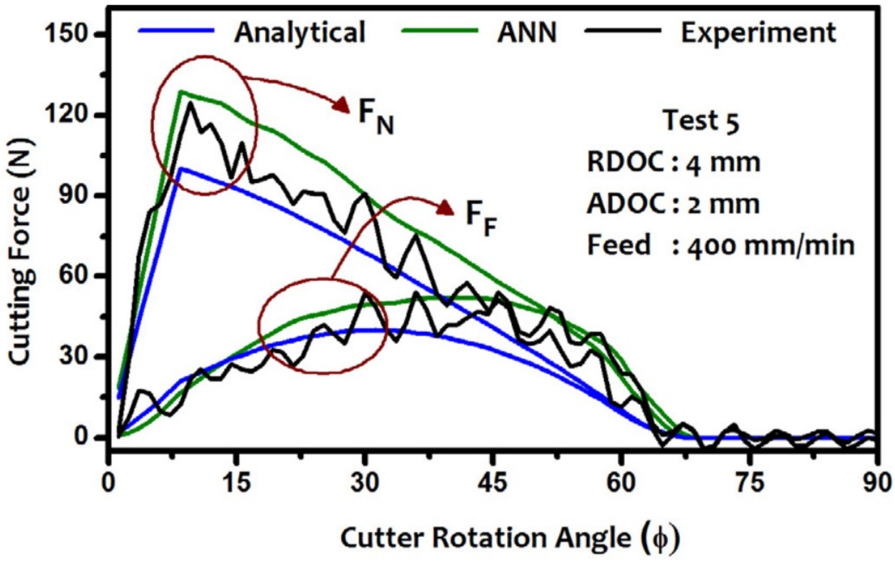

Figure 1.49: Comparison of measured and predicted forces [33].

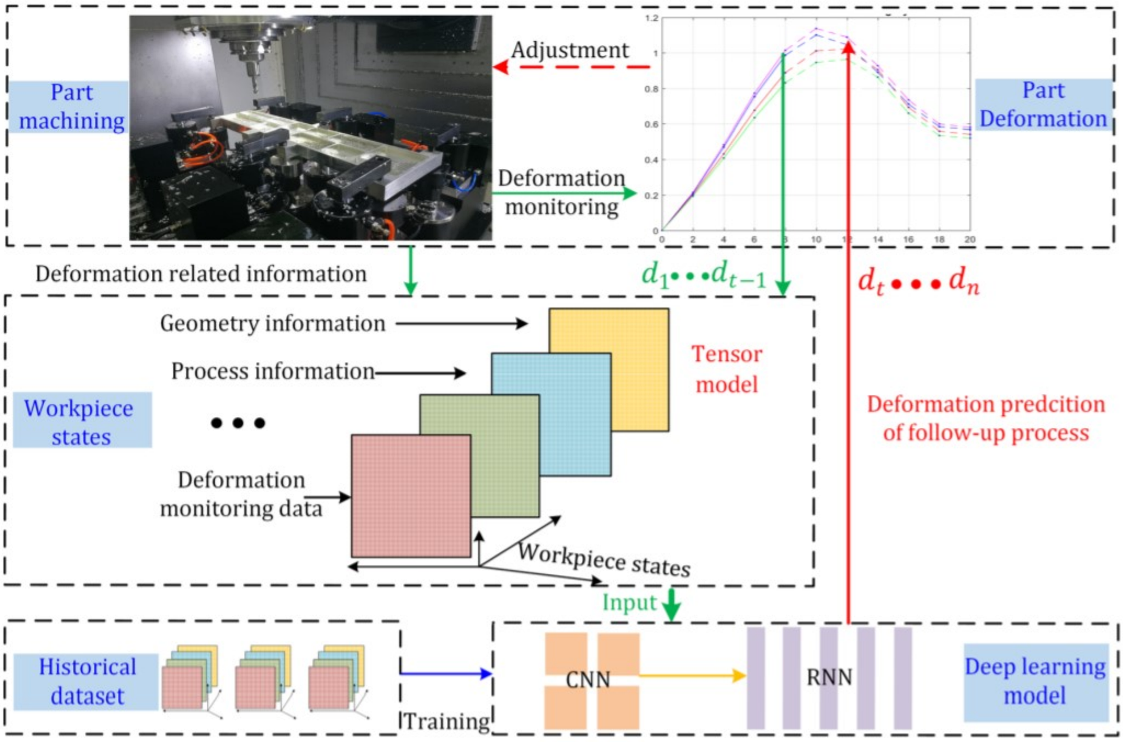

Figure 1.50: On-line part deformation prediction model [34].

Discussion on miscellaneous factors

The machining process is a thermo-mechanical phenomenon with complex dynamics that depend on several factors. It is a system with several components, e.g., machining equipment, cutting tool, workpiece material, clamping fixture, and coolant/lubricant. Each of these components has a bearing on the behavior of the final machined part. It is, therefore, quite understandable that improvement in the performance of each one of these improves the quality of the machined part. It can also be inferred from the review of this section that distortion of the final machined component can also be reduced in several ways other than controlling the IBRS, MIRS, or tool/workpiece deflection.

The studies reviewed in this section showed the control of distortions due to strategies like clamping force optimization, online deformation control based on the interim measurement of part during the process, control of chatter during the process using DSLD, and use of deep learning techniques for optimization of process based on the outputs of the model trained from historic machining data. However, each of these methods has its own merits and demerits.

The approach of controlling machining error by limiting part movement clamping force optimization was built on the assumption that the clamping force remains constant throughout the machining process. While this is possible for certain clamps, e.g., pneumatic or hydraulic, it is not the case for commonly employed mechanical clamps in which clamping force changes with workpiece deformation. Furthermore, the requirement of a separate clamping system for different jobs may limit its applications.

The approach based on interim measurement of the part may avoid the non-conformance of the part after complete machining. However, it is also a cumbersome technique to implement due to the requirement of removing the part during processing for interim measurements. Accurate measurement of the interim part geometry, reconstruction of the part geometry based on interim measurements, and reconfiguring the toolpaths based on the interim analysis require extra time. The cost of added time may limit its application in the competitive industry.

Another approach based on the deep learning-based prediction of distortion has the advantage of avoiding the time of taking measurements of residual stresses. Although the effect of only one process parameter, i.e., depth of cut, was analyzed in the presented study, it may be expanded to include other machining parameters. The challenge of this method is the requirement of a huge amount of data related to different types of parts and materials. Handling and processing many different data types is a difficult aspect of this method. Furthermore, the method relies on measuring part distortions using a responsive fixture, requiring separate fixture designs depending on the shapes of different parts.

1.4 Summary

A study of recent research is conducted on the prediction and prevention of distortions in machined aerospace components. Inadequacies in the state of the art are addressed, and significant discoveries are reported. Important findings from this review include the following:

- The distortions of machined components are influenced by a number of factors. All these mechanisms must be taken into consideration during the process design stage in order to appropriately regulate the machining operation.

- The main element affecting how aluminum alloy aircraft components deformed was the re-distribution of initial bulk residual stresses (IBRS) while machining. IBRS, however, were unable to explain the distortion behavior on its own fully. This emphasizes the value of taking into account additional factors, including machining-induced stresses (MIRS), tool/workpiece distortions, clamping systems, etc. Particularly in materials that are challenging to machine, MIRS play a key role in the distortion of machined components.

- One of the primary reasons for taking into account the role of MIRS in controlling component deformations is the absence of analytical models for residual stress estimations for typical machining operations. FEM can mimic machining-induced deformations, but it requires a lot of computation and is time-consuming.

- When a lot of material is removed, and there is a large re-distribution of stresses during the roughing step, IBRS play a dominant role in distorting the machined part. In contrast, MIRS are crucial during the finishing phase when minimal material is removed. When the component thickness is less than 4-5 mm for thin-walled workpieces, the role of MIRS becomes dominant.

- Effective characterization methods for each residual stress phenomenon are required to predict part distortions accurately. In particular, depth profiling of IBRS using the widely used chemical layer removal process inside the whole thickness of the machining blank is a highly laborious task for its effectiveness and precision; fast layer removal techniques like machining need to be further investigated. The availability of a database of IBRS depth profiles for these common materials and manufacturing processes, such as rolling, forging, quenching, annealing, etc., could also increase the effectiveness of the distortion predictions given that the majority of the raw materials used to create these blanks come from these standard processes.

- To correctly comprehend and simulate the machining processes and associated distortions, further work is needed. Although FEM is the most used method for computing MIRS, it has poor processing efficiency. Furthermore, the majority of FEM simulations take into account unrealistic constitutive laws of stress-free materials. To increase the precision of MIRS predictions, constitutive rules for materials with IBRS must be created and used. The development of more thorough analytical models for MIRS must be the main focus. For example, simpler situations of turning and milling are addressed by the analytical methods for predicting residual stresses that are now available. These models do not take into account the impact of one or more significant process elements, such as complicated tool geometries, cutting fluids, tool wear, tool coatings, etc.

- It is anticipated that the availability of more accurate predictive models for MIRS and depth profiles for IBRS adequate process planning may prove more practical as compared to the use of online deformation control strategies and customized toolings.

- Another process that has been demonstrated to significantly contribute to the size and surface imperfections of machined parts by several studies is tool and workpiece deflection. Certain simplified assumptions regarding the part shape and cutting mechanics were used to demonstrate the consideration of these factors. Further research must be done using more realistic cutting geometries and loading scenarios.

- It has also been demonstrated that online error control systems may also effectively manage distortion. However, these methods demand both highly specialized adaptive systems and technician knowledge. Additionally, it may not be time-efficient to repeatedly stop the process in the midst of machining for error correction.

- Data-based approaches, such as deep learning, have also been shown to be a possible resolve for machining processes regarding distortion control and process optimization. It is a relatively new approach in this field; there are still many obstacles to address in data collecting and processing.

Chapter 2

ANALYTICAL ALGORITHM FOR PREDICTION OF WORKPIECE TEMPERATURE IN END MILLING

2.1 Overview

Cutting temperature is crucial in machining since it directly influences cutting performance, residual stresses, workpiece distortions, tool life, etc. This chapter presents a novel analytical algorithm for fast prediction of workpiece temperature in intermittent cutting operations like milling. The drop in the workpiece temperature during the non-cutting interval is incorporated. The model also considers the variable chip thickness caused by the milling tool's trochoidal motion. The potential of the model to predict the workpiece temperature for different cutting conditions is demonstrated by validation testing with Ti6Al4V.

2.2 Introduction

Workpiece temperature prediction is essential from the standpoint of residual stresses, distortions, and overall surface integrity of the machined parts. Excessively high temperatures during machining may shorten the useful life of parts by generating residual stresses. For precision applications like aerospace and biomedical components, distortions and form deviations of parts owing to thermally induced stresses are highly undesirable. Therefore, it is vital for companies striving for high safety and accuracy requirements to understand and predict workpiece temperature. For this purpose, models can be developed that predict the workpiece temperature under specific process conditions. There has been considerable research on temperature prediction for continuous cutting operations like turning but not sufficient on intermittent cutting operations like milling.

Radulescu and Kapoor put forth an analytical model for determining cutting tool temperature fields [89]. Lazoglu and Altintas [90] developed a model for temperature prediction of chip and tool based on the finite difference method (FDM). The transient temperature field was treated a heat transfer system of the first order, and the response of the same was calculated by considering the time constant of the system and the initial temperature. The time constant of the system was calculated based the thermal characteristics of the material and the geometrical characteristics of the heat source. Saelzer et al. [91] studied how different cutting conditions affected rake face temperature in orthogonal cutting using an in-situ monitoring system. To evaluate different temperature measuring approaches, Aspinwall et al. [92] performed ball-end milling of γ-TiAl to monitor temperature under various tool wear situations. Byfut and Schroder [93] and Denkena et al. [94] predicted workpiece deformations during the NC-milling process. Calculations of the cutting force loads were made using geometry-based tool-workpiece contact modeling. The workpiece temperature and thermal deformations were then calculated using these loads in the finite element model (FEM). For milling, geometric-based heat input modeling was done by Schweinoch et al. [95], FDM was employed to simulate the temperature of the workpiece. A semi-analytical model for tool temperature in milling was presented by Lazoglu and Bugdayci [96]. The numerical model based on finite differences used forces that were computed analytically. An FDM-based model for the 3D temperature fields of the workpiece, tool, and chip in case of both continuous and interrupted machining was proposed by Islam et al. [97]. The thickness of the shear zone, cut chip thickness, and the thermal diffusivity of the workpiece material were used to compute the workpiece's time constant. Green's function-based analytical approach was put forth by Karaguzel et al. [98] to predict tool temperature during intermittent cutting. The temperature of the tool was stated to rise with the increase in the radial depth of cut and the cutting speed.

According to the above literature review, most milling models address the temperature prediction of the cutting tool; furthermore, most are based on FEM or FDM approaches. It is crucial to devise computationally efficient analytical models that are simpler to use. Komanduri et al. [99] presented an analytical model to predict temperature of chip and workpiece. The model was built by considering the cutting heat as a band heat source moving in a semi-infinite medium. The model has been frequently used for estimating the temperature of the workpiece in a continuous cutting process, i.e., turning. The same model was employed by Wan et al. [100] and Zhou et al. [101] to determine the workpiece temperature field in milling. However, in its original form, this model, because of its boundary conditions, applies to continuous machining, i.e., turning. The interrupted aspect of the process must be included for using it for discontinuous cutting operations, e.g., milling.

This chapter describes a new analytical algorithm for estimating the workpiece temperature during the milling operation. The analytical algorithm proposed here takes process interruptions into account. The drop in the temperature of the workpiece in the non-cutting periods is considered. Experiments on the Ti6Al4V material are used to validate the results of the model.

2.3 Analytical algorithm for workpiece temperature

A typical configuration of an end milling process is shown in Figure 2.1. For calculating the workpiece temperature at any point P at a distance s from the current location of the tool, the linear travel domain of the tool is discretized in the angular domain with prescribed intervals of engagement and non-engagement. When the tool is engaged, the rise in temperature of the workpiece is calculated by employing the moving heat source model as in Komanduri and Hou [99]. On the other hand, when it is not engaged, the workpiece's temperature drop is accounted for by treating it as a heat transfer system of first order.

2.3.1 Workpiece temperature during tool-workpiece engagement

The temperature increase in the workpiece caused by the heat generation at the shear plane is computed by considering it as a heat source moving through a semi-infinite medium as follows:

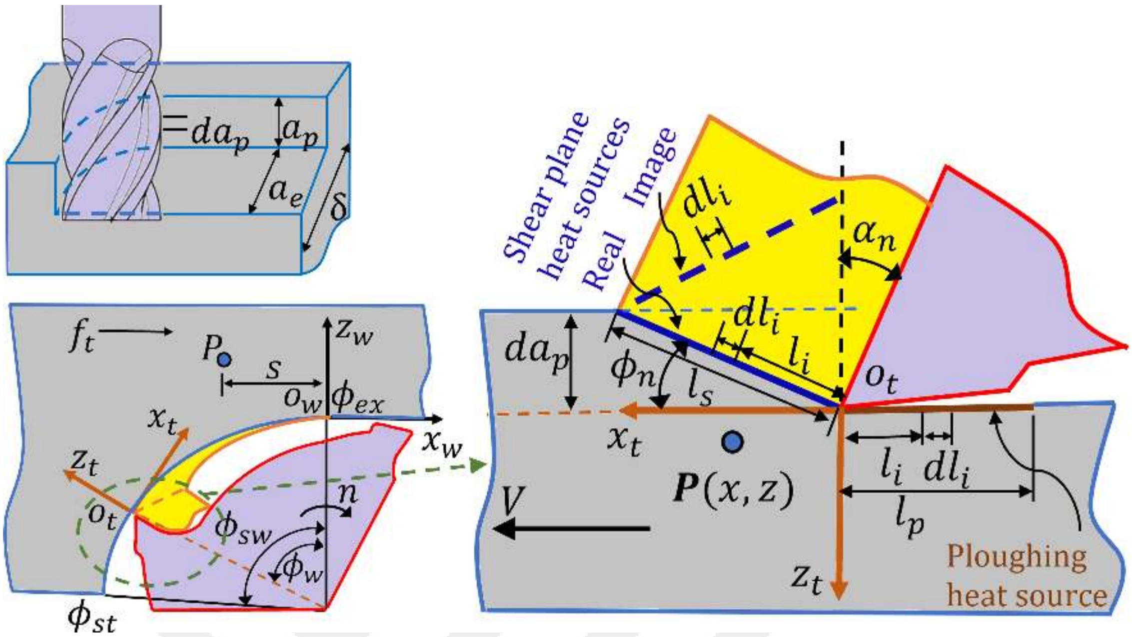

Figure 2.1: Representation of the end milling process.

$$T_{sh}(x,z) = \frac{q_{shear}}{2\pi k_{wp}} \int_0^{l_s} e^{-\frac{(x - l_i \cos\phi_n)V}{2a_{wp}}} \left[K_0 \frac{V}{2a_{wp}} \left[\sqrt{(x - l_i\cos\phi_n)^2 + (z + l_i \sin\phi_n)^2} + \sqrt{(x - l_i\cos\phi_n)^2 + (z + 2da_p - l_i \sin\phi_n)^2} \right] \right] dl_i \tag{2.1}$$

where l_s represents the shear plane length and x and z represent the position of the point P in the coordinate system of the cutting tool. k_{wp} and a_{wp} represent thermal conductivity and the thermal diffusivity of the workpiece, and K_0 is the modified Bessels function of second type zero-order. V, da_p, and ϕ_n are cutting velocity, discretized axial depth of cut, and normal shear angle according to the oblique cutting mechanics presented in [102]. Provided the diameter of the tool D and its current angle of immersion ϕ_w are available, the coordinates of P can be transformed from the workpiece coordinate system to the tool coordinate system as follows:

$$\begin{Bmatrix} x_t \\ y_t \\ z_t \end{Bmatrix} = \begin{bmatrix} \cos\phi_w & 0 & \sin\phi_w \\ 0 & 1 & 0 \\ \sin\phi_w & 0 & \cos\phi_w \end{bmatrix} \begin{Bmatrix} x_w \\ y_w \\ z_w \end{Bmatrix} + \begin{Bmatrix} -(D/2)\sin\phi_w \\ 0 \\ -(D/2)(1-\cos\phi_{w)} \end{Bmatrix} \tag{2.2}$$

The shear heat source intensity, q_{shear} is formulated as:

$$q_{shear} = \frac{F_s V_s}{l_s \; da_p} \tag{2.3}$$

To account for the change in thickness of the chip caused by the helix angle β of the tool, discretization of the total force due to shearing is carried out over the axial length of the tool at each angular increment:

$$dF_s = dF_t \cos\phi_n - dF_r \sin\phi_n \tag{2.4}$$

$$\begin{pmatrix} dF_t \\ dF_r \\ dF_a \end{pmatrix} = da_p \begin{pmatrix} K_{tc}h_c \\ K_{rc}h_c \\ K_{ac}h_c \end{pmatrix} \tag{2.5}$$

where dF_t, dF_r, and dF_a are the discretized values of the tangential cutting force, radial cutting force, and axial force, respectively, in the tool coordinate system. K_{tc}, K_{rc}, and K_{ac} are the corresponding cutting coefficients identified via mechanistic calibration. The uncut chip thickness, h_c is determined based on the feed per tooth, f_t, and the tool's current immersion angle, ϕ_w:

$$h_c = f_t \sin\phi_w \tag{2.6}$$

The shear plane length l_s and velocity on shear plane V_s are determined as:

$$l_s = \frac{h_c}{\sin\phi_n \cos\phi_i} \tag{2.7}$$

$$V_s = \frac{V \cos \alpha_n}{\cos(\phi_n - \alpha_n)} \tag{2.8}$$

α_n and ϕ_i are normal rake angle and oblique shear, respectively [102]. The increase in workpiece temperature caused by the tool flank's plowing action against the recently cut surface is expressed as [101]:

$$T_{pl}(x,z) = \frac{q_{pl}}{2\pi k_{wp}} \int_{-\frac{l_p}{2}}^{+\frac{l_p}{2}} h_p \, e^{-\frac{(x+l_i)V}{2a_{wp}}} \left[K_0 \frac{V}{2a} \sqrt{(x+l_i)^2 + z^2} \right] dl_i \tag{2.9}$$

The plowing heat source intensity is:

$$q_{pl} = \frac{P_{cut} V}{l_p a_p} \tag{2.10}$$

According to Waldorf et al. [103], the plowing heat source length l_p and the plowing forces in the direction of cutting velocity P_{cut} and the thrust direction P_{thr} are computed as:

$$\begin{pmatrix} P_{cut} \\ P_{thr} \end{pmatrix} = a_p \begin{pmatrix} K_{te} \\ K_{re} \end{pmatrix} \tag{2.11}$$

Here, K_{te} is the edge coefficient in the cutting direction, and K_{re} is the edge coefficient in the radial direction. The ratio of heat partition is calculated after [100] as:

$$h_p = \frac{\sqrt{k_{wp}\rho_{wp}c_{wp}}}{\sqrt{k_{wp}\rho_{wp}c_{wp}} + \sqrt{k_t\rho_t c_t}} \tag{2.12}$$

where ρ_{wp}, c_{wp} are the density and specific heat capacity of the workpiece material while k_t, ρ_t and c_t are thermal conductivity, density, and specific heat capacity of the tool.

2.3.2 Workpiece temperature calculation for non-engagement intervals

The model for the temperature of the workpiece presented in the previous section is built on the formulations of a band-shaped heat source traveling in a semi-infinite continuous body. The milling process is characterized by intermittent cutting of the material. There are regular intervals of cutter-workpiece engagement and non-engagement during the process. This requires that a drop in temperature of the workpiece being taken place during the non-cutting time between two subsequent engagements must be allowed before the temperature begins to increase again as a result of the subsequent engagement of the tool. To incorporate this decrease in temperature during the non-cutting intervals, the workpiece is considered a heat transfer system of first order. For such a system, the time constant τ can be found based on the material's thermal diffusivity and the geometrical parameters of the heat source as stated in [90]. By taking into account the heat loss from the 2D plane given by the workpiece's wall thickness in the radial depth of cut direction and axial depth of cut direction as δ and a_p, respectively, the time constant can be obtained as follows:

$$\tau = \left[a_{wp} \left(\frac{\pi^2}{a_p^2} + \frac{\pi^2}{\delta^2} \right) \right]^{-1} \tag{2.13}$$

Prior to calculating the temperature evolution as a result of the tool progressing towards the point P (Figure 2.1), the domain of calculation is discretized by employing the algorithm shown in Figure 2.2. This discretization is carried out on the basis of cutting parameters, including the spindle speed n, number of cutting edges N, feedrate f_t, radial depth of cut a_e, and cutter pitch angle ϕ_p. Following the definition of the domain for calculation, the evolution of workpiece temperature is carried out by using the algorithm given in Figure 2.3.

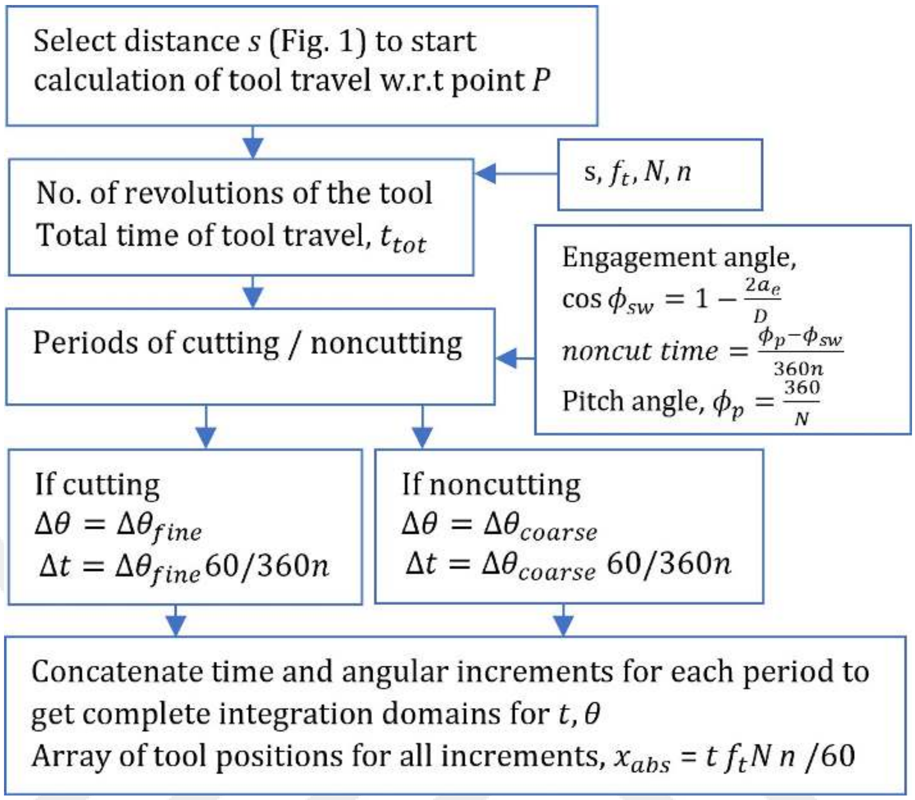

Figure 2.2: Discretizion of temperature calculation domain.

2.3.3 Simulation results

Figure 2.4-2.6 provide the temperature prediction results under different cutting conditions. Simulations done on a laptop took a few seconds when $\Delta\theta_{\text{fine}} = 0.1°$ and $\Delta\theta_{\text{coarse}} = 1°$ were defined for the engagement and non-engagement intervals, respectively. The model gives the results of the impact of different parameters on cutting temperature in line with the literature. Figure 2.4 illustrates the effect of the system's time constant on the evolution of workpiece temperature. Higher radial depth of cut is characterized by a thicker workpiece wall, causing the time constant to be higher, i.e., 132 ms, which is quite large when compared to the non-cutting interval of 4.1 ms. The large time constant prevents the workpiece from reaching the room temperature prior to the beginning of the next engagement, thus leading to a higher rise in temperature. The effect of the increase in cutting speed and feedrate reflects in the form of increased temperature of the workpieces as can be observed

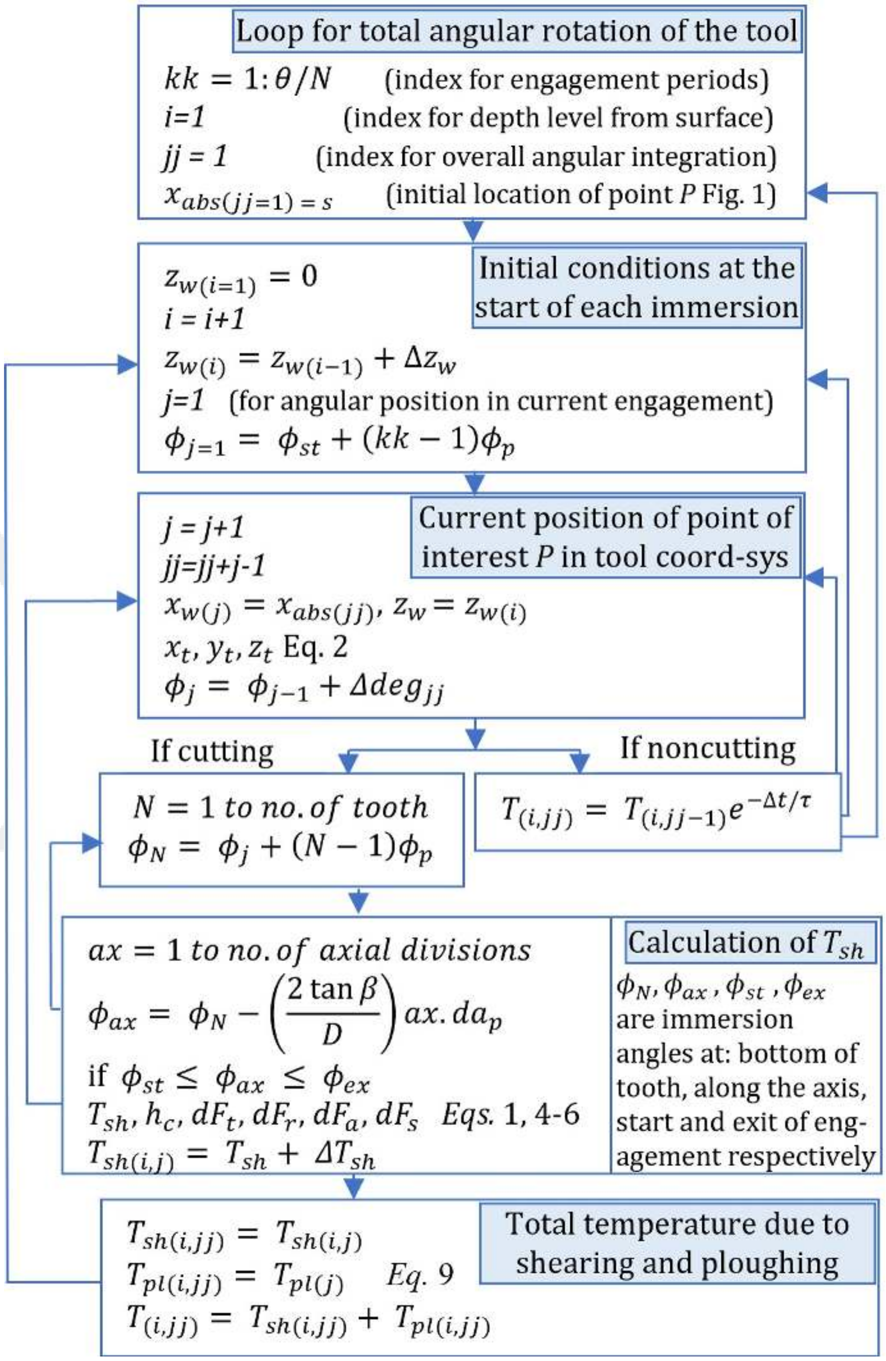

Figure 2.3: Calculation of evolution of temperature in milling.

in Figure 2.5 and Figure 2.6, respectively.

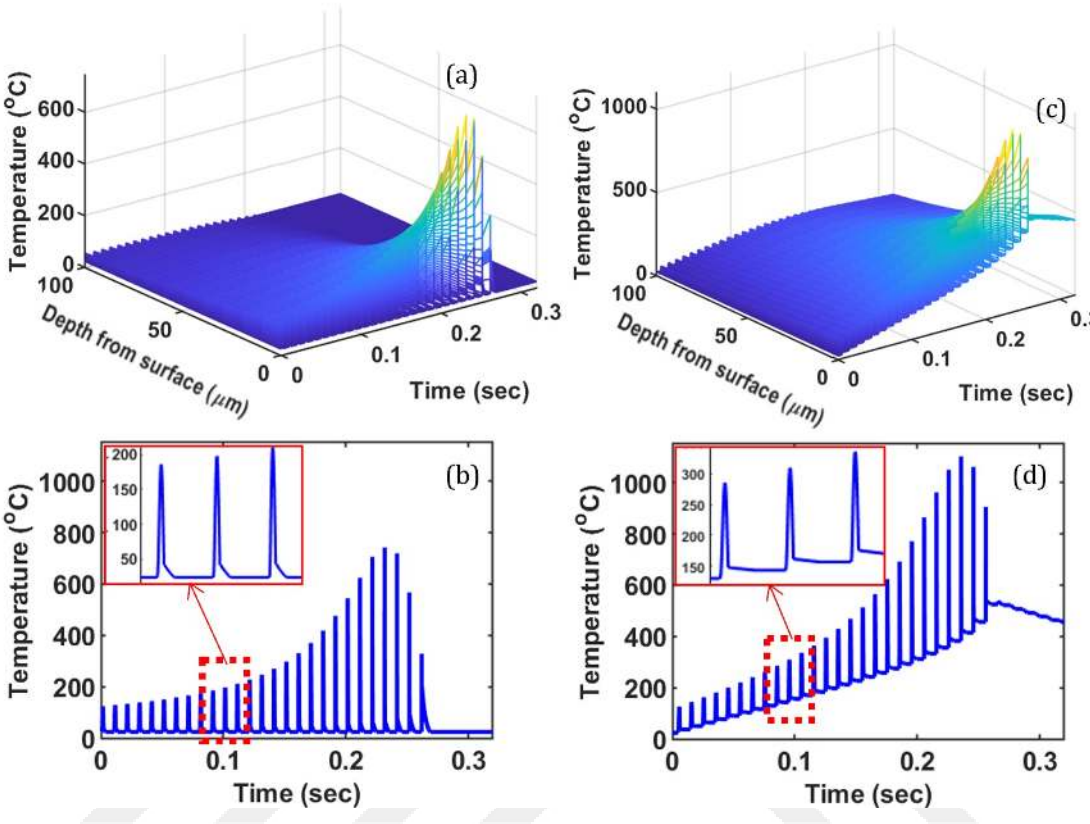

Figure 2.4: Workpiece temperature corresponding to different radial depths of cut. (a) and (b) $a_e = 0.2mm$, (c) and (d) $a_e = 2mm$. (b) and (d) temperature values at the surface.

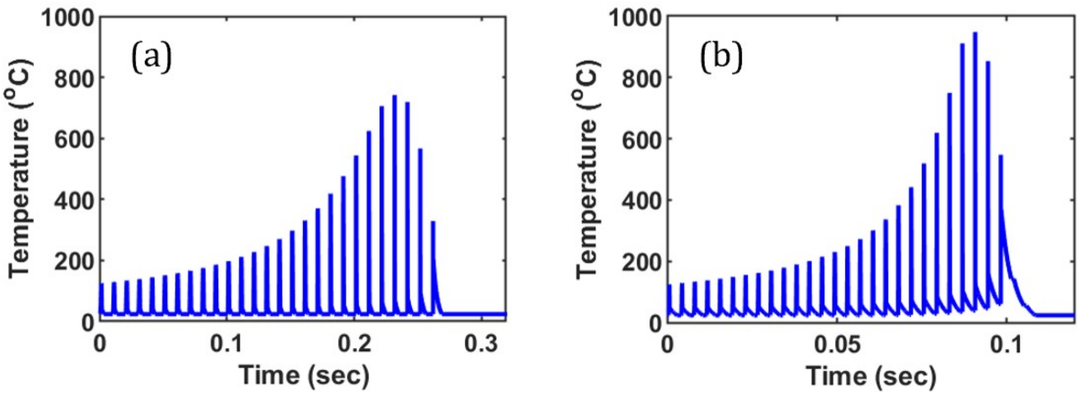

Figure 2.5: Effect of cutting speeds on temperature at workpiece surface (a) $V = 47m/min$ (b) $V = 125m/min$.

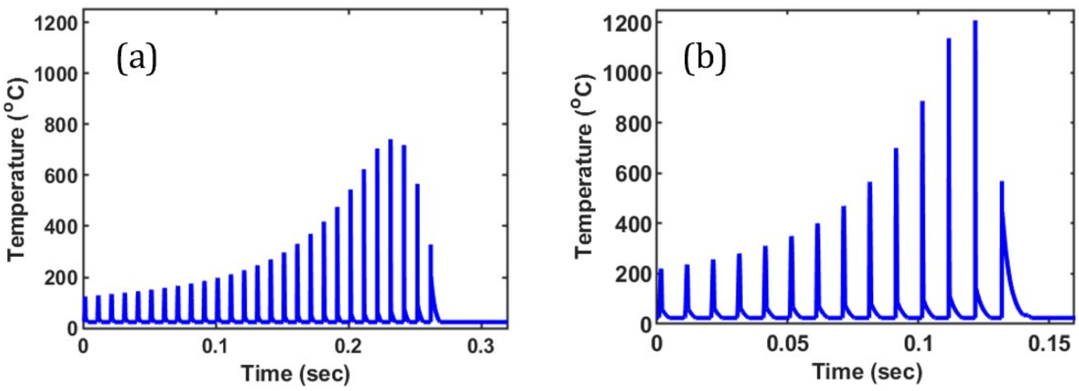

Figure 2.6: Effect of feedrate (feed per tooth) on temperature at workpiece surface (a) $f_t = 0.06mm$ (b) $f_t = 0.12mm$.

2.3.4 Experimental validation

Milling of the Ti6Al4V workpiece using carbide tools was performed on a Spinner 5-axis CNC machine. The four fluted endmills had a diameter of 10 mm, helix angle of 36°, rake angle of 6°, and cutting edge radius of 10 μm. Figure 2.7 provides an illustration of the experimental setup. Table 2.1 and Table 2.2, respectively, provide the physical characteristics of the materials and the cutting parameters for validation testing. Four K-type thermocouples with 90 μm wire diameters were used to monitor temperature, and a Kistler 9257B dynamometer was used to measure cutting forces. To obtain precise force coefficients for the workpiece-tool pair, mechanistic calibration tests were also conducted. Figure 2.8 illustrates the comparison of the experimental and simulated forces.

Table 2.1: Material properties for Ti6Al4V and carbide tool.

Property	**Ti6Al4V**	**Carbide tool**
Thermal conductivity, k (W/mK)	6.7	62
Specific heat capacity, c (J/kgK)	526	234
Density, ρ (Kg/m^3)	4430	13000

The comparison of predicted and measured temperature results is provided in

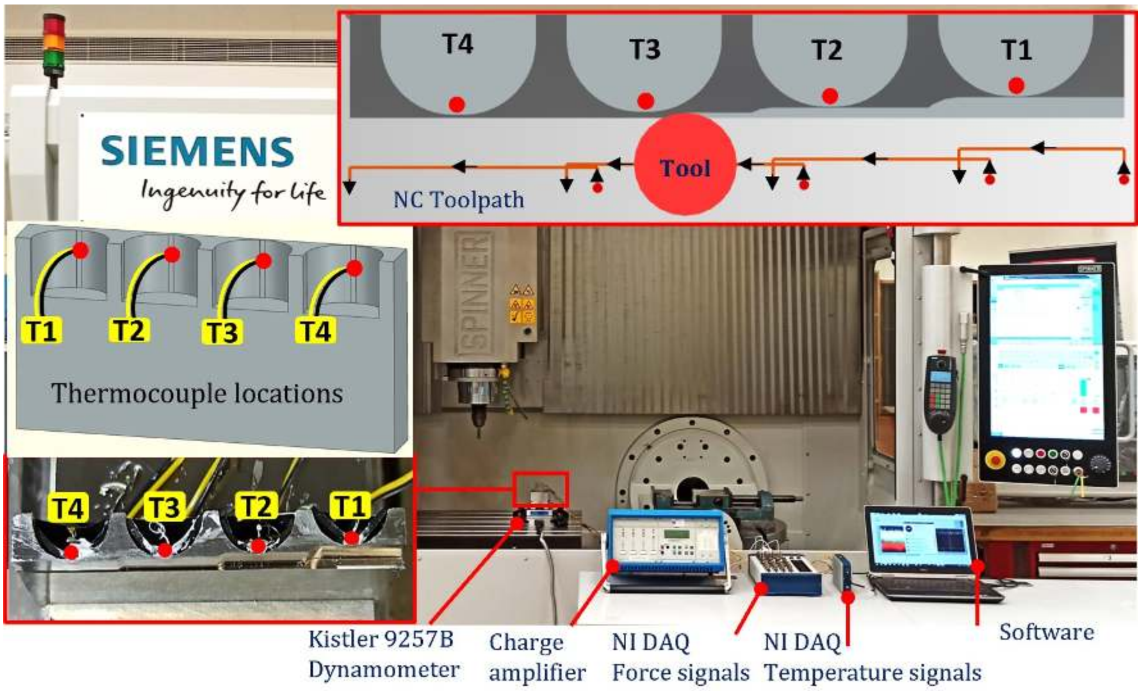

Figure 2.7: Setup for experimental validation cutting force and temperature measurements.

Table 2.2: Cutting parameters for validation tests.

Nomenclature	Test 1	Test 2	Test 3	Test 4
Cutting speed, $V(m/min)$	47	47	47	125
Feed per tooth, $f_t(mm)$	0.06	0.06	0.12	0.06
Radial depth of cut, $a_e(mm)$	0.2	2	0.2	0.2
Axial depth of cut, $a_p(mm)$	5	5	5	5
Thermocouple distance from the machined surface (μm)	60	60	90	90

Figure 2.9. The illustrated results are related to thermocouples located at specified distances from the surface being machined. The measured maximum temperatures agree with the predicted values. The small shift in thermocouple location is believed to be the source of the difference. Only the maximum values of the workpiece temperatures are presented because these are considered the most reliably measured.

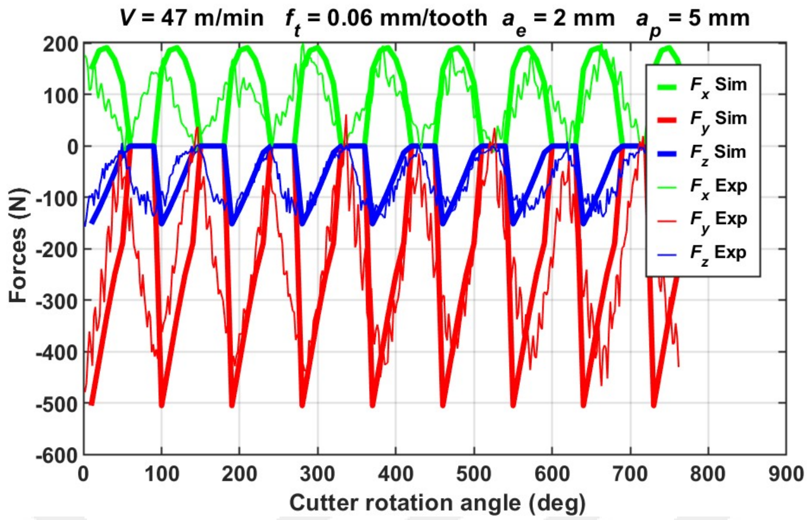

Figure 2.8: Comparison of calculated and measured cutting forces.

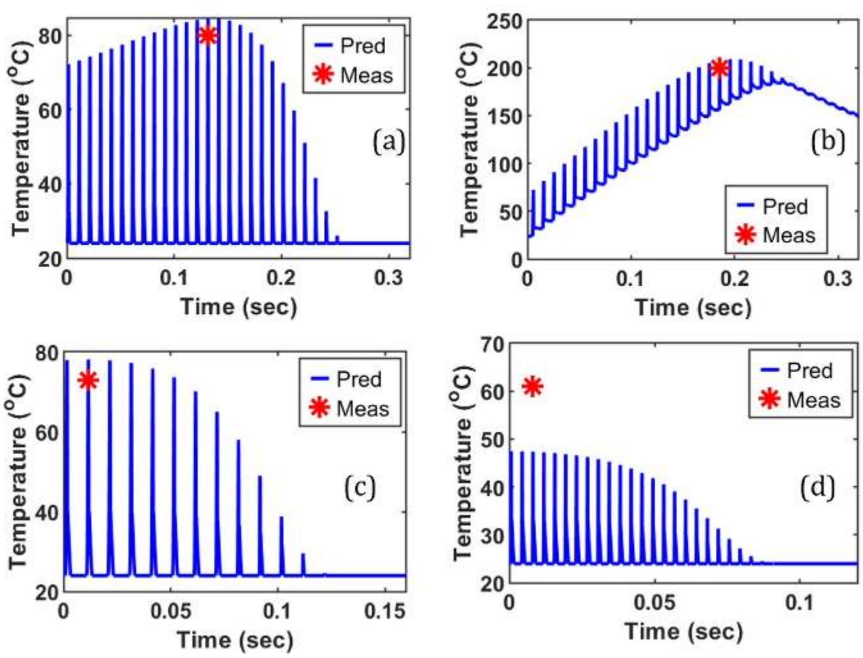

Figure 2.9: Predicted vs measured workpiece temperature. (a) Test 1 (b) Test 2 (c) Test 3 (d) Test 4.

The reason for this is that the relatively large time constant of thermocouples (30 ms) in comparison with the intervals of tooth passing, which ranged from 3.75 ms to 10 ms could affect the measurement of drop in temperature during the non-cutting intervals.

2.4 Summary

The temperature of the workpiece during end milling is predicted by the proposed analytical model. The ability of the model to consider the drop in the temperature of the workpiece during the non-engagement periods gives it a novel character. When compared to the tests, the temperature predictions are quite promising. Cutting temperature tends to rise with increasing feedrate and speed due to the increase in the intensity of heat sources. On the other hand, the rise in temperature with increasing radial depth of cut is primarily the result of the increase in the time constant of the system. Due to its analytical character, the proposed algorithm allows fast prediction of workpiece temperature and may also be applied in prediction algorithms for machining-induced residual stresses in milling.

Chapter 3

CRACK COMPLIANCE METHOD FOR INITIAL BULK RESIDUAL STRESS MEASUREMENT

3.1 Overview

Techniques for measurement of residual stresses in the thickness of the material are well established. Both destructive and non-destructive methods are available to determine the residual stresses inside the material. Common non-destructive methods include X-ray diffraction, Neutron diffraction, and Synchrotron diffraction techniques [104]. The non-destructive methods, on the other hand, include hole drilling, deep hole drilling, ring coring, contour, and crack compliance methods. All these methods assume that the stress is distributed uniformly in each plane in the thickness of the material. Each of these methods has its limitations in measuring stresses near the surface or deep in the thickness direction of the material. A comparison of the depth ranges of some of these stress measurement techniques is presented in Table 3.1 [35]. The use of non-destructive methods, such as diffraction techniques for measuring the through-thickness residual stress profile of the material, requires the tedious task of carefully removing layers of the material without generating any additional stresses. Furthermore, the cost of specialized diffraction equipment used in these methods is relatively high. On the other hand, destructive methods are relatively fast and do not require very specialized equipment. Among these, the crack compliance method has been recognized as a simple, fast, and accurate method with good repeatability. This method is flexible enough to measure stresses in various materials such as metals, plastic, glass, and crystal. Furthermore, it can be employed for different geometries such as blocks, plates, beams, rods, rings, and tubes [36]. This chapter delineates the crack compliance method used to measure the through-thickness profile of initial bulk residual stresses (IBRS) in this thesis.

Table 3.1: Measurement range in depth of the material for different techniques [1].

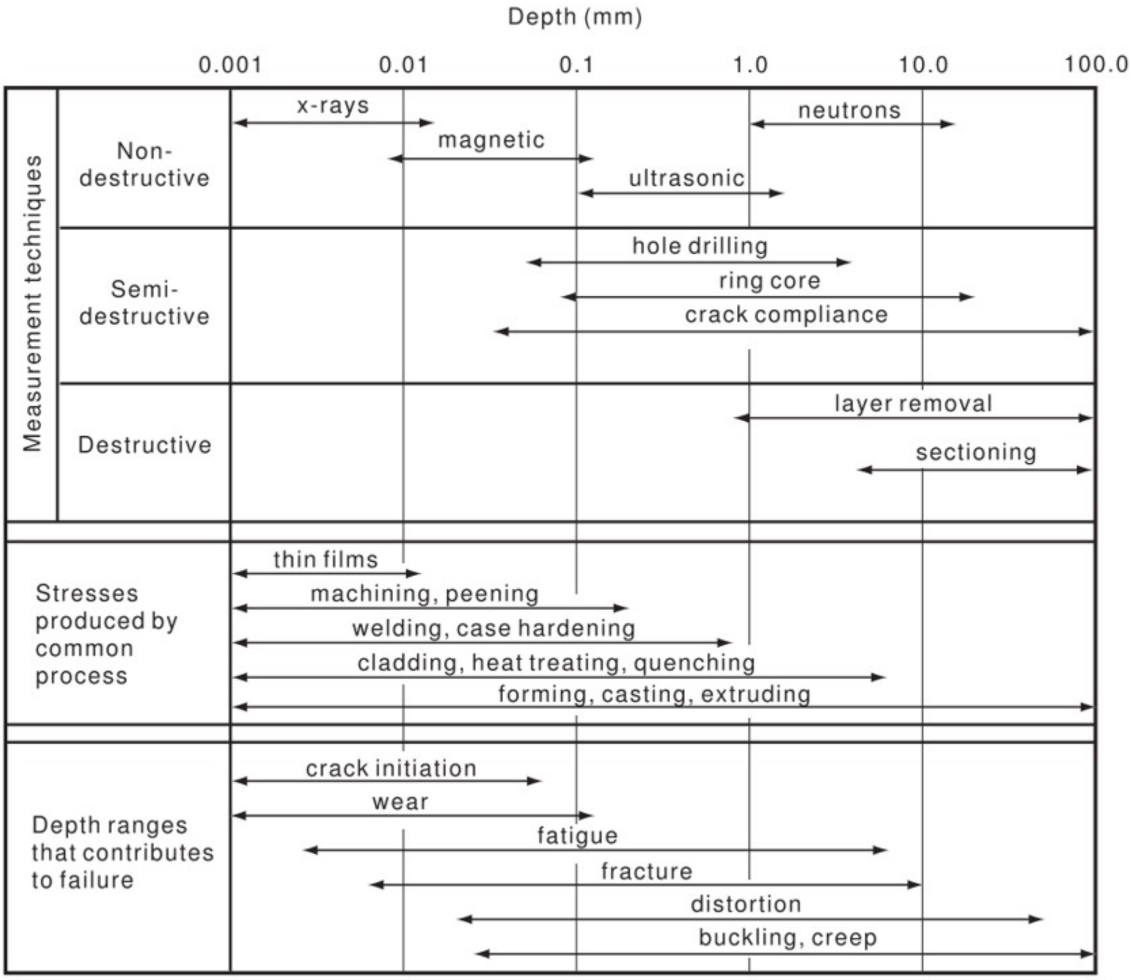

3.2 Introduction of the crack compliance method

The crack compliance method for residual stress measurement is originally derived from Bueckner's superposition principle [35]. In the context of stress measurement, it can be stated that the superimposition of the stress change to the changed stress state of the blank gives the original stress state of the material. The illustration of this principle in the context of residual stress measurement is given in Figure 3.1 [105]. The original stress state **A** of the material is to be measured. Partitioning the blank from the half at section $x = 0$ causes deformation due to the release of residual stresses, resulting in a partially relaxed state of stress **B**. If this stress state is superimposed with another stress state **C** which can bring the stress-free deformed shape to its original flat face, the superposition of these two stress states will give the original stress state **A** of the material such that $\sigma^A = \sigma^B + \sigma^C$. In the context

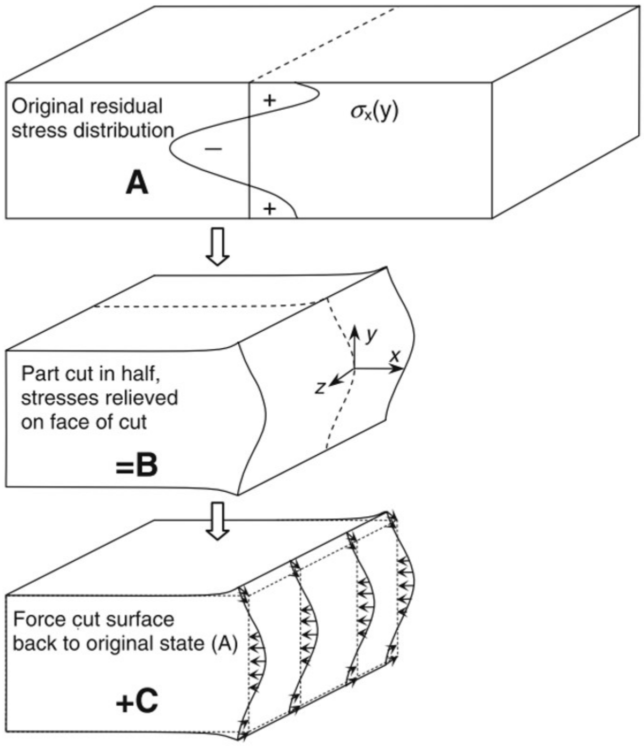

Figure 3.1: Bueckner's superposition principle [35].

of fracture mechanics, Buekner established that the extension of a crack is governed by the stresses present on the crack propagation surface. Alternatively, if a crack is propagated only under the influence of the internal stresses of the material, equal but opposite tractions applied to the surface of the crack leading to its closure would give the original stresses in the material.

3.3 Calculation of residual stress profile

The crack compliance or slitting method developed initially by Finnie and co-workers [36] is capable of measuring the in-plane normal component of the stress in the material. Incremental cutting of a planar slit is carried out in the depth of the specimen for which the through-thickness residual stress profile is to be determined. The strains resulting due to the release of residual stresses during incremental slit cutting are measured using strain gauges. These measured strains are then used to determine the normal stress existing in the material before cutting off the slit.

The method is comprised of two parts: a forward solution and a backward solution. In the forward solution, the strains due to the extension of a slot in a material with a known stress state are calculated. These strains corresponding to different slot depths and known stress states are called compliance functions and are determined with the help of the finite element method (FEM). On the other hand, the stress state related to the strains measured during the slot extension process is determined in the backward solution. A polynomial series expansion is commonly used to relate the measured strains with the profile of residual stress in the material. This problem of relating the stresses in the depth of the material with the measured strains is thus reduced to finding the unknown coefficients of the polynomial series.

3.3.1 Theoretical formulations

Figure 3.2 shows a rectangular block sample for which the residual stress profile is to be measured by the incremental slitting process. The dimensions of the block are length L, width B, and thickness t whereas, a and w are the depth and width of the slit, respectively. Here, l is the gauge length, and s represents the distance between the slitting plane and the center of the strain gauge. The determination of stress component $\sigma(x)$ requires the measurement of the strain $\epsilon(a)$ corresponding to each slit depth a. Successive measurement of strains corresponding to each incremental slit depth leads to the stress profile in the thickness of the material. Legendre polynomial basis has been mostly used in the literature to relate the measured strains with the material stress. The residual stress is represented in terms of these Legendre functions as:

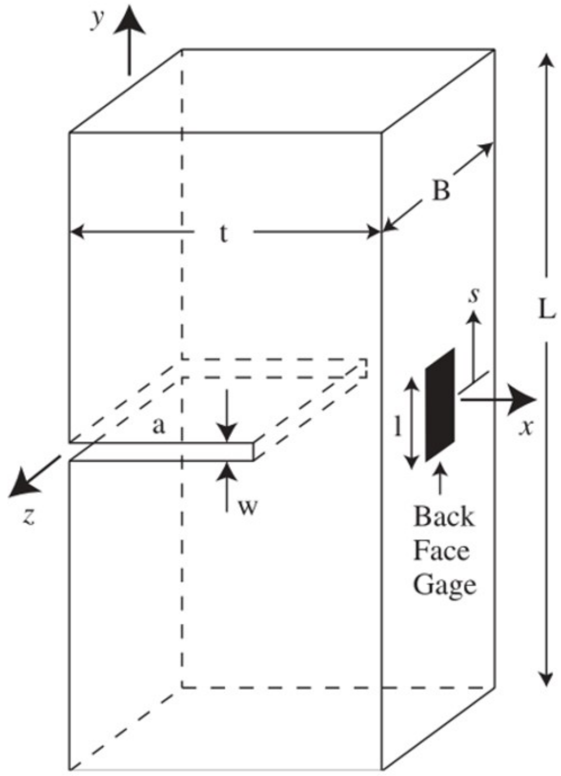

Figure 3.2: Block geometry for slitting [36].

$$\sigma(x) = \sum_{j=2}^{m} A_j P_j(x) \tag{3.1}$$

where $P_j(x)$ are the Legendre polynomial functions; the details of these functions are available in Appendix 'A'. A_j are the unknown coefficients of the polynomial terms that best relate the stress to the measured strain at the depth x. j is the order of the polynomial terms, with m being the highest order decided during data reduction through error minimization. Generally, the value of m between 4 and 12 represents the residual stress profiles of the materials with sufficient accuracy [36]. The coefficients A_j are determined using the measured strains and compliances calculated by FEM. Assuming linear elastic behavior, the compliance matrix C is a linear system that relates the unknown coefficients of the basis function with the measured strain. Each element C_{ij} of the compliance matrix represents the strain ϵ

at the location of the strain gauge for a certain slit depth a_i when the residual stress σ is exactly equal to the Legendre polynomial term P_j such that:

$$C_{ij} \equiv \epsilon(a_i)_{|\sigma=P_j(x)} \tag{3.2}$$

Using the principle of superposition, the strain resulting from the residual stress in Eq. 3.1 is given as a function of slit depth a_i as:

$$\epsilon(a_i) = \sum_{j=2}^{m} C_{ij} A_j \tag{3.3}$$

By inverting Eq. 3.3 in the least square sense, the unknown coefficients of the terms of the basis functions can be found by using the pseudoinverse and the measured values of the strain ϵ_{meas}:

$$\{A\} = [([C^T][C])^{-1}[C^T]]\{\epsilon_{meas}\} \tag{3.4}$$

where, $\{A\}$ is the vector of coefficients of the basis function, $[C]$ is the matrix of compliances and $\{\epsilon_{meas}\}$ is the vector of measured strains.

3.3.2 Finite element modeling for calculation of compliance matrix

To determine the compliance matrix using FEM, a simple static strain analysis is carried out. The FE model is established according to the actual dimensions of the sample and the slit. For each slit increment, different pressure loads corresponding to different orders of the stress function are applied on the surface of the slit, and corresponding strains at the locations of the strain gauges are determined. Each strain value corresponding to each pressure load and depth of the slit gives an element of the compliance matrix. In this research, the FE modeling of the slitting process was carried out in Abaqus. FE modeling was carried out for each of the four samples (one sample for each direction of the 23 mm and 50 mm thickness blanks). The details of FEM analysis for one of the samples, i.e., the sample for measuring stress profile in the transverse direction of the 50 *mm* thick sample, are only presented. The dimensions of the sample were 212 x 38 x 50 mm, as shown in Figure 3.3. Due to the symmetry on both sides of the slit, only one side of the specimen was modeled, as shown in Figure 3.4. Since the propagation of crack under the action of internal stresses and the resulting release of stress is considered a purely elastic phenomenon, the elastic modulus and Poisson's ratio of the material were only defined to represent the mechanical behavior of the material.

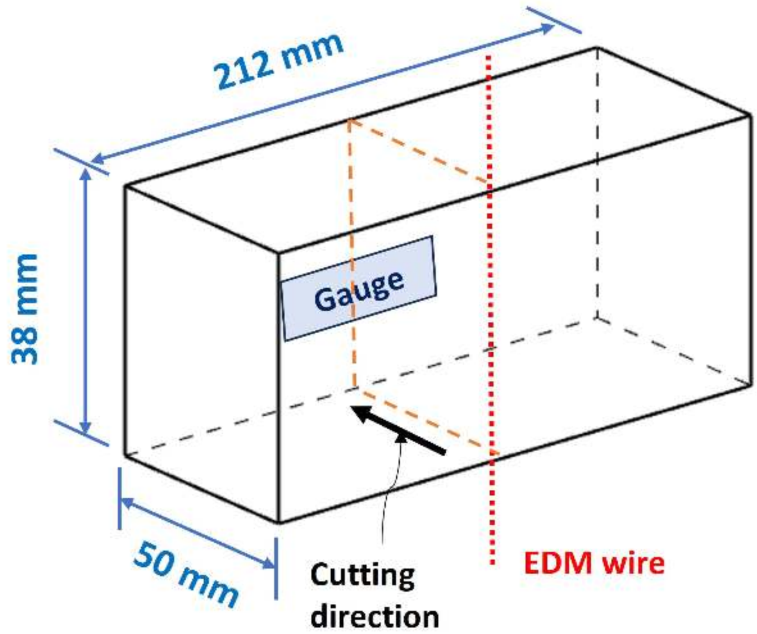

Figure 3.3: Schematic of the slit cutting process and sizes of the sample.

The meshing of the model was carried out with 6664 quadratic quadrilateral elements of type CPE8R, having a total of 20339 nodes. The fine mesh was defined in the regions closer to the slit, whereas coarse meshing was done far from the slit regions to avoid excessive computation time, as shown in Figure 3.5. Boundary conditions were defined as displacement constraints along the slit (Y-dir) and normal to the slit (X-dir) direction as shown in Figure 3.6.

Material removal due to each increment slit cutting was simulated by deleting corre-

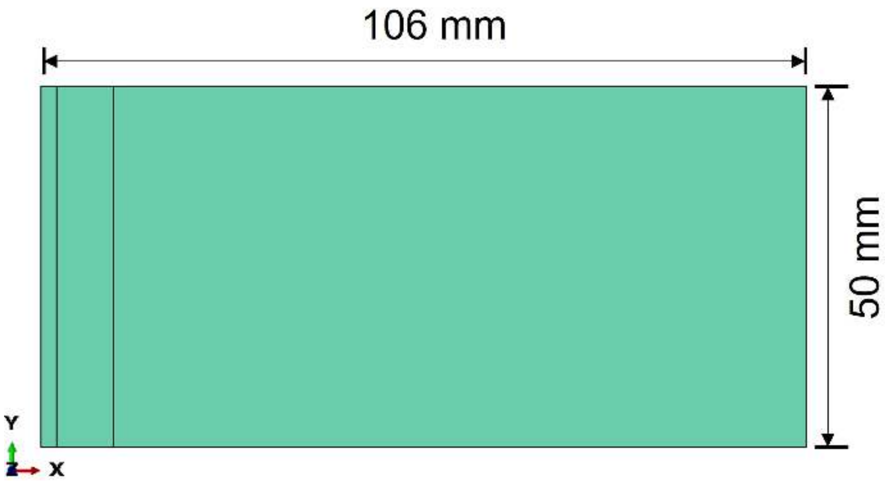

Figure 3.4: FEM model of the sample.

sponding elements in the FE model as shown in Figure 3.7. The deletion of elements also released the displacement boundary conditions applied to the deleted elements hence representing the free crack surface.

For each slit depth, different stresses corresponding to different polynomial orders were applied as pressure loads on the slit surface. The strain corresponding to each load case was determined by processing the data of change in the distance between the nodes representing the strain gauge in the FE model. Figure 3.8 shows the applied stresses and deflections corresponding to different applied load cases.

3.4 Experiment for strain measurement

3.4.1 Experimental procedure

A brief outline of the experimental setup for stress measurement with a single strain gauge is presented here. Detailed guidelines about the experimental steps can be found in [106].

1. The sample for residual stress measurement is cut according to the sizes, and references are marked for the strain gauge installation.

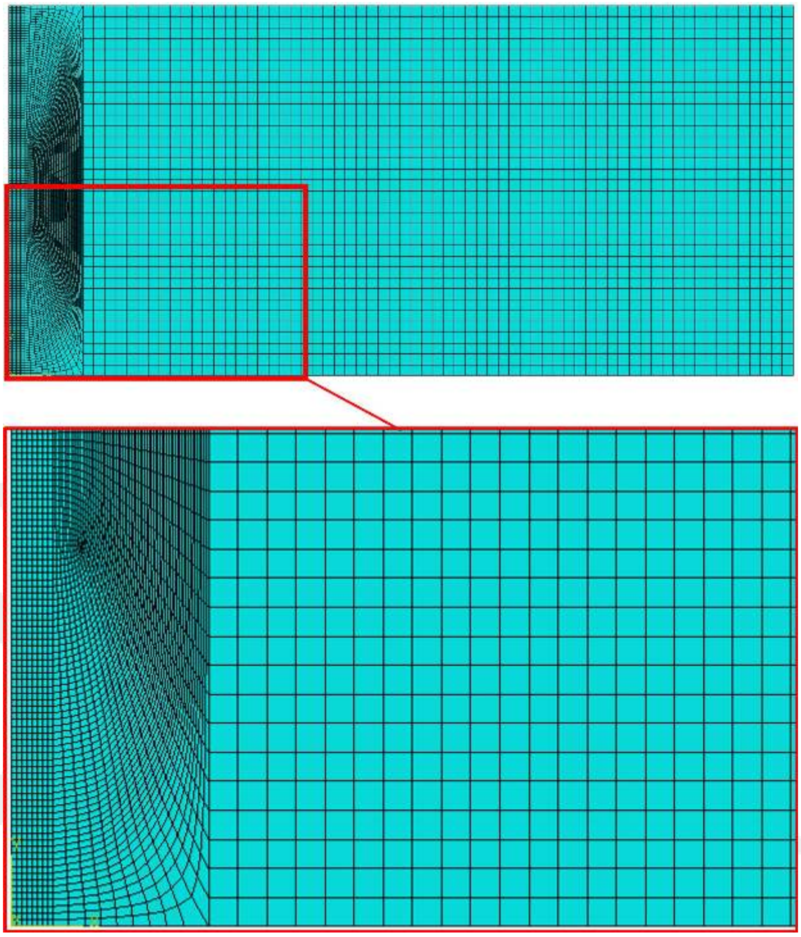

Figure 3.5: Meshing of the FEM model.

2. The strain gauge is installed and isolated from external contacts using waterproof coatings.

3. A data acquisition system is established for the measurement of strains. Proper grounding of the circuit/data acquisition system is essential to avoid any errors in strain measurements.

4. The sample is clamped on the WEDM (wire electric discharge machine) from one side while the other is left hanging in the air. The sample is aligned such that the EDM wire is parallel to the surface on which the slot is to be cut and perpendicular to the direction in which the strains are to be measured.

Figure 3.6: Displacement boundary conditions in X and Y directions.

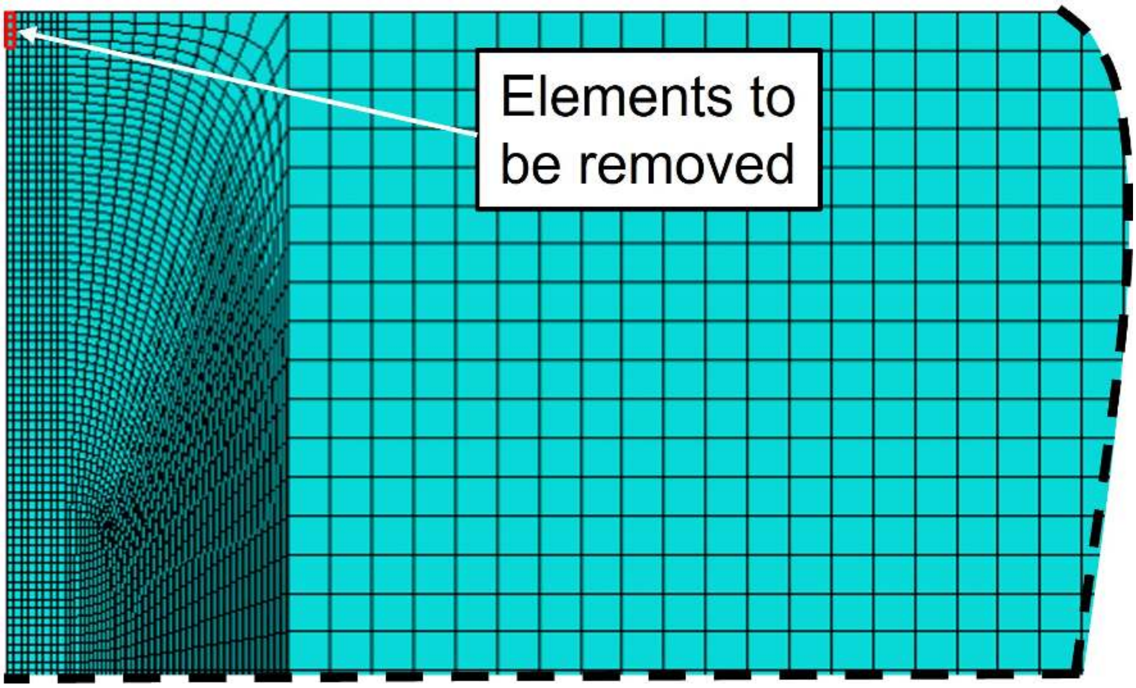

Figure 3.7: Elements to be deleted to simulate the material removal.

5. Before cutting, the tank of the WEDM machine is filled with deionized water. After the tank is filled to the appropriate level, the strain gauge reading is set to zero.

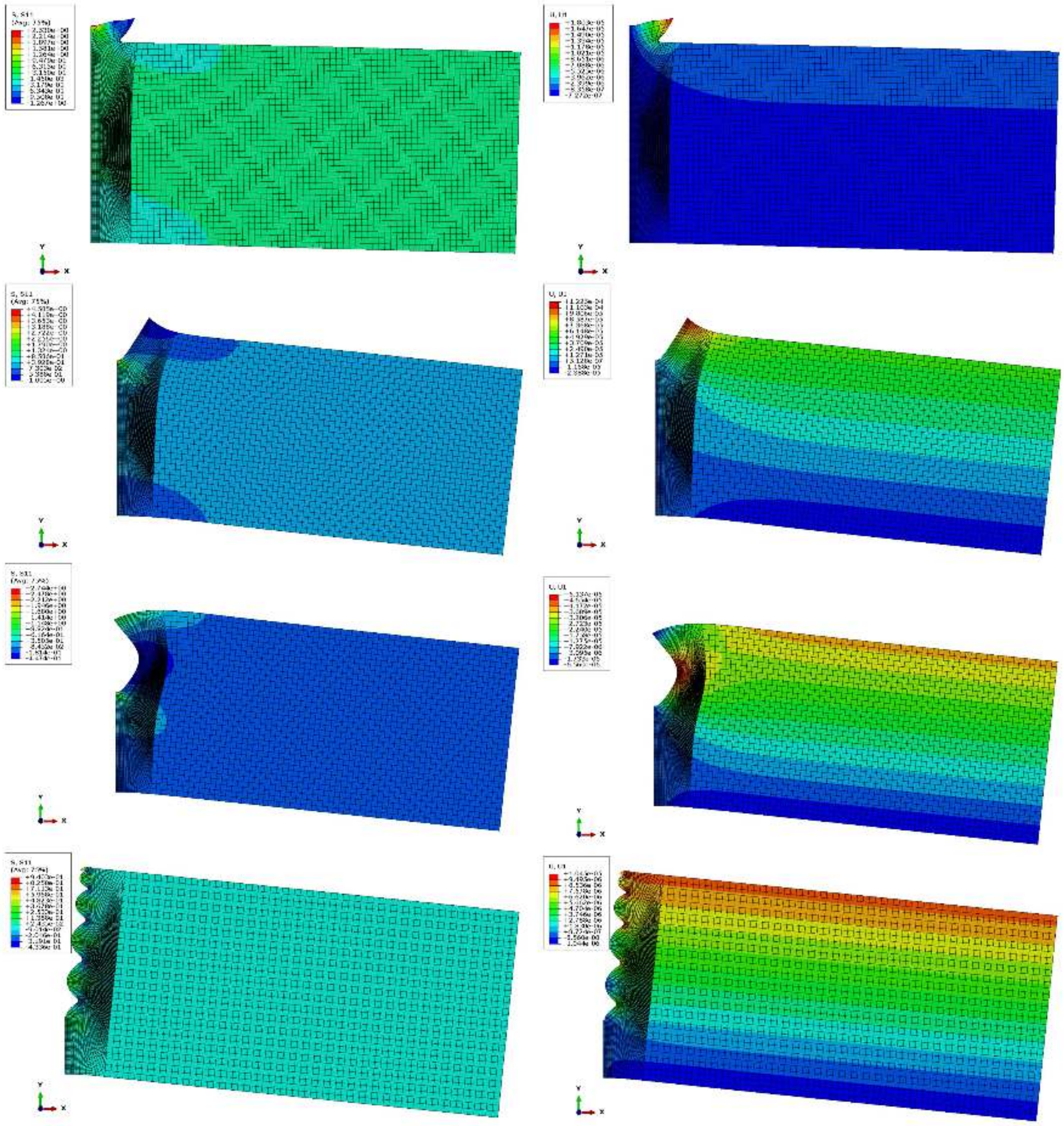

Figure 3.8: Simulation results showing the stresses and deflections corresponding to different load cases.

6. Incremental slot cutting is carried out according to pre-decided increments until 95-98% of the sample thickness has been cut. Cutting is stopped, and wire power is turned off after completion of each increment to get the strain reading corresponding to that particular depth level.

7. After completion of the slot cutting, the actual width of the slot and the re-

maining uncut thickness of the material are measured under a microscope to check for any differences from the pre-decided values. In case of any differences, necessary compensations may be made in the FEM model for compliance calculation.

3.4.2 Experimental setup

WEDM experiments were performed on the MAKINO U32j EDM machine as shown in Figure 3.9. Details of the equipment used for the slit cutting experiment are given in Table 3.2, whereas auxiliary materials used for installing strain gauges are listed in Table 3.3.

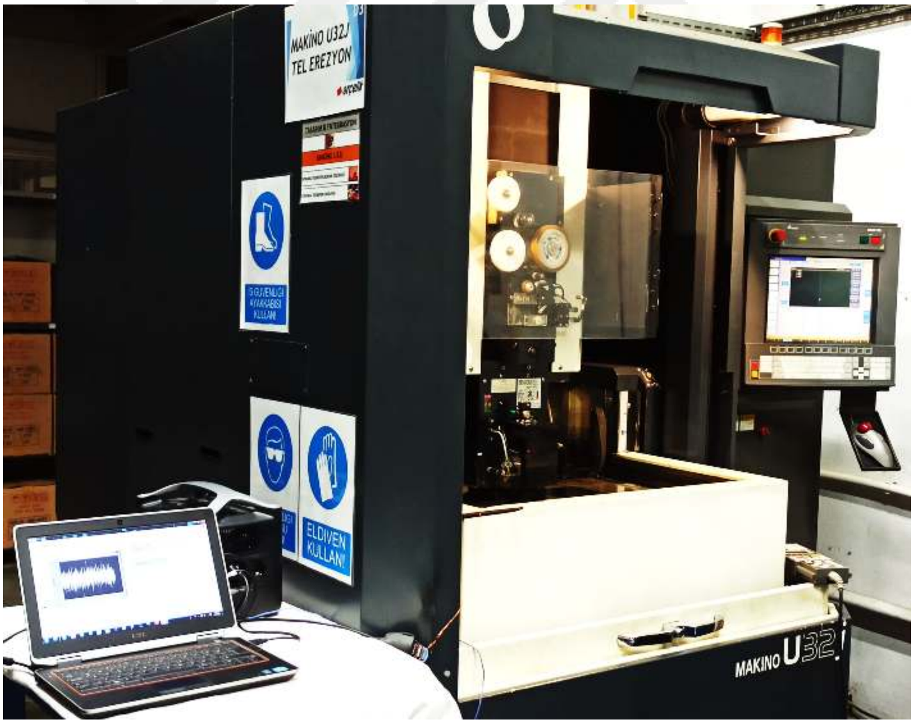

Figure 3.9: WEDM setup for slitting experiment.

Before carrying out the WEDM experiment, samples were prepared according to the required sizes, ensuring proper squaring and flatness of different sides. The strain gauges were then carefully installed on the samples. Proper alignment, bonding, and

Table 3.2: Equipment used for strain measurement during slitting experiment.

Sr.	Equipment	Model	Purpose
1.	Strain gauge	CEA-06-062UWA-350	Strain measurement
2.	DAQ	NI 9237	Strain gauge data acquisition
3.	Compact DAQ USB cable	NI 198506D-01	Connect DAQ to laptop
4.	RJ-50 to Screw-Terminal	NI 9949	For Wheatstone circuit
5.	RJ-50 to RJ-50 data cable	NI 194612C-02	Connect Screw terminal to DAQ

Table 3.3: Materials used for strain measurement during slitting experiment.

Sr.	Material	Type	Purpose
1.	Degreaser	-	Clean oil on surface
2.	M-Prep conditioner A	MCA-2	Fine clean the surface
3.	M-Prep Neutralizer 5A	MN5A-2	Fine clean the surface
4.	Adhesive	M-Bond 200	Bonding of strain gauge
5.	Inner coating	M-Coat A	Waterproofing
6.	Outer coating	RTV silicone	Waterproofing
7.	Miscellaneous: Sandpaper (fine), Adhesive band (transparent) for gauge installation, cotton gauze		

insulation of the strain gauges were ensured at this step, as shown in Figure 3.10. The sample was then held in the machine by clamping from only one side and leaving the other side free, thus ensuring the free formation of the crack. The clamping force was kept just enough to hold the sample without exerting any additional stresses due to clamping. At this stage, the alignment of the EDM wire was ensured such that it was parallel to the plane of the surface where the slit was to be carried out

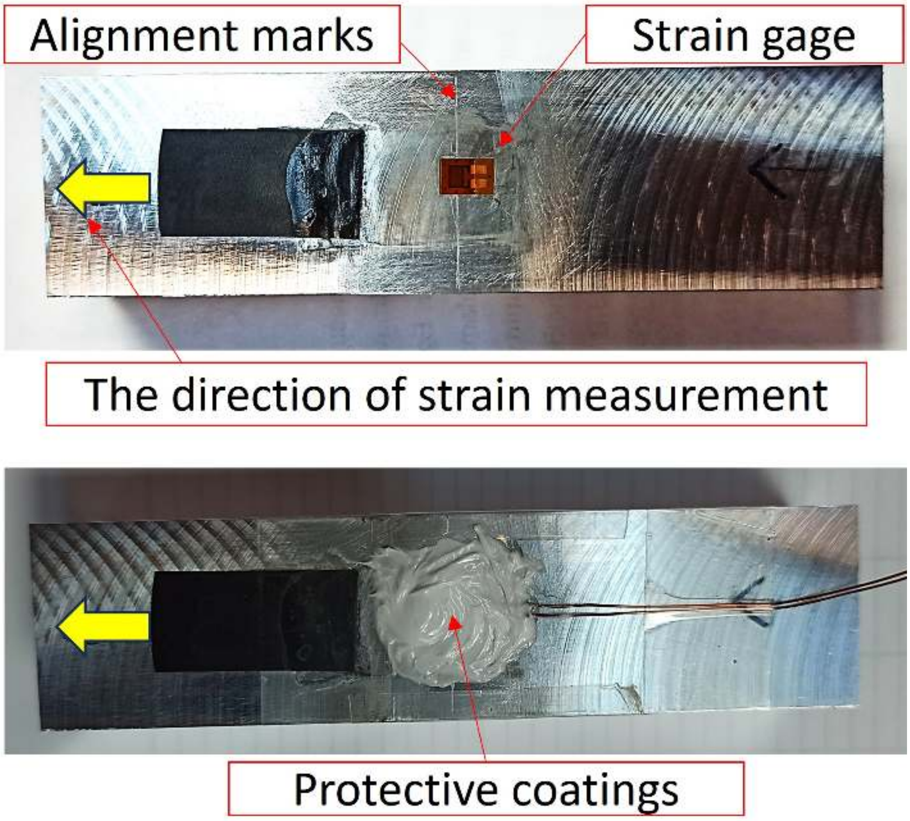

Figure 3.10: Installation of strain gauges.

and perpendicular to the direction of strain measurement. The process of slitting was carried out incrementally, and strains corresponding to each slit depth were recorded after stopping the cutting and turning off the power of the EDM wire. The clamping and incremental slit cutting of the sample are shown in Figure 3.11.

3.4.3 Precautions

The following considerations are critical for getting accurate results through the successful implementation of the crack compliance technique:

1. Preparation of samples:

   The samples for the measurement of residual stresses should be prepared carefully. The most important considerations to be taken care of while preparing

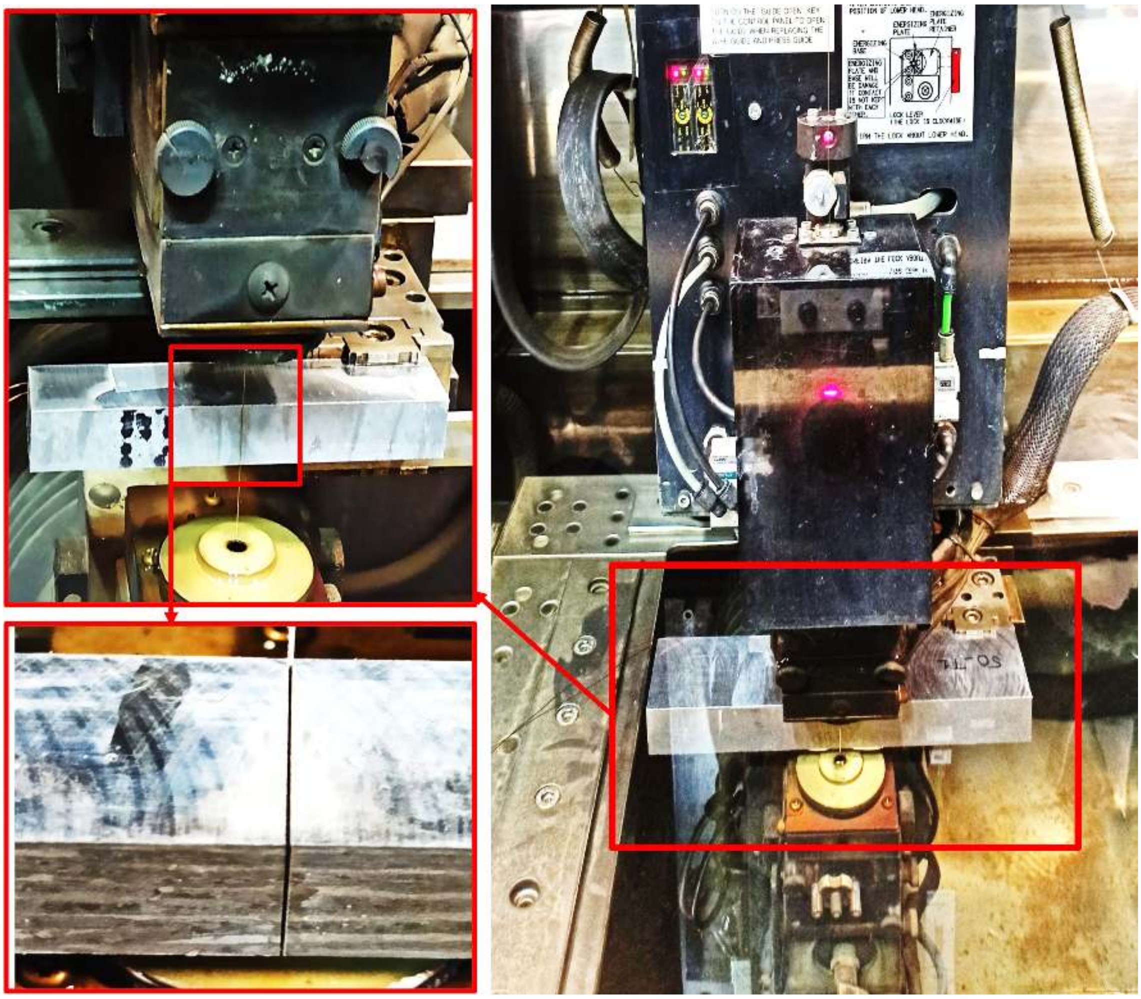

Figure 3.11: Slit cutting process.

the samples are their sizes and establishing the reference system for the correct alignment of the gauges. Since it is a plane strain problem, the width of the sample is less important; however, the length of the sample should be selected such that it should neither be so long to add the additional force at the slit/gauge location due to the overhung weight nor should it be so short that the stresses at the slit get affected by the clamps that are holding the samples at one of the ends. Generally, a length four times the thickness of the sample is considered good to avoid any size-related issues. Furthermore, the sample should be prepared so that its sides are squared to establish a reference system so that the strain gauges can be aligned correctly with respect to the direction of strain measurements, i.e., normal to the plane of the slit. Correct establishment of the reference system is also essential for aligning the EDM (electric discharge machining) wire before cutting the slit.

2. Application of strain gauge:
   The correct application of the strain gauges is crucial for the accuracy of results obtained from the slitting experiment. In this respect, it must be ensured that the gage is:
   - Properly aligned perpendicular to the slit, i.e., in the direction of the stresses to be measured.
   - Centered with respect to the slit such that half the gauge length should be at one side and the other half on the other side of the slit to be cut.
   - Bonded adequately to the sample, and proper insulation is carried out to avoid any electrical short-circuiting with the dielectric fluid.

3. Data acquisition setup:
   A data acquisition setup should be established to get the correct data for strain measurements corresponding to each cutting increment. The strain gauge is typically connected to a Wheatstone bridge circuit to get stable voltage readings corresponding to each slit depth. The voltage readings are then converted to the strain value using the formulations of the Wheatstone configuration.

4. Cutting:
   Before the EDM cutting process, proper alignment of cutting wire parallel to the surface to be cut and perpendicular to the strain gauge measurement direction is crucial. Any misalignment would result in errors in strain readings, and residual stress measurements would be affected. EDM process should be carried out slowly to limit the size of the resulting slit width. Furthermore, the program for the cutting process should ensure the stoppage of cutting at pre-decided depth levels for taking the strain gauge readings. Stoppage of the

process is also important to avoid any interference of the cutting currents with the strain gauge signals.

5. Post cutting measurements:
   After the slit-cutting process is complete, an inspection of the slit width and remaining thickness of the workpiece at the bottom of the slit should be examined under an optical microscope. In case of difference in the measured and the pre-decided values, necessary changes should be made in the FEM model to get the correct compliance matrices and polynomial coefficients according to the actual conditions.

3.4.4 Sources of errors

The crack compliance technique is relatively simple for measuring residual stress profiles inside the material. However, accurate determination of stresses requires the following care to be exercised during the process [35];

- The alignment of strain gauges must be ensured.
- The slot-cutting technique should be selected to generate no stresses due to the process.
- Clamping of the sample during slot cutting should not generate any additional stresses

3.5 Summary

The process of residual stress measurement using the crack compliance method is delineated. Various aspects of the technique, e.g., the theoretical background, FE modeling for calculation of compliance matrix, experiment procedure, and precautions to be followed to determine residual stresses accurately, are discussed. The results of the residual stress measurement are presented in the following chapter.

Chapter 4

HYBRID MODEL TO PREDICT DISTORTIONS IN MILLING

4.1 Overview

Distortion is a prevalent problem with large monolithic thin-walled machined parts. The aerospace industry is always concerned about this well-known problem. This chapter presents a hybrid analytical-FEM model for efficiently predicting the distortion of machined thin-walled parts. Milling loads are calibrated and applied at the surface of the meshed part model as moving mechanical and thermal load sources. The model duly incorporates the contributions of initial bulk residual stresses of the workpiece, heal flux, and cutting forces. Machining tests performed on aerospace alloy Al7050-T7451 to validate the model corroborated its strength for predicting part distortions.

4.2 Introduction

In the aerospace sector, distortion of monolithic machined parts is a significant problem. Therefore, it is essential to predict distortions in order to manage the quality of aeronautical parts. Post-machining deformations cost time and money, particularly in the case of large, thin-walled structural elements. The two primary factors that are known to contribute to these distortions are the initial bulk residual stresses (IBRS) and the cutting loads (due to machining forces and thermal phenomena). The workpiece material and the amount of material removed from the original blank often determine the contribution of each source. Initial bulk stresses are recognized to significantly affect the distortion of large thin-walled parts [38]. This is because of the fact about 90% of the initial workpiece material is removed in the milling of these parts, causing significant IBRS redistribution and part distortions. On the other hand, cutting loads due to machining may lead to plastic deformations. The prediction of these distortions is not a straightforward task. There are two main factors that complicate the deformation predictions for machined aerospace components. First of all, it is very difficult to represent complicated parts analytically. Second, utilizing 3D finite element modeling (FEM) to simulate deformation for large parts requires a lot of calculation and time. There have been several attempts to address these issues, but a wholesome approach to accurately predict these distortions is not available, and research remains in progress on effective prediction models.

A hybrid FEM model was given by Hussain and Lazoglu [67] to predict the deformation of a small thin-walled part. The effect of IBRS was not considered in the proposed model, which solely took into account deformation caused by cutting loads. The cutting loads, i.e., cutting heat flux and forces, were directly applied to the nodes of the meshed model corresponding to the finished part geometry. For peripheral milling, Denkena et al. [58] explored the impact of temperature and cutting pressures on form deviations of thin-walled objects. Brinksmeier and Solter [59] employed source stresses measured from a basic machined part for predicting the deviations in the form of complicated parts using FEM. Dreier et al. [107] proposed a FEM simulation-based technique for estimating the deformation driven by IBRS and MIRS. The technique was evaluated for the case of milling of a part of EN AW-7050 T7651 alloy. The FEM model was subjected to the MIRS, and IBRS determined using the diffraction (X-ray) technique. Analysis was done on the impact of various cutting strategies and locations of the part inside the workpiece blank. Similar methods were utilized by [108] to forecast distortion of Al7175-T7351 face-milled parts. For a simple Al7075-T6 T-shaped component, Schulze et al. [109] investigated the impact of IBRS and machining stresses using FEM. IBRS was discovered to be the primary cause of the part deformities. To examine the impact of IBRS profiles and MIRS on an Al7050 part, Jiang et al. [20] used three FEM programs. Huang et al. [12] too specified determined MIRS and IBRS profiles in the FEM model of the Al7050-T7451 part for distortion simulations. The IBRS was shown to be liable for 90% of the part deformations. To predict the deformation of frame components, Tang et al. [19] computed cutting loads by FEM and imposed them as nodal loads in a different FEM model. The aforementioned literature analysis demonstrates that the current methods for the prediction of component deformation need the prior determination of MIRS by employing FEM of the X-ray diffraction technique, both of these methods are highly laborious and resource intensive.

This chapter unveils a novel hybrid analytical-FEM model for predicting the distortion of milled thin-walled parts. Moving surface loads that have been analytically computed are imposed as heat flux and mechanical pressure in the FEM model of the part. By developing a simple experiment-based approach for fast calibration of surface loads, the uncertainty related to the direct application of cutting loads to the nodes is avoided. The impact of IBRS is effectively accounted for in the model. Al7050-T7451 aerospace alloy was used for experimental validation.

4.3 Modeling of initial bulk residual stresses and thermomechanical loads

4.3.1 Analytical modeling of the cutting loads

A typical end milling operation is illustrated in Figure 4.1. Analytical formulations for modeling end milling are derived according to [67, 102, 110]. The shearing and plowing cutting forces are calculated as follows:

$$\begin{pmatrix} dF_{tc} \\ dF_{rc} \\ dF_{ac} \end{pmatrix} = da_p \begin{pmatrix} K_{tc}h_c \\ K_{rc}h_c \\ K_{ac}h_c \end{pmatrix}; \quad h_c = f_z sin\theta \tag{4.1}$$

$$\begin{pmatrix} P_{cut} \\ P_{thr} \end{pmatrix} = a_p \begin{pmatrix} K_{te} \\ K_{re} \end{pmatrix} \tag{4.2}$$

where dF_{tc}, dF_{rc}, and dF_{ac} are the discretized values of the tangential cutting force, radial cutting force, and axial axial force. Whereas P_{cut} and P_{thr} are the plowing forces in the direction of the cutting velocity and thrust, respectively. The mechanistic calibration gave the cutting and edge coefficients K_{tc}, K_{rc}, K_{ac}, K_{te}, and K_{re}. h_c and d_{ap} are the uncut chip thickness and axial depth of cut discretized along the tool length, respectively. The values of both of these parameters depend on the current angle of immersion of the tool θ and the feed per tooth f_z. The thermal and

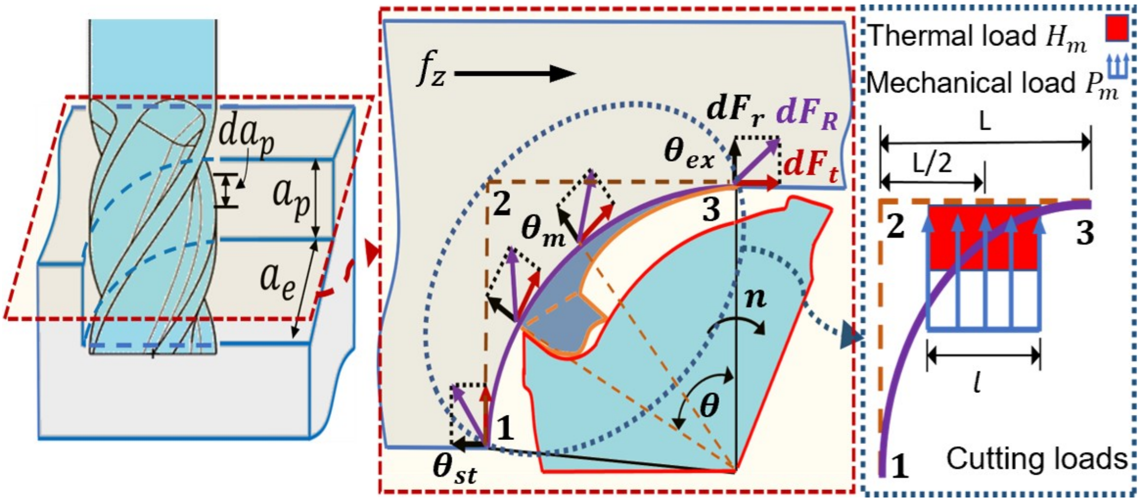

Figure 4.1: End milling process and schematic of cutting load sources.

mechanical loads due to shearing and plowing are determined as the surface heat flux and surface pressure as:

$$\dot{Q}_s(\theta) = F_s(\theta).V_s = \tau_s.\frac{a_p.h_c}{\sin\phi_n.\cos\phi_i}.\frac{V\cos\alpha_n}{\cos(\phi_n - \alpha_n)} \tag{4.3}$$

$$\dot{Q}_f(\theta) = F_u(\theta).V_c = \tau_s.\sqrt{F_{tc}(\theta)^2 + F_{rc}(\theta)^2}.\frac{V\sin\phi_n}{\cos(\phi_n - \alpha_n)} \tag{4.4}$$

$$F_R(\theta) = \sqrt{(F_{tc}(\theta) + P_{cut})^2 + (F_{rc}(\theta) + P_{thr})^2 + F_{ac}(\theta)^2} \tag{4.5}$$

$$\dot{Q}_{pl}(\theta) = P_{cut}.V \tag{4.6}$$

$$\dot{Q}_T(\theta) = h_s.[\dot{Q}_s(\theta) + \dot{Q}_f(\theta)] + h_p.[\dot{Q}_{pl}(\theta)] \tag{4.7}$$

$$H_m = \frac{mean[\dot{Q}_T(\theta_{st}) + \dot{Q}_T(\theta_m) + \dot{Q}_T(\theta_{ex})]}{l.a_p} \tag{4.8}$$

$$P_m = \frac{mean[F_R(\theta_{st}) + F_R(\theta_m) + F_R(\theta_{ex})]}{l.a_p} \tag{4.9}$$

where, the variables $\dot{Q}_s$, $\dot{Q}_f$, $\dot{Q}_pl$, $\dot{Q}_T$, P_m, H_m, and l denote the power of shearing, friction power, power of plowing, total power of cutting, mean value of surface pressure, mean value of surface heat flux, and width of the moving load source, respectively. The immersion angles of the tool at the start, middle, and exit are θ_{st}, θ_m, and θ_{ex}, respectively. ϕ_i, ϕ_n, α_n, τ_s, V, V_c, V_s, F_R, F_{ac}, F_{rc}, F_tc, F_u and F_s are the oblique shear angle, normal shear angle, normal rake angle, average shear flow stress, cutting velocity, chip velocity, shear velocity, resultant cutting force, axial cutting force, radial cutting force, tangential cutting force, rake face friction force, and the shear force, respectively. The ratio of shearing heat partition h_s is taken in accordance with [67] as 0.40, for plowing it is determined as [110]:

$$h_p = \frac{\sqrt{k_{wp}\rho_{wp}c_{wp}}}{\sqrt{k_{wp}\rho_{wp}c_{wp}} + \sqrt{k_t\rho_t c_t}} \tag{4.10}$$

where, ρ_{wp}, c_{wp}, k_{wp} are density, specific heat capacity and thermal conductivity of the workpiece while, ρ_t, c_t and k_t are the same physical characteristics of the tool.

4.3.2 calibration of thermal and mechanical load for the FEM model

Cutting loads, such as cutting forces and heat fluxes, may be quickly and accurately predicted using analytical models. The changing interaction of the workpiece and tool at different tool immersions makes it extremely difficult to apply these predicted loads to the FEM mesh. To overcome this difficulty, a method is used to apply calibrated mean heat flux and cutting pressure values as load sources moving on the machined surface. As illustrated in Figure 4.1, this rectangular moving source has a fixed height equal to the total axial depth of cut (a_p), whereas its width (l) is determined by calibration as a percentage of the length (L), which is the projection of the arc formed by the overall immersion of the tool on the freshly machined surface. In order to calibrate the loads, a small workpiece of a simple shape is milled using the same conditions as the finishing cut of the walls of the actual large part. The wall deflection and cutting temperature are measured at the designated points on the walls. Figure 4.2 ($a - b$) illustrates the setup of the load calibration experiment and the positions of the sensors for measurement. The FEM model of this trial workpiece is then established, and various fractions of the cutting heat flux (H_m) and pressure (P_m) as determined using Eqs. (4.8) and (4.9) are imposed as loads moving at the feedrate on the final wall surface. Figure 4.2(c) and Figure 4.2(d) show the imposed moving load and subsequent distribution of temperature on the wall, respectively. The experimental and simulated values of the wall deflection and cutting temperature at the measured positions are then compared. The load percentage and source width l combination that yields the correct values is chosen to be used in the FEM model of the big part actually required to be machined. Only a few minutes are required to carry out the simulation for each combination.

4.3.3 Measurement of initial bulk residual stresses (IBRS)

The crack compliance method (CCM) [111] was used to measure IBRS. In CCM, the stress profile is calculated using strains measured during the gradual cutting of a slit in the material. The incremental cutting of the slit was carried out by the WEDM process. An Al7050-T7451 plate of 50 mm plate was face machined to produce the 23

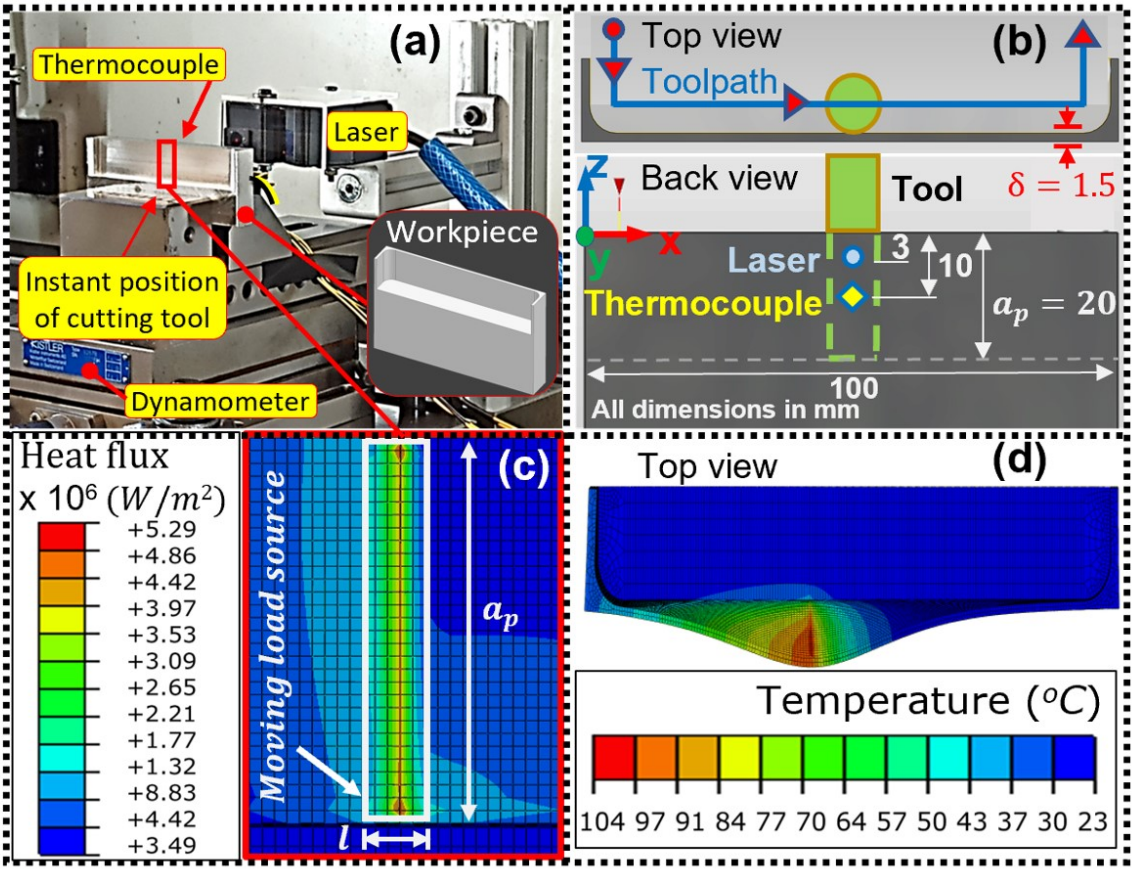

Figure 4.2: (a) Load calibration setup (b) Sensor layout in Back view and Toolpath in the top view (c) Front view shows the application of moving heat load in the FEM model (d) Resulting temperature and deflection in Top view.

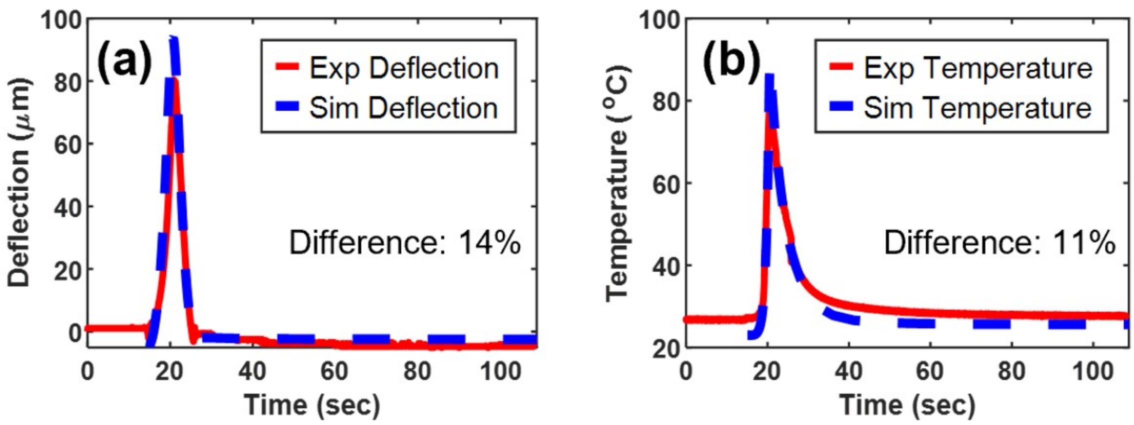

Figure 4.3: Comparison of experiments and simulations (a) deflection (b) temperature.

mm thick workpiece for the distortion experiment. The final 500 μm of the surface was removed under very mild machining settings to minimize machining-induced stresses. IBRS were measured for both the plate and the workpiece. Figure 4.4 demonstrates the setup of the WEDM procedure as well as the results of the IBRS measurements. As can be seen, the IBRS profile of the plate measured by CCM is similar to the residual stress profiles of the material available in the literature. This confirms that the crack compliance procedure was applied correctly. It can also be observed that the profiles of IBRS are different for the workpiece and the plate, indicating towards the redistribution of the IBRS due to the material removal. Therefore, it is essential to correctly identify each workpiece's stress status. The measured IBRS profiles of the workpiece were utilized to define the initial state of stress of the workpiece blank in the FEM model using fitted functions.

4.4 FEM modeling and simulations

The proper definition of the FEM model to consider all the conditions of the actual physical process is crucial for the accuracy of simulation results. Process constraints, IBRS, and end milling experiment cutting loads were correctly modeled using the Abaqus FEM program. The concurrent application of thermal and mechanical loads was taken into account using a fully coupled thermo-mechanical analysis. For defining the profile of IBRS in the blank and applying the computed cutting loads over time in a time series, subroutines were created in FORTRAN.

4.4.1 Modeling of the initial conditions of the workpiece

The initial condition for the workpiece mesh was the measured IBRS profile of the workpiece. In contrast to the in-plane stress values assumed to be uniform in the two planar directions, a polynomial fitting function defined the change in the stress in the blank's thickness. The IBRS profile defined in the transverse direction is depicted in Figure 4.5. The initial temperature for each node was set to 23°C, corresponding to the room temperature value, and the convection coefficient for the walls was set to 7 W/m^2K, corresponding to still air cooling. The clamping bolt regions and the area

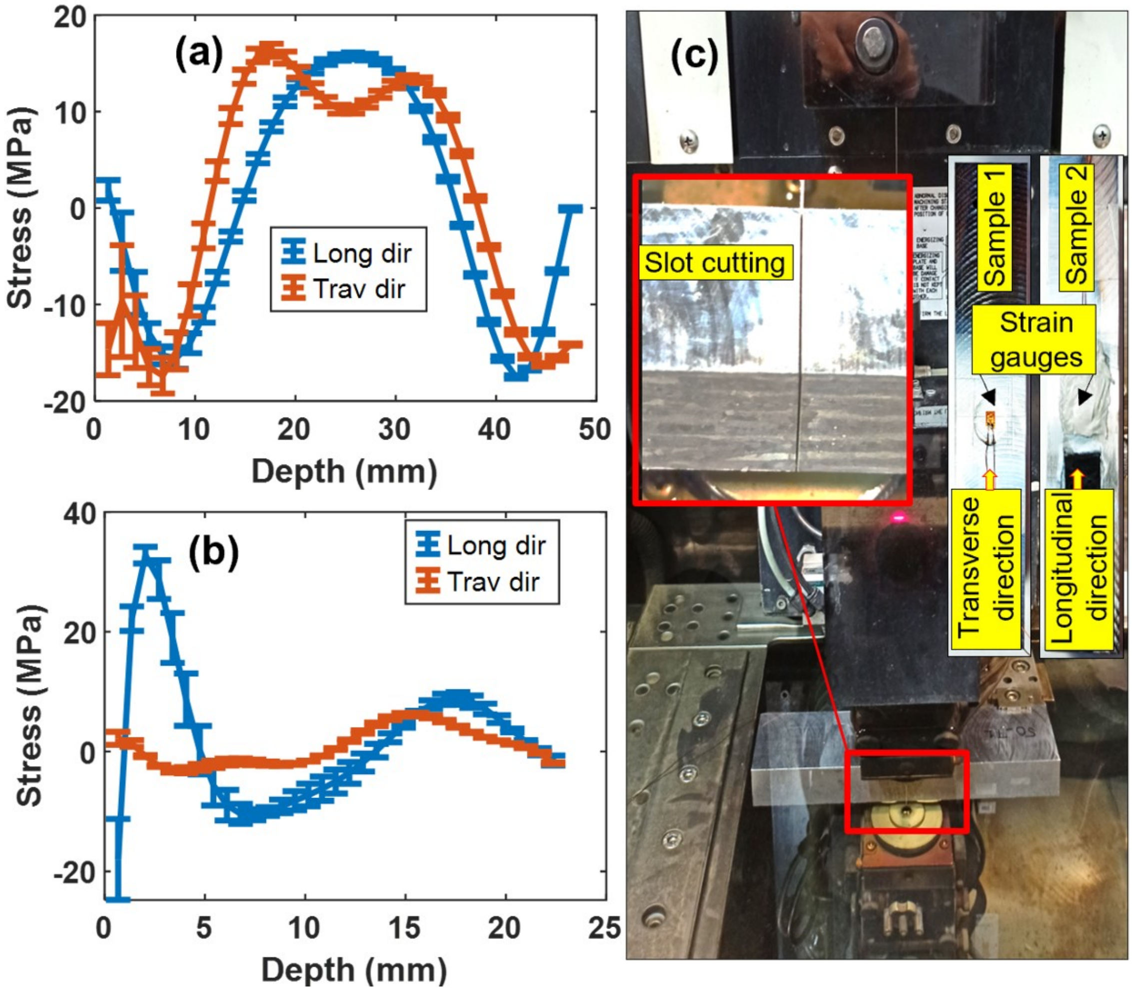

Figure 4.4: IBRS measurement setup and results for (a) stock plate 50 *mm* thick (b) machined workpiece blank 23 *mm* thick (c) Experimental setup for WEDM.

at the bottom of the component were defined as fixed boundary conditions. The true stress-strain curve as in [112] was used to characterize the material's elastic-plastic behavior. The physical characteristics were defined as provided in Table 4.1.

4.4.2 Modeling and simulation of cutting

As illustrated in Figure 4.6, moving calibrated surface loads were defined on the inner walls of the FEM model of the part having dimensions of 226 x 226 x 23 *mm*. The thicknesses of the floor and finished walls of the thin-walled part were 3 *mm* and 1.5 *mm*, respectively. The roughing operation carried out for machining

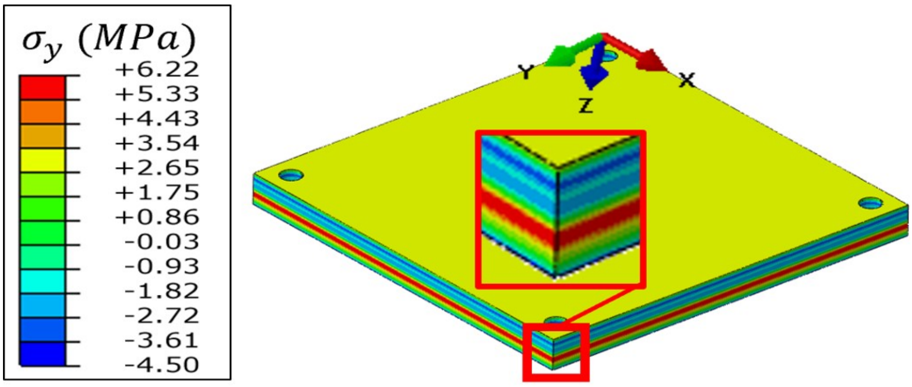

Figure 4.5: IBRS in the transverse direction defined in the FEM model.

Table 4.1: Physical characteristics of Al7050-T7451 and carbide tool.

Property	**Al7050-T7451**	**Carbide tool**
Density, ρ (Kg/m^3)	2830	13000
Thermal conductivity, k (W/mK)	157	62
Specific heat capacity, c (J/kgK)	860	234
Coefficient of thermal expansion, α $(1/K)$	25.4×10^{-6}	-
Modulus of elasticity, E (Gpa)	71.7	-
Poisson's ratio, v	0.33	-
Shear stress, τ_s (Mpa)	303.5	-

the inner pocket involved layer-by-layer removal of material, whereas finishing the inside surface of the walls was carried out in just one cutting pass. Figure 4.6 and Figure 4.7, show the tool paths for the finish and rough machining steps, respectively. The FEM model of the part had a mesh comprising 348,309 eight-node hexahedral elements with temperature and displacement degrees of freedom. As illustrated in Figure 4.6, the walls had fine mesh elements that were 0.5 mm in width and 1 mm in height. The bottom of the part had coarse mesh with elements that were 2 mm in size. To ensure that the moving cutting loads were applied effectively, the element size on the walls of the model was set to be smaller than the value of the width of the moving load source. Prior to applying surface load to the walls, material removal corresponding to the pocket machining was achieved by the element death approach. Layers of 2 mm depth corresponding to the actual machining process of each roughing pass were eliminated one by one up to the final depth of 20 mm. After removing each layer, the redistribution of residual stresses in the blank was realized by allowing an equilibrium step. The application of moving load sources on the walls simulated the last finishing step of the process. Steps related to the complete cooling of the workpiece and unclamping from the machine were also incorporated to mimic the actual process steps. To limit the rigid body motion of the component during the unclamping stage, 3-2-1 boundary conditions were defined as nodal constraints at three corners at the bottom of the part. A Xeon(R) CPU 3.7 GHz with 128 GB RAM took almost 300 min to do the distortion simulation for the large part.

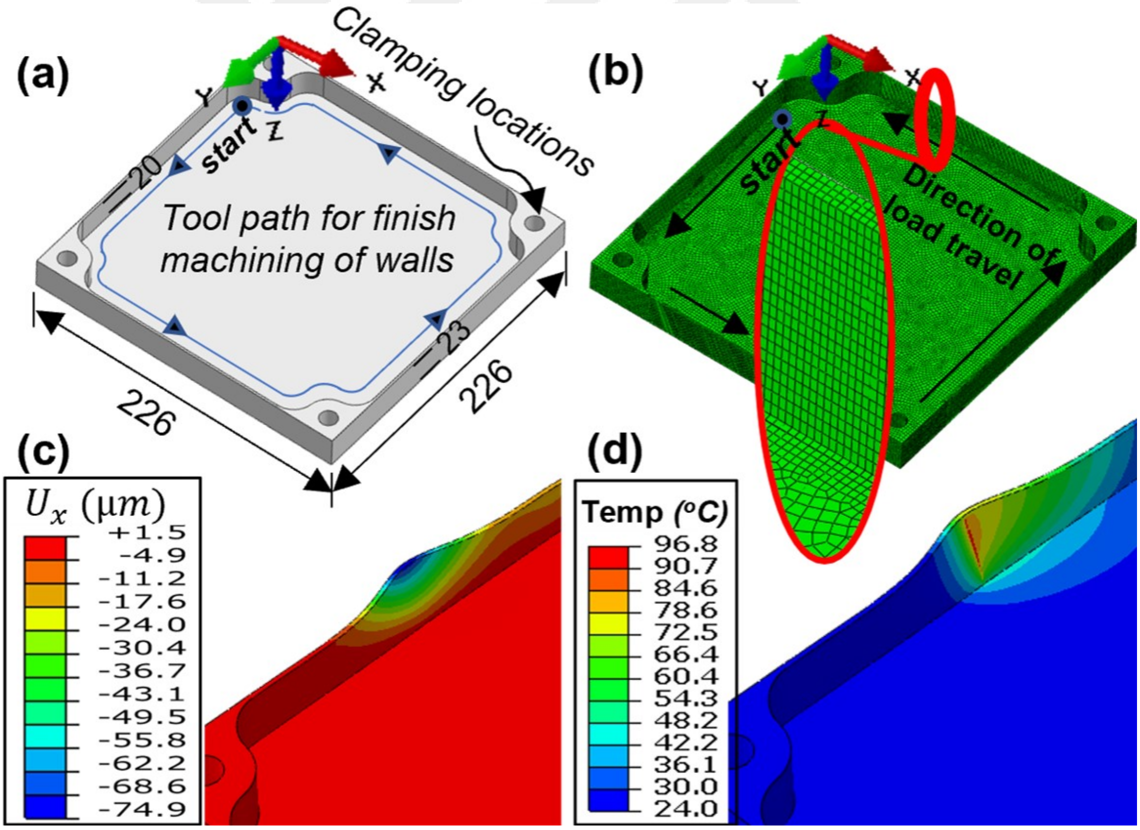

Figure 4.6: (a) Part CAD model (b) FEM model showing meshing (c) & (d) Temperature rise and wall deflection due to the application of moving cutting load.

4.5 Simulation results and experimental validation

The workpiece was meticulously prepared to ensure the flatness of its sides prior to the machining tests. Before the deformation experiment, many small finishing cuts were made to ensure the correct surface quality and prevent machining-induced stresses. The workpiece was prepared, and thermocouples were then mounted on the exterior of the walls, as seen in Figure 4.7. The workpiece was then secured to the machine's worktable, and laser sensors were placed to monitor deflections by targeting the exterior of the walls.

Figure 4.7: Thermocouple installation on the workpiece.

The thin-walled part of Al7050-T7451 was down-milled using a carbide tool under dry conditions on a Spinner 5-axis machine. The endmill with two cutting flutes had a diameter of 10 mm, a helix angle of 25°, and a rake angle of 13.6°, respectively. The axial depth of cut, feedrate, and cutting speed was 20mm, 480 mm/min, and 94 m/min, respectively. Figure 4.9 depicts the experimental setup. Four K-type thermocouples with 90 μm wire diameters were used to measure the cutting temperature. Two Keyence LK-H052 laser sensors and a Kistler 9123 dynamometer were used to detect the displacement of the walls during the milling process.

Finish machined part after machining is depicted in Figure 4.10.

Figure 4.11 compares observed and simulated values for the wall deflection and cut-

Figure 4.8: Workpiece clamping and installation of laser sensors.

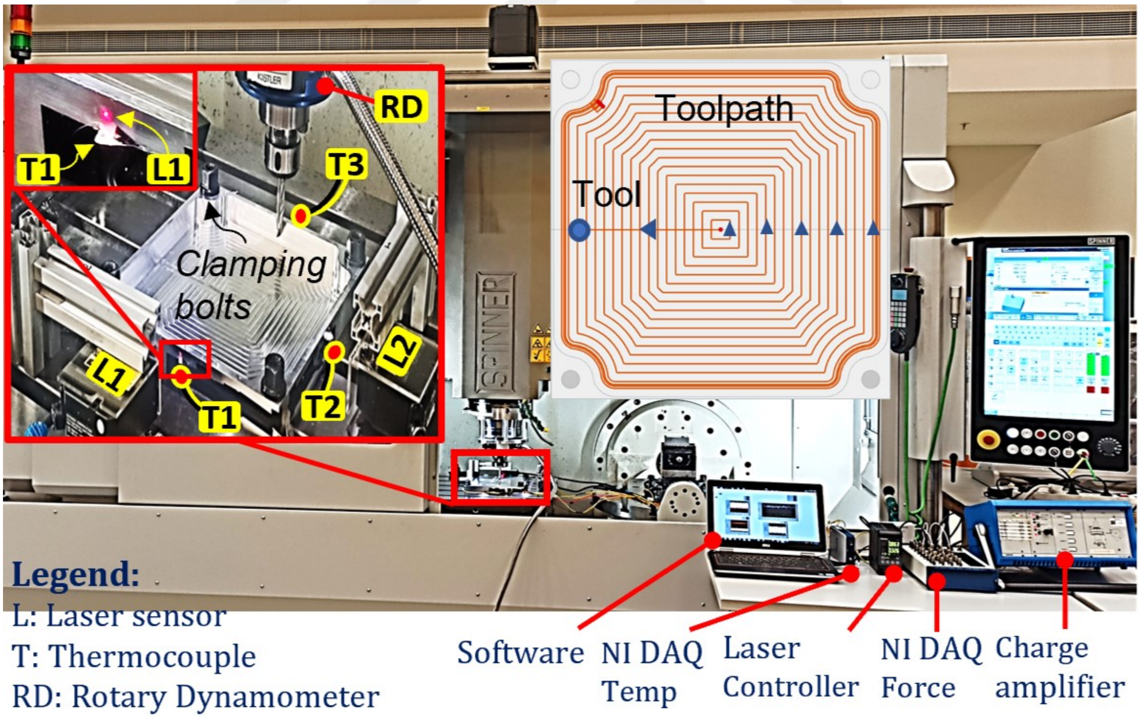

Figure 4.9: Setup for experimental validation.

ting temperature. The comparison justifies the calibration scheme for estimating cutting loads to be applied to the FEM model of the part. CMM measurements

Figure 4.10: Final machined part.

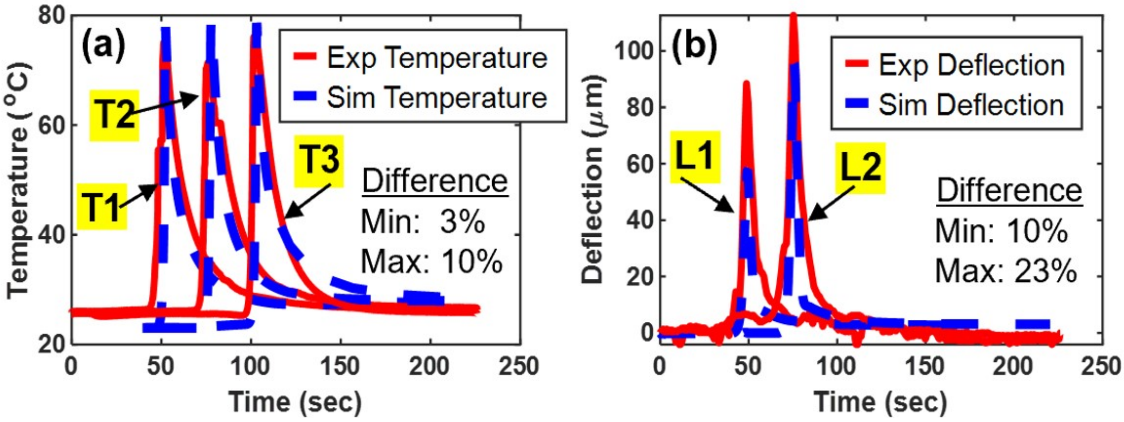

Figure 4.11: Comparison of simulations and experiments for the large part(a) temperature (b) deflection.

were carried out on the reverse side of the part before and after the machining operation to validate the results of distortion prediction. As illustrated in Figure 4.12, measurements were made at 49 places along a grid of rectangular shape, and the spacing between the grid points was kept at 36 mm. The difference in the surface profiles measured prior to machining and after the completion of the machining experiment was then used to calculate the deformation of the part as a result of the milling operation. The comparison between the estimated and actual values of the measured deformation is shown in Figure 4.13. The model could accurately estimate the deformation within 25% of the observed value.

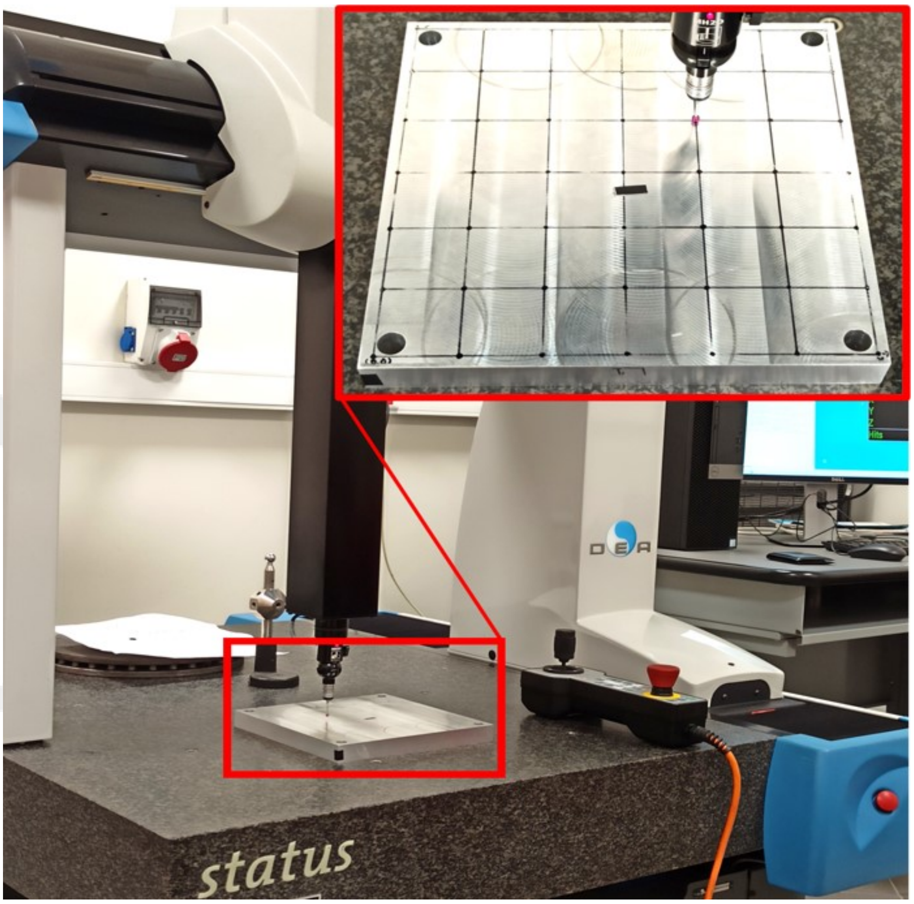

Figure 4.12: CMM measurement of part distortion.

4.6 Summary

A hybrid analytical-FEM model for fast prediction of distortions of milled thin-walled parts of large sizes is put forth in this chapter. A method is devised to precisely calibrate the cutting loads due to the machining process and apply them as moving loads on the surface of the mesh model of the part. The model successfully takes into account the material's initial bulk stresses. The outcomes of the validation trials confirmed the efficacy of the proposed approach in predicting the distortions of a large part. Keeping in view the simplicity of the proposed approach, it is

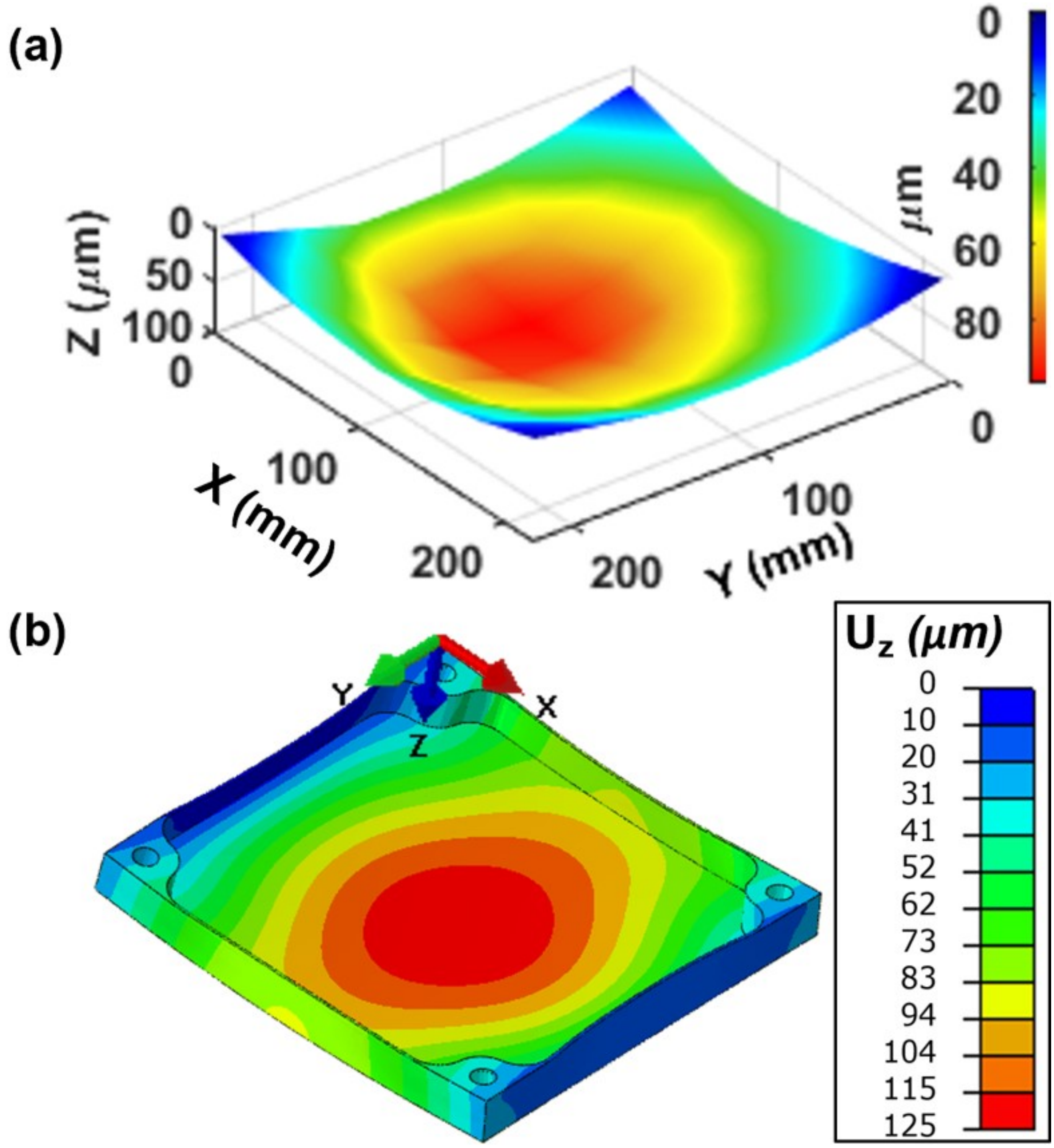

Figure 4.13: Distortion of the part (a) measured (b) simulated.

envisaged that it might further be extended to distortion simulations of the parts having complex shapes.

Chapter 5

MACHINING PROCESS MONITORING BY AN INFRARED SENSOR

5.1 Overview

Machining is crucial for manufacturing precision aerospace, automotive, and biomedical parts. Problems related to the machining process, i.e., tool wear, chatter, and workpiece deformation, have an impact on the quality of these machined components. Early detection of these issues is required to achieve the desired quality of precision parts. Traditionally, these process anomalies are monitored using commercial sensors like lasers, dynamometers, accelerometers, etc. This chapter presents monitoring of the machining process based on a low-cost infrared sensor. Compared to state-of-the-art sensors, which are engineered to monitor specific attributes of the machining process, the employed sensor can monitor multiple aspects. To determine tool wear, chatter, and workpiece deflection, infrared sensor data is processed in the time and frequency domain. Validation of the results is accomplished by using commercial sensors through established methods. Results of validation experiments corroborate the strength of the proposed approach in estimating the tool wear, chatter, and workpiece deformation.

5.2 Introduction

The evolution of Industry 4.0 has enabled a paradigm shift from traditional manufacturing to intelligent manufacturing. Smart and intelligent machines equipped with sensors boast the potential to analyze and control the machining process. With the integration of artificial intelligence (AI) technology, these machines aim to optimize the machining process in real-time, which would significantly boost productivity by minimizing part rejections [113]. Such systems are still in the evolution phase and are far from being adopted on the industrial scale. Meanwhile, in-situ monitoring of the process using commercial sensors provides significant opportunities for analysis and optimization of the machining process. The most important process-related issues that lead to inferior quality and, hence, the rejection of precision machined parts are tool wear, chatter, and workpiece deformation. Timely assessment of these issues allows adjustment of the machining process and avoids part nonconformances. There is continuous research towards finding the most suitable sensors and methods for efficiently monitoring these issues in the industrial environment. Both direct and indirect measurements using sensors such as acoustic, ultrasonic, capacitive, optical, current, piezoelectric, and strain gauges can be found in the literature. The following paragraphs summarize significant developments in monitoring each of these process attributes.

5.2.1 Tool wear detection

Machining is a thermomechanically intensive process for the workpiece and cutting tool [110]. Very high cutting loads generated during the process cause wear of the cutting tool by several mechanisms; details of these mechanisms can be found in [114]. Cutting tool wear affects the surface finish of the workpiece. It may also lead to sudden tool breakage, causing catastrophic damage to the workpiece or the machine. Timely identification of wear of the cutting tool is thus very crucial for achieving the required quality and efficiency in machining. In literature, two approaches are generally adopted for monitoring tool wear, which are direct and indirect measurements [115]. In the direct measurement approach, cutting tool wear or breakage is measured with the help of optical systems such as cameras or laser beams. Hou et al. in [116] presented an online vision-based system to monitor the tool condition in dry cutting by implementing the self-matching algorithm, and the maximum absolute flank edge was reported as 0.030 mm. These optical techniques offer reasonable measurement accuracy; however, environmental factors such as illumination and cutting fluid in the machine limit their usage during machining.

On the other hand, indirect methods estimate tool wear based on the information obtained from the sensors employed in the vicinity of the machining process, i.e., on or near the tool/workpiece. The sensors that are commonly used for these methods measure acoustic, force, acceleration, or current signals. Since these sensors do not directly measure the worn surface of the tool, the accuracy of their measurement requires rigorous scrutiny. Li et al. [117] presented a signal processing technique using audio signals and developed a machine learning-based predictive model to classify tool wear. Salgado and Alonso [118] illustrated a method based on the signals of sound and feed motor for tool condition monitoring in turning operations. Huang et al. [119] demonstrated that the change in the magnitude of acoustic emission (AE) signals during the machining operation was associated with the change in wear levels of the cutting tool. An ensemble convolutional neural network model was introduced in [120] that employs audio sensors for tool wear monitoring to predict tool wear values accurately under different cutting conditions. Zhou et al. [121] proposed a method for measuring tool wear using the signals obtained from acoustic sensors. The dominant feature identification algorithm was used to select the most usable feature for prediction. All these studies demonstrated the reliability of AE for predicting tool wear in a lab environment; the background factory noise severely limits its application in the industrial environment. Other than AE signals, many studies can be found using vibration signals acquired using accelerometers to estimate tool wear. Rmili et al. [122] detected cutting tool life based on the mean power of the vibration signal acquired using the accelerometer. The decision about tool wear was made based on a pre-defined threshold value.

Similarly, Twardowski et al. [123] predicted tool wear in milling by applying machine learning to the accelerometer data and reported a classification of tool wear with a 0.8% error. Kalvoda and Hwang [124] utilized the Hilbert Huang transform (HHT) on the accelerometer signals to detect tool wear. Dheeraj and Deivanathan [125] also demonstrated the feasibility of early tool wear detection using accelerometer data and reported an accuracy of 79.56% using the K-star classifier. Other than single sensor-based detection, some studies [126, 127] have also reported an increase in the accuracy of wear estimations by using the sensor fusion technique. Bagga et al. [128] implemented Neural networks to detect tool wear by the fusion of the vibration, temperature, and force signals during the machining operation. Huang and Lee [129] also studied the effect of combining different sensors using sensor fusion to identify tool wear.

5.2.2 Chatter detection

Chatter or regenerative chatter is self-excited vibration triggered by the difference in chip thickness resulting from the phase shift in vibration patterns of the previous and subsequent cutting pass. Chatter results in poor surface finish of the machined part, accelerated tool wear, and even cutting tool breakage. Several studies aim to identify and mitigate chatter using data-driven or physics-based approaches. Wang et al. [130] reviewed the state of the art on chatter detection methods and highlighted the limitations of offline chatter detection. The complexity of obtaining modal parameters due to varying dynamics of the workpieces, the uncertainty of chatter occurrence at the conditions determined in offline tests, and errors due to simplification of dynamics of the complex multi-degree of freedom system were mentioned to be the major factors limiting the accuracy of offline chatter calculations. Due to these limitations related to offline methods, the significance of the development of sensors for data-driven chatter detection was highlighted. Acceleration, force, and sound signals were reported to be the most commonly used signals for data-based chatter detection methods. In contrast, current, image, and displacement signals were reported to be less commonly employed. Kim et al. [131] developed an optical curved edge sensor (CES) and implemented it on an aerostatic spindle. Shi et al. [132] presented a method for online chatter detection based on piezo actuators. The method was reported to be able to detect the transition between no chatter and chatter states. The proposed piezo actuators were application-specific and needed special care for positioning and installations on the workpiece. Zhang et al. [133] used force signals acquired using a dynamometer and applied signal processing techniques, variational mode decomposition (VMD), and wavelet packet decomposition

(WPD) to identify chatter. The variation in energy entropy of the signals was shown to be related to the stable or chatter state of the process. Navarro Devia et al. [134] reviewed different sensors, signal processing techniques, and machine learning methods for detecting chatter. The usage of accelerometers, force sensors, microphones, acoustic sensors, and current signals for data-driven chatter detection was reported. Wu et al. [135] also reviewed chatter detection and suppression techniques in machining thin-walled parts. The need for the development of low-cost sensors for reliable, fast, and precise detection of chatter was highlighted. Yesilli et al. [136] used transfer learning for autonomous chatter detection in the turning and milling process. Accelerometers and capacitive probes were used to collect data for detecting chatter in the turning and milling process, respectively. Riviere et al. [137] detected chatter in the milling process based on the amplitude level, variance, and frequency content of microphone signals. Detection of frequencies different than spindle speed or tooth passing frequency was used as the criterion for chatter detection in milling. Tran et al. [138] employed multi-sensor data fusion on data collected from a microphone and accelerometer to detect chatter in the milling process. Rahimi et al. [139] used a microphone and accelerometer for hybrid machine learning and physical model-based chatter detection.

5.2.3 Workpiece deformation

Measurement and control of workpiece deformation are crucial for precision applications, e.g., thin-walled components of the aerospace industry [140]. Traditionally, these measurements are conducted in an offline manner after completion of the machining process. Measurements of finished parts, however, limit the opportunity to avoid non-conformities. On the other hand, online measurement of deformations during machining allows adjusting the process between different cutting passes to avoid excessive deformations. There has been a rising trend towards online measurement and compensation of errors for machined parts. Ge et al. [135] emphasized the importance of on-machine measurement of part deformation in the context of online error compensation and presented an integrated approach for error compensation.

A machine probe was employed for on-machine measurement of part deformations. Li et al. [141] also used a machine probe for on-machine measurement of the workpiece deformation. Song et al. [42] used a portable joint measuring machine to validate the results of deformation simulations of a low-stiffness part. Ratchev et al. [23] targeted inductive sensors on the back of the machined surface for online measurement of the defection of a thin-walled part. The measurement of deflection value was found to be affected by the vibration of the workpiece during the machining process. Loehe et al. [142] proposed an in-process measurement method for the deformation of thin-walled workpieces using a non-contact optical laser doppler vibrometer. Lazoglu and Mamedov [143] used the Keyence LK-030 laser sensor for online measurement of the deflection of a thin-walled part in micro-milling. Akhtar et al. [38] carried out a review of the literature on the prediction and control of deformations of aerospace parts and reported linear displacement sensors, on-machine measuring probes, and CMM as the most employed sensors for deformations measurements. In a review, Wu et al. [135] discussed the potential of different online deflection monitoring/measurement and error compensation techniques. The challenge of employment of costly sensors, e.g., touch probes and laser displacement sensors for online monitoring of the deflection of thin-walled parts, was highlighted. The above literature review shows that several studies have been conducted on detecting tool wear, chatter, and workpiece deformation during the machining process. Most of the studies employed commercially available sensors like dynamometers, laser displacement sensors, accelerometers, etc., which are expensive to use in the factory environment. None of these sensors or the low-cost sensors such as microphones, eddy current sensors, and strain gauges was found to be suitable for detecting multiple process attributes. This study presents monitoring and analysis of the machining process using a low-cost infrared (IR) based sensor. Infrared sensors are widely accepted in the fields of robotics and biomedical for proximity measurements and smart health monitoring, respectively. In machining applications, IR sensors are primarily found in thermal measurement systems. In contrast, its potential for monitoring other aspects of the machining process, such as tool, wear chatter, and workpiece deformation, is yet to be explored. This study demonstrates using the IR sensor to estimate all these aspects using a single sensor. The non-contact nature of the IR sensor is considered an advantageous feature that avoids the issues associated with contact-based technologies, i.e., dynamometers, accelerometers, strain gauges, etc. The sensor data is acquired through a data acquisition setup and is analyzed in time and frequency domains. The strategies to extract data features for detecting or measuring the different process attributes are elaborated.

5.3 Methodology

The infrared sensor is comprised of an LED (transmitter) and a phototransistor (receiver) pair, as shown in Figure 5.1. The transmitter emits infrared rays (940 nm) that strike the target surface, reflect, and are collected by the phototransistor. The sensor's output varies with the intensity of the reflected rays received by the phototransistor, which is proportional to the change in the displacement of the target object. IR sensors in the 2-1000 mm range are typically used to measure displacement. In this study, an infrared sensor QRE1113 (Fairchild Semiconductor International Inc., San Jose, CA, USA) is employed that has a measuring range of 5 mm. In the proposed method, the machining process attributes are monitored by measuring the output voltage of the IR sensor. Compared to the expensive single-purpose commercial sensors, the proposed sensor is a low-cost solution to multipurpose machining process monitoring, i.e., tool wear, chatter, and part deflection.

5.3.1 Experimental setup and data acquisition

CNC machining center Spinner U1530 was used to set up different experimental configurations for each task, as shown in Figure 5.2. To detect chatter and measure wall deflection, the workpiece was held in a vice mounted on the machine bed while the infrared (IR) sensor targeted the back side of the machined wall of the workpiece. On the other hand, tool wear detection was carried out by scanning the rotating end mill directly by the sensor. The data were collected at a sampling rate of 20

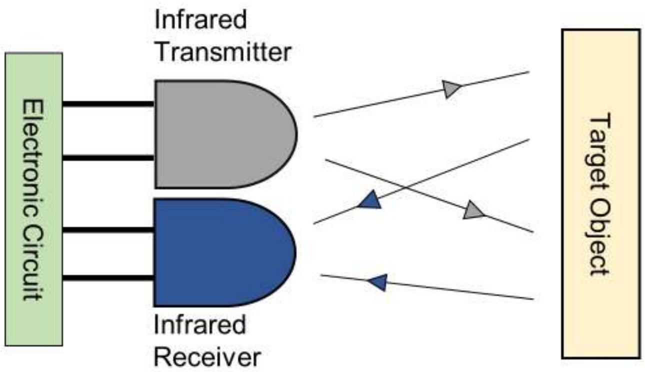

Figure 5.1: Working principle of infrared sensor.

kHz using NI 6259 data acquisition unit. Additionally, a Keyence laser sensor (LK-H052) and a 3-axis accelerometer were used to acquire data to validate the IR sensor measurements.

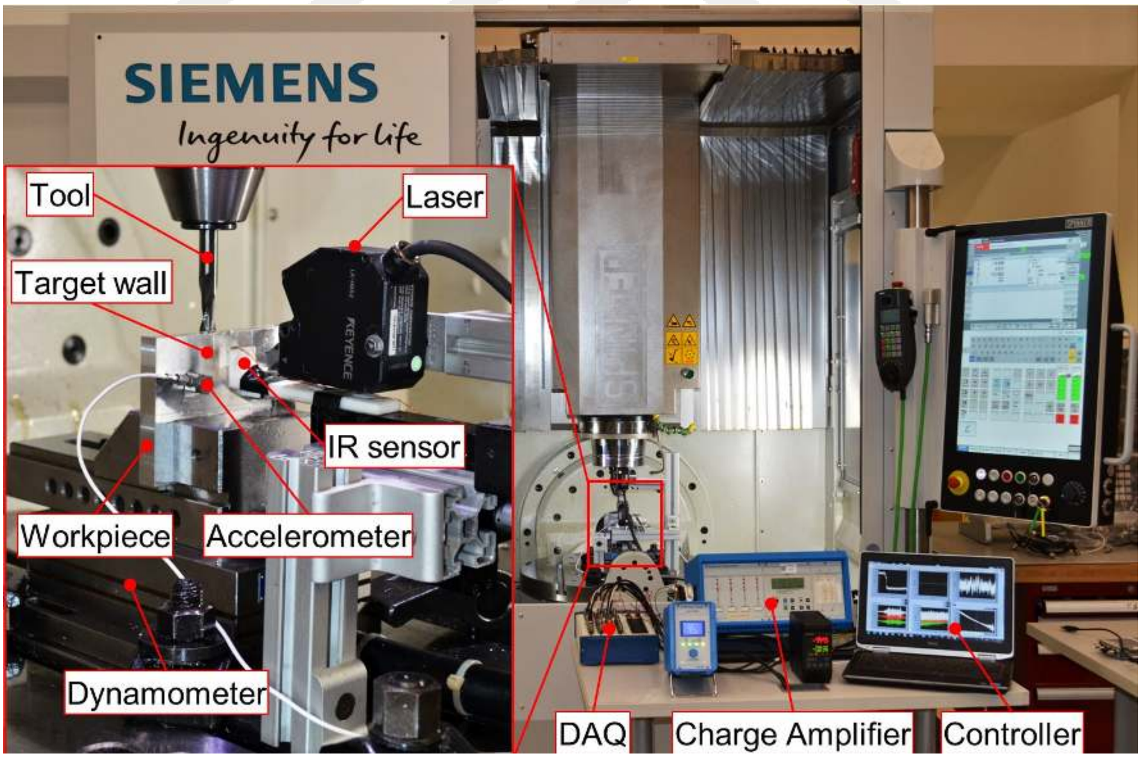

Figure 5.2: Experimental setup and data acquisition system.

5.3.2 Data processing

The IR sensor data is analyzed in time and frequency domains to detect or measure different aspects of the machining process. The acquired data is then processed using signal processing techniques such as filtering, fast Fourier transform (FFT), peak-to-peak analysis, and fundamental frequency removal. An overview of the overall methodology is given in Figure 5.3. Details of the various data features used for detecting or measuring various process aspects are elaborated in the subsequent sections.

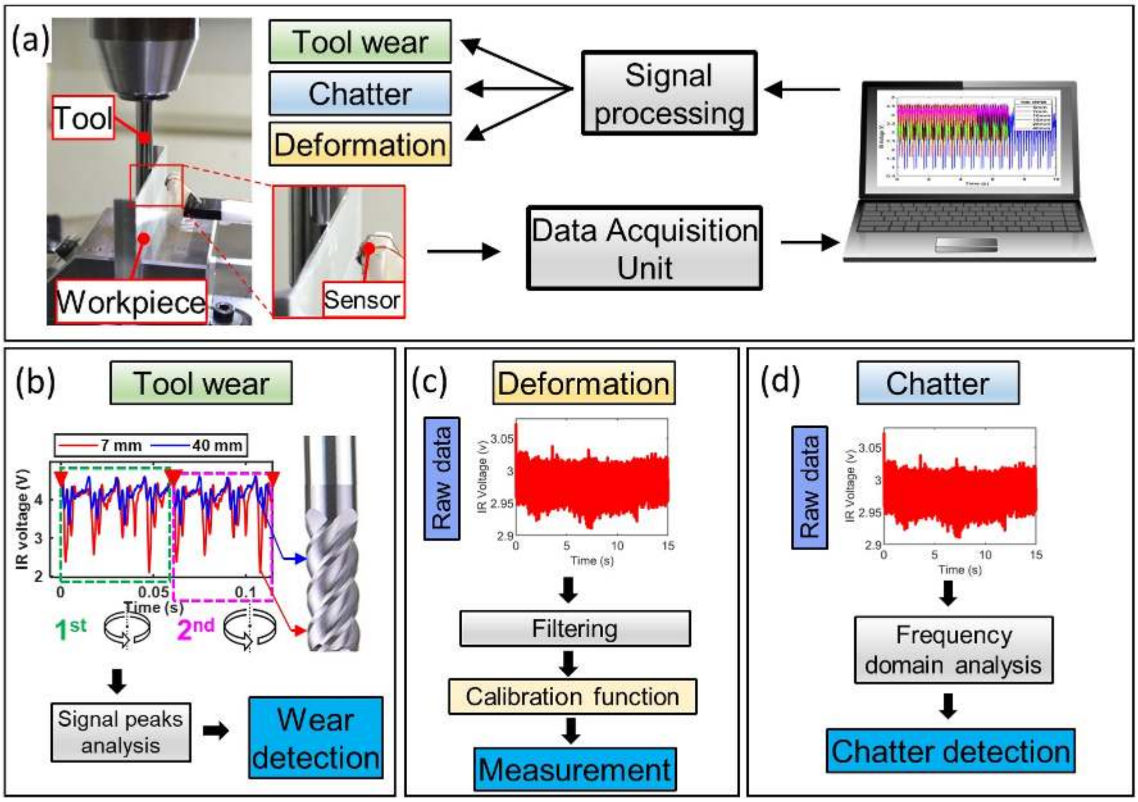

Figure 5.3: Overview of the data acquisition and signal processing system. (a) Overall system (b) Tool wear detection (c) Deflection measurement (d) Chatter detection.

Detection of tool wear

The experimental setup used for tool wear measurement is shown in Figure 5.4. It consists of the infrared sensor targeting directly at the end mill from a pre-set distance and at a specified axial depth of cut a_p. The IR sensor voltage data is acquired at a sampling frequency of 10 kHz while the end mill is rotated in the spindle at a certain revolution per minute (rpm) for a specified period. The change in wear levels of the tool translates into the change in output voltage because of the variation in the distance between the sensor and the tool surface. The tool wear is estimated using these signals by visualizing and processing the data in the time and frequency domain.

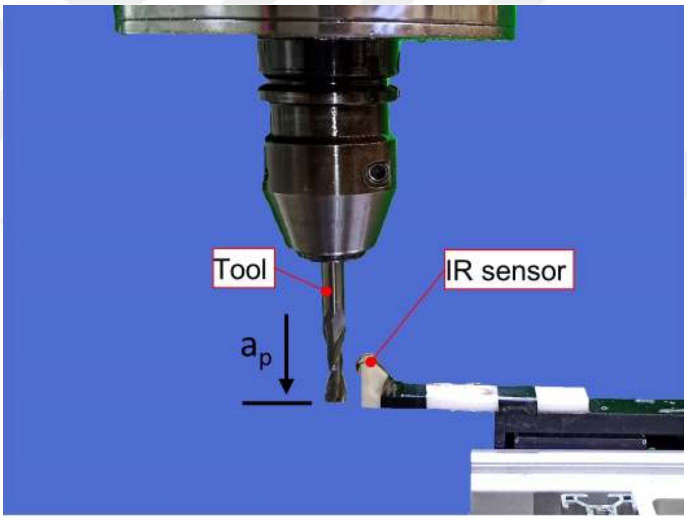

Figure 5.4: Tool wear detection hardware setup consisting of an IR sensor and endmill tool.

Time domain analysis

The overview of the signal processing scheme in the time domain adopted for the tool wear is presented in Figure 5.5. First, the raw data of the tool profile, as shown in Figure 5.5(a) is acquired by scanning the tool with the IR sensor. The acquired data is fragmented into frames corresponding to each tool revolution based on the repetition of peaks corresponding to the different cutting flutes after each revolution. The ensemble averaging method was utilized to check the repetition of the cutting tool profile after each revolution, as shown in Figure 5.5(b). The peaks corresponding to different a_p values for a single revolution are then compared with those of the reference data. In this study, data acquired at $a_p = 40\ mm$ was taken as reference data since the depth of cut used in the machining experiment was less than this value, and the cutting edges of the tool were unworn at that depth. The peaks corresponding to the more worn cutting edges were found to be higher than those for the less worn cutting edges. The comparison of data peaks acquired at $a_p = 5$ and 40 mm is illustrated in Figure 5.5(c). Furthermore, data peaks corresponding to these a_p values were plotted after normalization with respect to reference data for better representation of wear as shown in Figure 5.5(d).

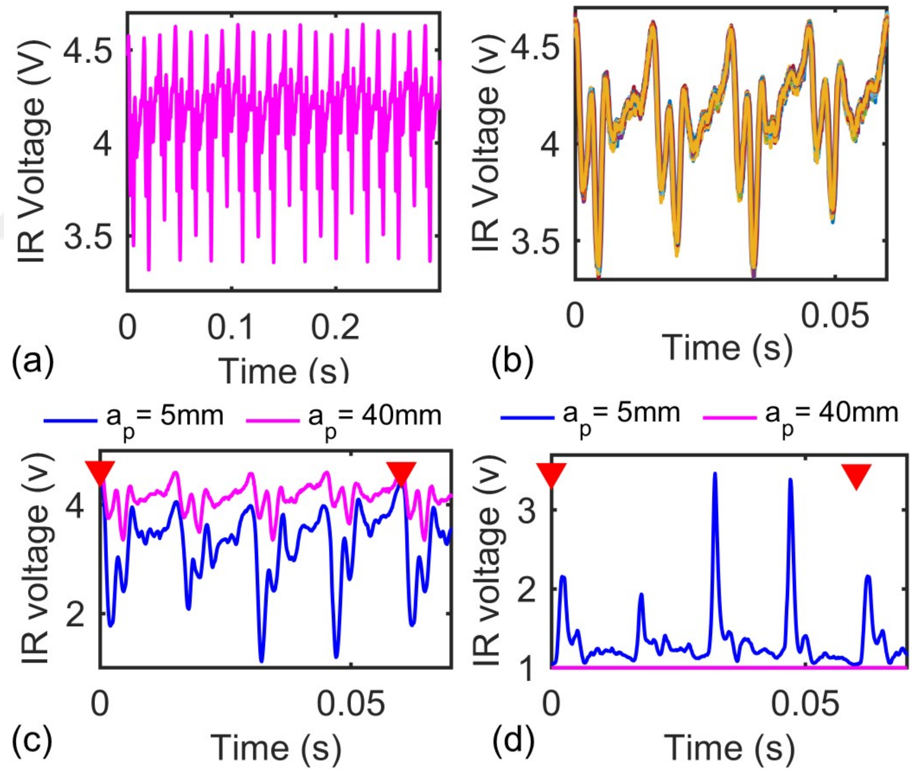

Figure 5.5: (a) Raw data of the tool wear scan with IR sensor (b) ensemble average (c) peak-to-peak analysis (d) Data normalized w.r.t no wear condition.

Frequency domain analysis

The frequency domain analysis takes the fast Fourier transform (FFT) of the data acquired. The power of the frequencies corresponding to tooth passing frequency at different a_p values is then compared. It is noticed that the power of the frequencies for more worn regions is higher as compared to less worn regions. It can be seen in Figure 5.6 that the power of the frequencies corresponding to the more worn region at a_p (5 mm) is higher than the less worn region at a_p (40 mm).

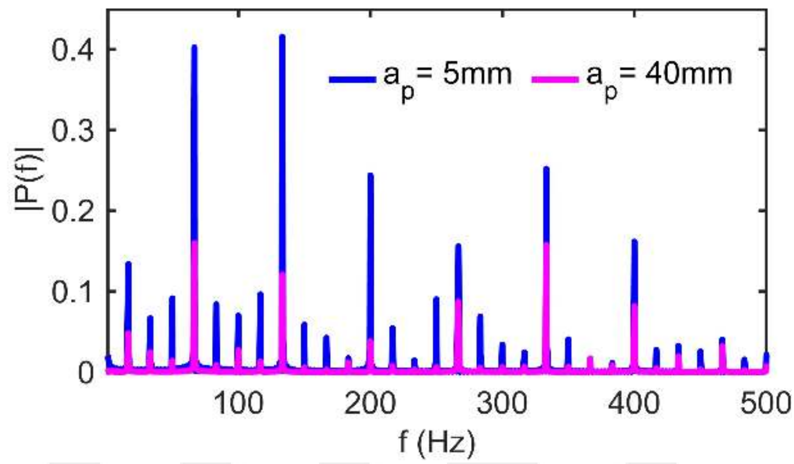

Figure 5.6: FFT of the data at a_p values of 5 mm and 40 mm.

Chatter detection

The hardware setup for chatter detection is shown in Figure 5.7. The workpiece is clamped in a machine vice, and the IR sensor is positioned to target the back surface of the wall being machined. A laser sensor is also installed in the proximity of the IR sensor for obtaining displacement data, whereas workpiece vibration data was acquired using a 3-axis accelerometer installed on the workpiece. Additionally, a microphone with a bandwidth of 24 kHz was placed inside the machine near the workpiece to collect the sound signals. Chatter detection is carried out in the frequency domain by processing the IR sensor data acquired during the machining of the workpiece. End milling experiments are performed on Al 7050-T451 workpiece using a diameter of 10 mm, two fluted carbide endmill. The spindle speed for different experiments varied between 1500 to 12000 rpm, whereas the axial depth of cut a_p and feedrate f_z are kept the same at 20 mm and 480 mm/min, respectively. A general overview of the signal processing approach adopted for chatter detection

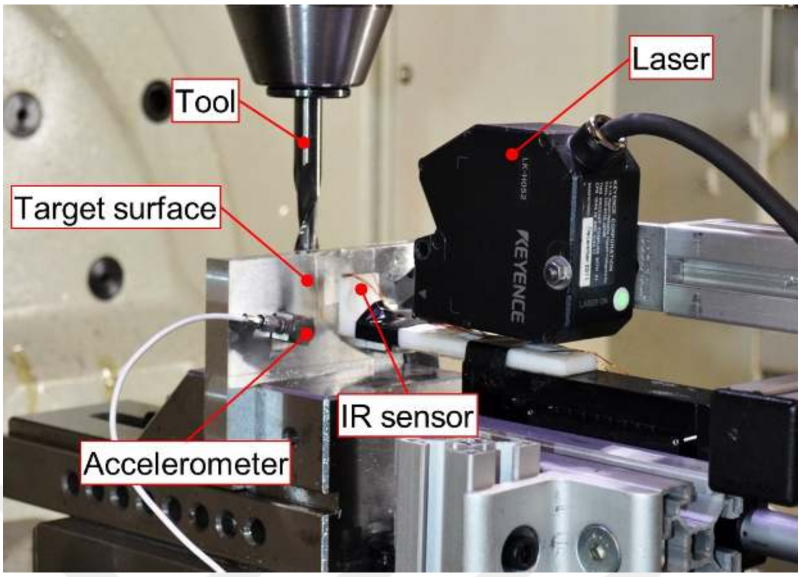

Figure 5.7: Hardware setup for estimation of chatter and workpiece deformation.

is shown in Figure 5.8. The acquired data, as shown in Figure 5.8(a) is processed, and frequencies below 60 Hz are filtered to eliminate powerline frequency content. The filtered signals are then analyzed in the frequency domain by computing the FFT, as illustrated in Figure 5.8(b). The commonly accepted criterion for deciding the occurrence of chatter in milling, i.e., the appearance of frequencies other than the spindle rotation frequency (SRF) and the tooth passing frequency (TPF) in the FFT spectrum, is used to detect chatter. For this purpose, the SRF, TPF, and their harmonics are identified as given in Figure 5.8(c). In the final step, all these known frequencies are removed from the FFT data to identify the presence of any unknown frequencies that can be associated with chatter, as illustrated in Figure 5.8(d). The main objective here is to demonstrate the capability of the IR sensor to capture frequencies other than the known frequencies of an end milling operation corresponding to the no-chatter conditions.

Workpiece deformation

The workpiece deformation is recorded as a change in the voltage of the IR sensor. Therefore, measuring the deformation value of the workpiece requires the calibration

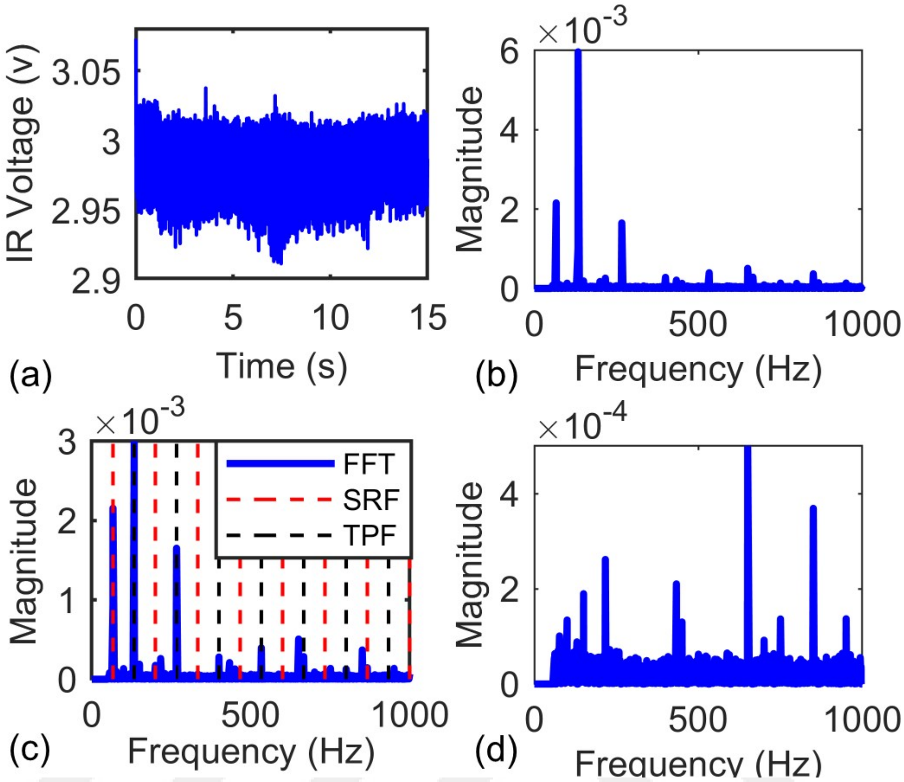

Figure 5.8: Signal processing scheme adopted for chatter estimation.

of voltage values for distance measurements.

Calibration for distance measurement

The hardware setup used for calibrating the IR sensor for distance measurement is shown in Figure 5.9, comprised of a laser and the IR sensor positioned at a specified distance from the target surface. The target comprised a very thin aluminum sheet of thickness 100 μm pasted on a compliant strip fixed at both ends by rigid fixtures on the machine bed. The compliant strip was used to allow easy bending of the target with the applied force. The target surface is incrementally moved in X direction, i.e., towards the sensor, by giving feed movement to the machine spindle. The IR sensor voltage and laser sensor distance corresponding to the initial position of the target, i.e., when the tool is just touching the surface from behind, is set to zero value. The change in voltage of IR voltage and Laser displacement measurements are recorded during the incremental movement of the target surface at a sampling rate of 10 kHz. The data is recorded during both forward and backward movement of the target surface. A total of 12 experiments were performed with an incremental spindle

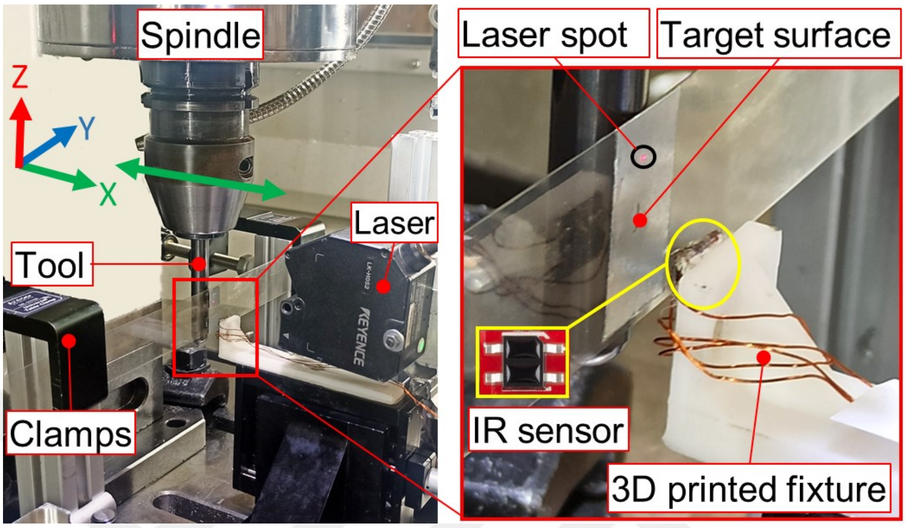

Figure 5.9: Hardware setup for calibration of IR sensor for distance measurement.

speed of 0.5, 1.5, and 2.6 mm/min. A polynomial function is derived between the change in the IR voltage and the distance measured by the laser sensor, as illustrated in Figure 5.10. The correlation function is given in Eq. 5.1, and the coefficient of determination R square value is found to be 0.998.

$$\Delta = av^2 + bv - c \tag{5.1}$$

where, Δ is the measured deflection in micrometers and v is the IR sensor voltage value, a, b, and c are the coefficients of the correlation functions; their values were -477.8, 1612, and -20.42, respectively. The change in the deflection value vs. IR voltage is shown in Figure 5.10. Validation experiments are performed to verify the correlation function; Figure 5.11 shows the comparison of the measurements carried out by IR and laser sensors.

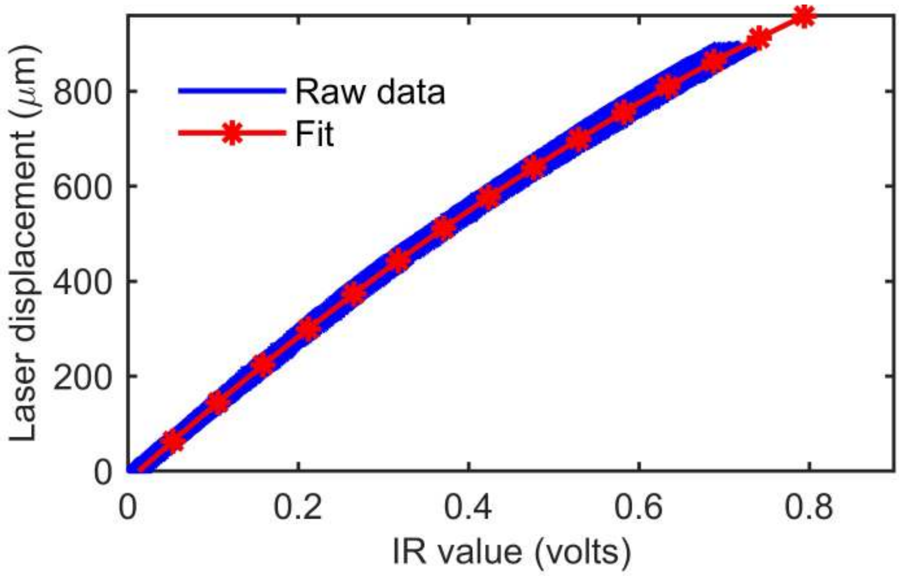

Figure 5.10: Calibration curve of IR sensor.

5.4 Results and discussion

5.4.1 Detection of tool wear

As explained in the methodology section, a comparison of IR sensor signals acquired for wear and non-wear tool conditions is used to detect tool wear. A worn four-fluted endmill having different wear levels at different axial positions was selected for validation of the proposed method. The cutting edges of the used tool had decreasing wear from the tip towards the shank in the axial direction such that the cutting edges at 40 mm from the tip were unworn. The same is depicted in measurements of tool flank wear taken with an optical microscope (Nikon SM-7645) at a_p = 5, 7, 10, 15, 20, and 40 mm, as shown in Figure 5.12. For estimating tool wear using the proposed method, a comparison of IR sensor data acquired at selected a_p values is carried out with the data for the unworn region at a_p = 40 mm, as explained in section 5.2.1. The data is acquired for different a_p values and fragmented into frames corresponding to one complete revolution of the tool having a duration of 60 ms, as shown in Figure 5.13. It is observed that the magnitude of the signal peaks is proportional to the wear levels of the cutting edges, as displayed in

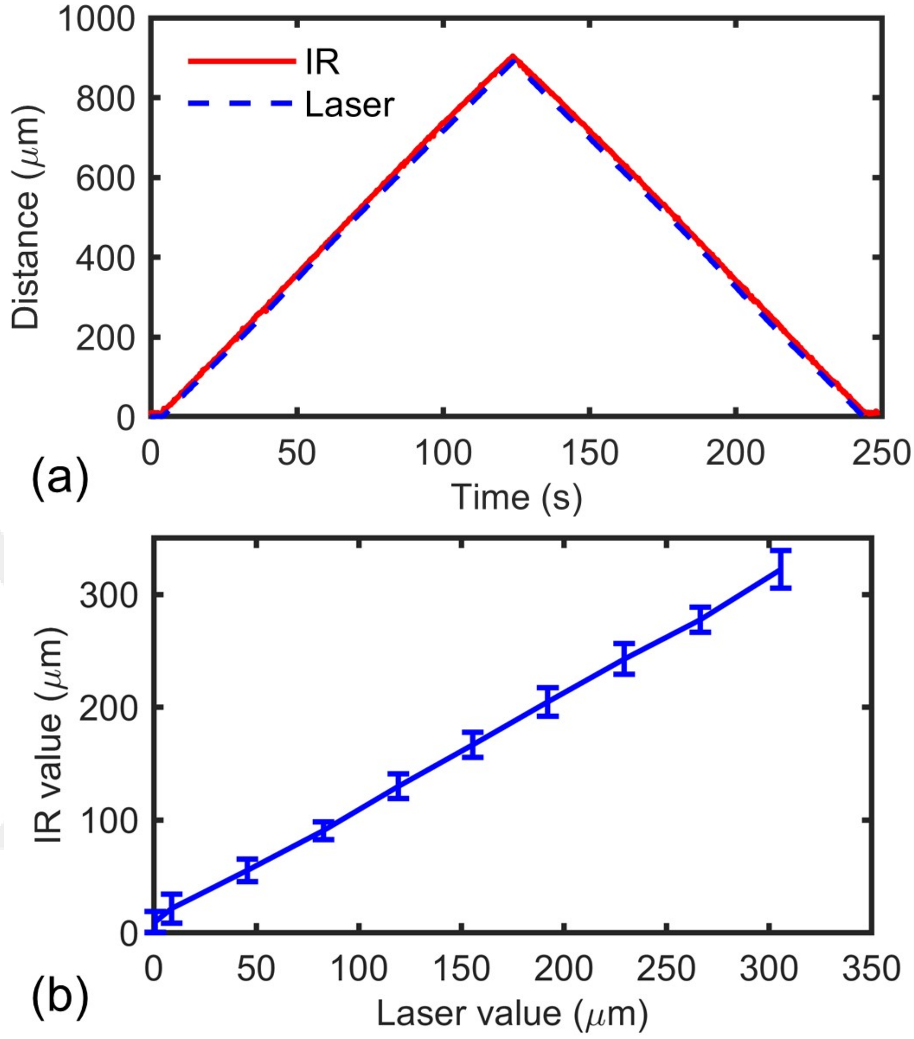

Figure 5.11: Hardware setup for calibration of IR sensor for distance measurement.

microscopic measurements Figure 5.12. To compare relative wear levels, the acquired signals corresponding to different a_p levels are normalized with respect to the signal corresponding to $a_p = 40\ mm$. The normalized values of the voltage signal are shown in Figure 5.13(b) indicate the relative wear of the tool. To analyze the effect of tool wear in the frequency domain, the FFTs of the IR voltage signals corresponding to different a_p were plotted on top of each other, as shown in Figure 5.14. It is seen that the power of the frequencies associated with TPF and SRF is also proportional to the wear levels of the cutting tool.

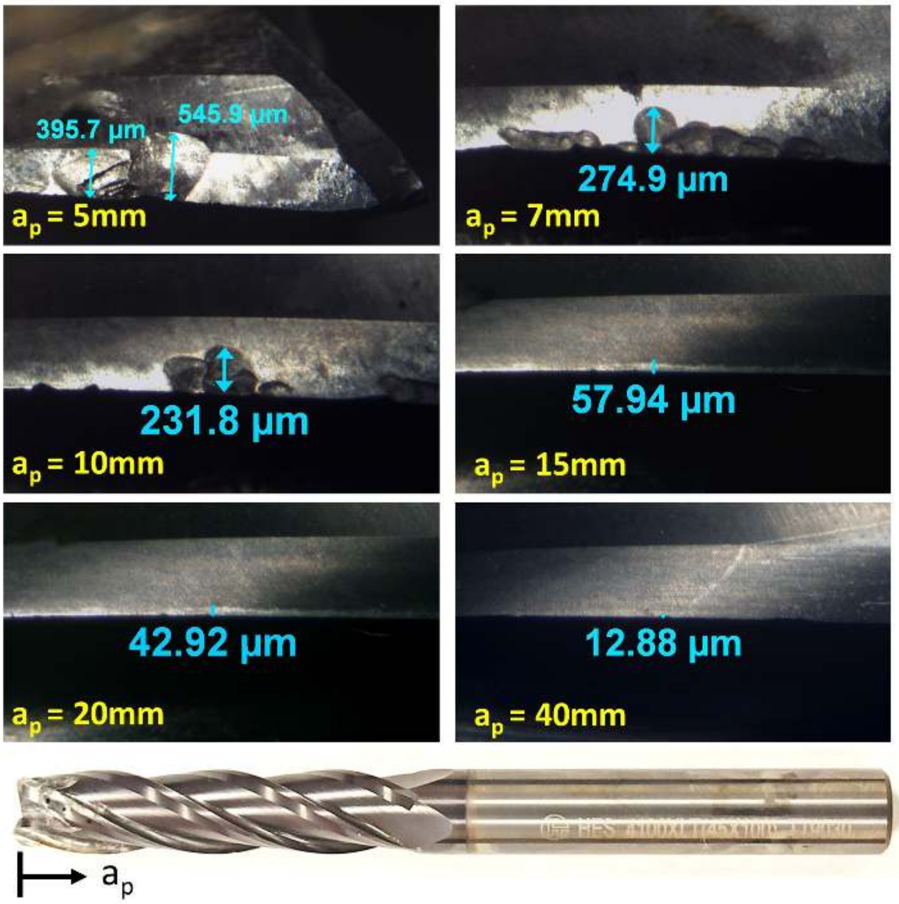

Figure 5.12: Tool wear measurements at different axial depths of cut (a_p).

5.4.2 Detection of chatter

As mentioned in the methodology part, typical vibration data of an end milling process corresponding to the non-chatter case is characterized by the frequencies related to the SRF and TPF. In the case of chatter, other frequencies related to the dynamics of the whole machining system, especially the tool-workpiece region, are also observed. The presence of such frequencies in the machining signal is considered an occurrence of chatter. The chatter detection capability of the IR sensor was validated by identifying the frequencies in the FFT of the sensor signal data acquired during the cutting process. The cutting experiments were performed at different spindle speeds in the range of 2500 – 10000 rpm, whereas the feedrate, axial depth of cut (a_p), and radial depth of cut (a_e) were 480 mm/min, 20 mm, and 1 mm,

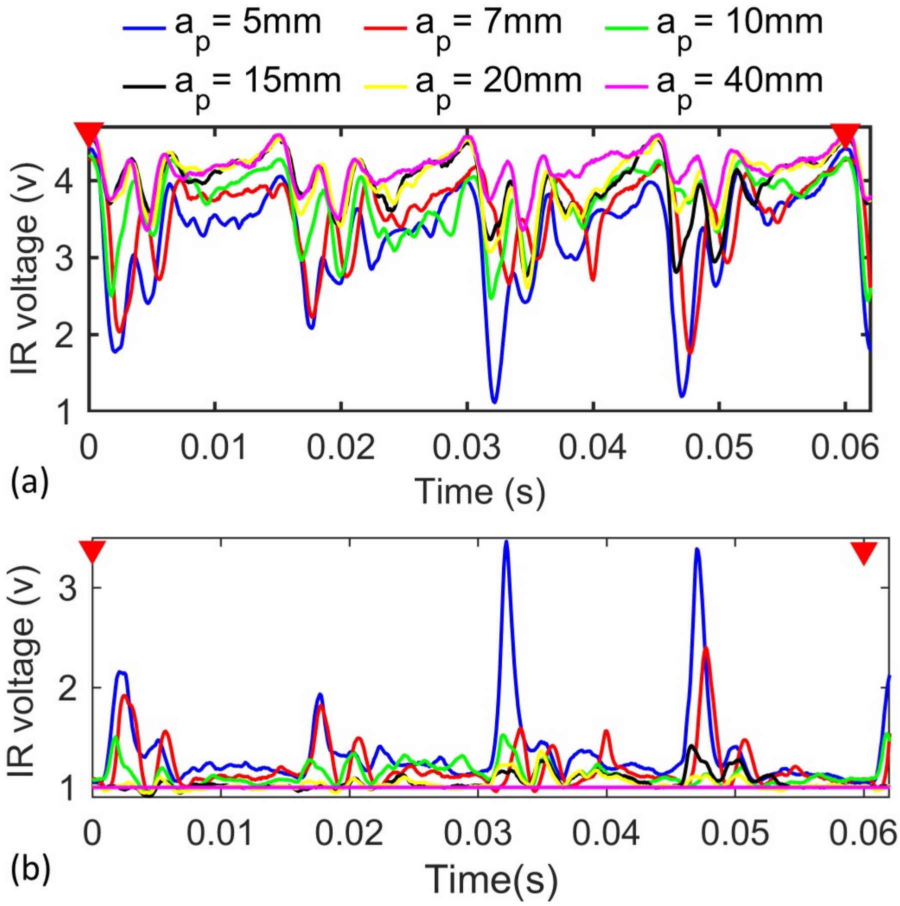

Figure 5.13: Results of tool wear estimation (a) The IR sensor data acquired for one complete tool revolution at defined a_p values. (b) Data normalized with respect to no wear region ($a_p = 40mm$).

respectively. The frequencies in the FFT of the IR sensor signal are compared with those of commercial sensors, i.e., accelerometer and microphone for 10000 rpm, as shown in Figure 5.15. It is observed that the frequencies captured by the IR sensor, as shown in Figure 5.15(b) are the same as those detected by the accelerometer or the microphone sensor in Figure 5.15(a&c) respectively. Figure 5.16 shows FFTs of the IR sensor and accelerometer data corresponding to the non-chatter case at 4000 rpm. After filtering the known non-chatter related frequencies, i.e., SRF and TPF, the plots of FFT for both the accelerometer and IR sensor do not show any other frequencies.

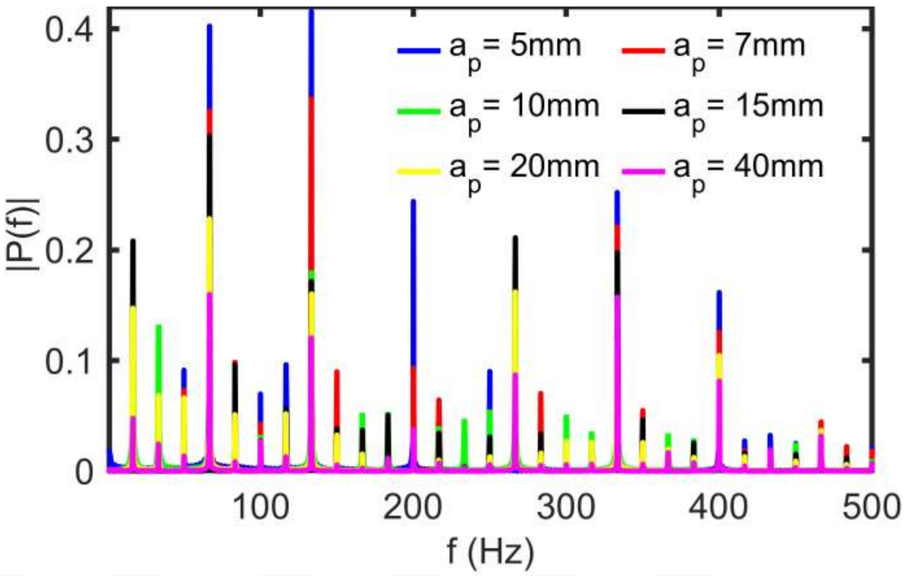

Figure 5.14: Combined plot of the FFT for tool wear estimation at defined a_p values.

5.4.3 Measurement of part deformations

Validation of IR sensor measurements for part deformations was carried out by measuring the deflection of the workpiece during machining using the laser sensor, as shown in Figure 5.17. The cutting experiments were performed at different cutting speeds (V) of 125.6 – 314 m/min whereas feedrate, axial cut depth, and radial cut depth were kept the same at 480 mm/min, 20 mm and 1 mm respectively. Figure 5.18 illustrates the measured dynamic deflection of the workpiece carried out using the introduced IR sensor and the laser displacement sensor. The comparison plots validate the accuracy and sensitivity of the IR sensor for the measurement of dynamic and static deformations. The difference in the value of deformation measurement was found to be in the range of 10 - 15 μm. This difference in the magnitude and profile of deflection measurement is due to the difference in the target positions of these two sensors on the workpiece wall. The laser sensor was targeted on the workpiece wall at a horizontal distance of 7 mm from the target location of the IR sensor due to the physical limitations of the setup as shown in Figure 5.17.

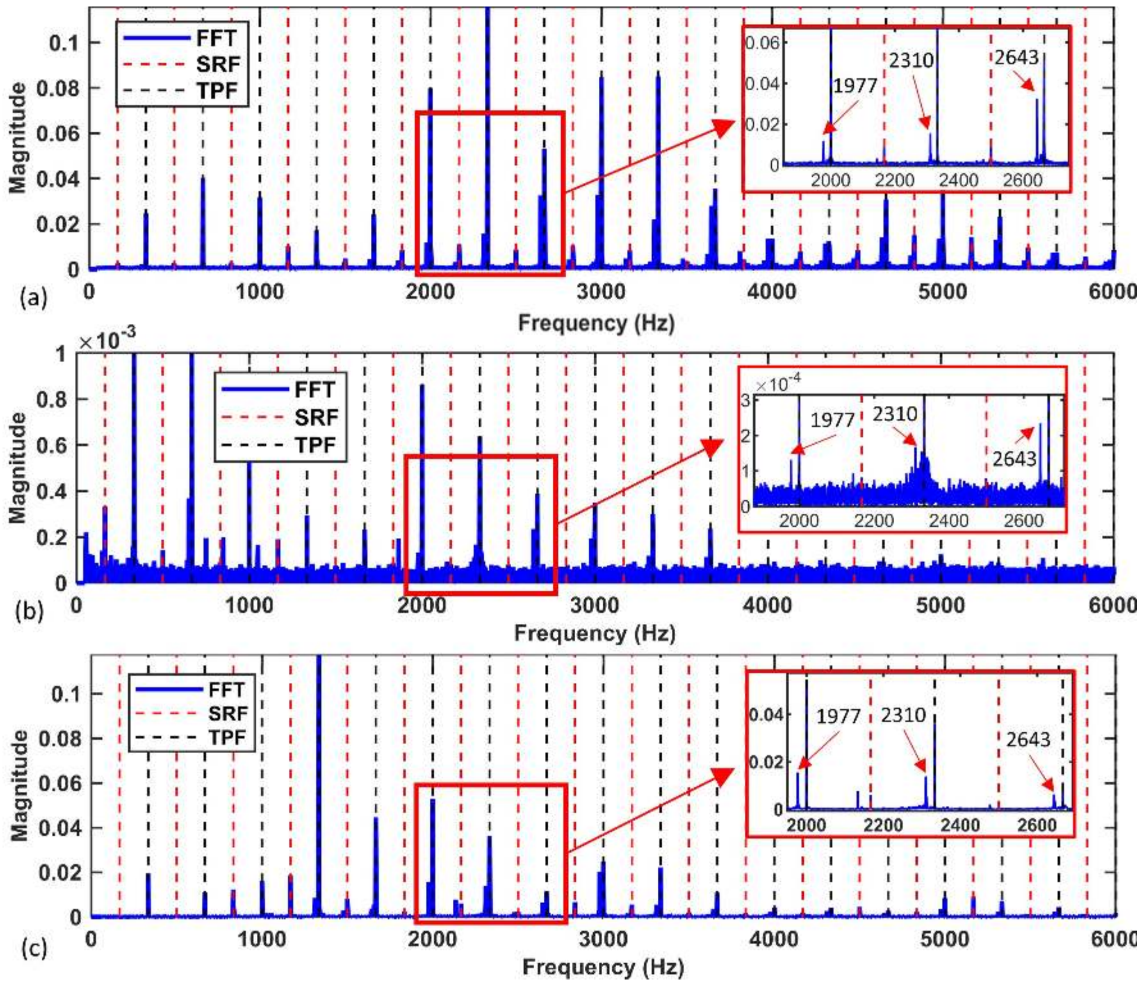

Figure 5.15: FFT comparison of sensors for chatter detection. (a) accelerometer, (b) IR sensor, and (c) microphone.

5.5 Summary

Monitoring different machining process attributes is typically accomplished using commercial sensors. This research presents monitoring of machining based on a low-cost infrared sensor. The sensor used in the proposed approach can monitor multiple attributes of the machining process. It is shown by validation experiments that the employed sensor is on par with commercial sensors such as lasers, accelerometers, and microphones for the estimation of tool wear, chatter, and workpiece deformation. Due to the non-contact nature of the utilized sensor, it does not need to be installed on the workpiece or the machine spindle. Furthermore, its low

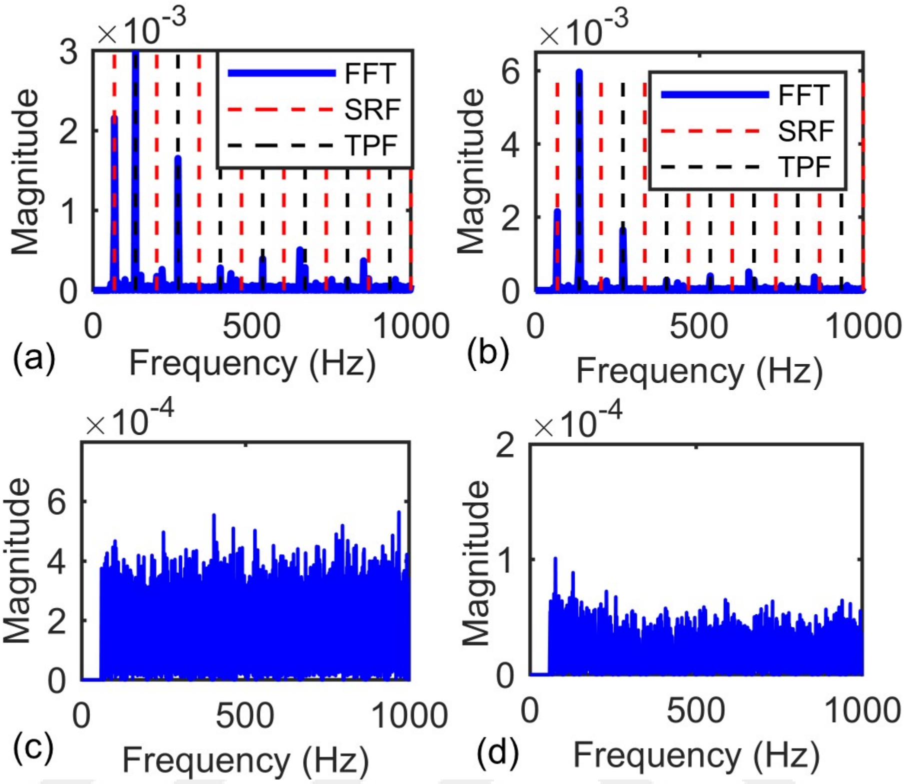

Figure 5.16: Frequency domain analysis of no chatter data. (a) FFT of the accelerometer data, (b) FFT of the IR sensor data, (c) filtered accelerometer data, and (d) filtered IR sensor data.

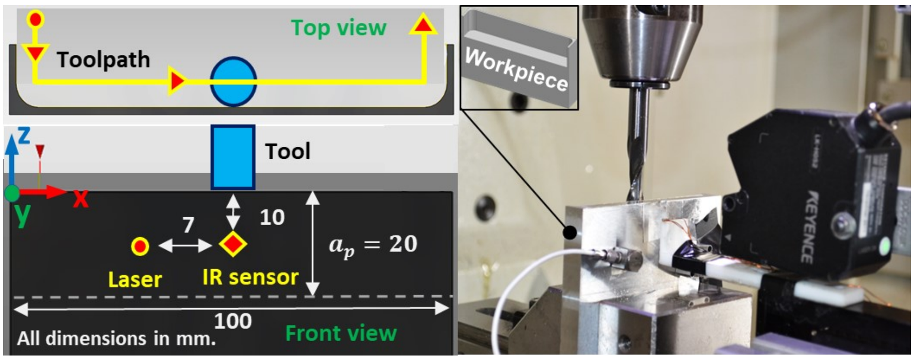

Figure 5.17: Experimental setup for validation of deflection measurement with IR sensor.

cost makes it especially suitable for monitoring multiple aspects of the machining process at different locations of large workpieces, such as structural parts of the aerospace industry.

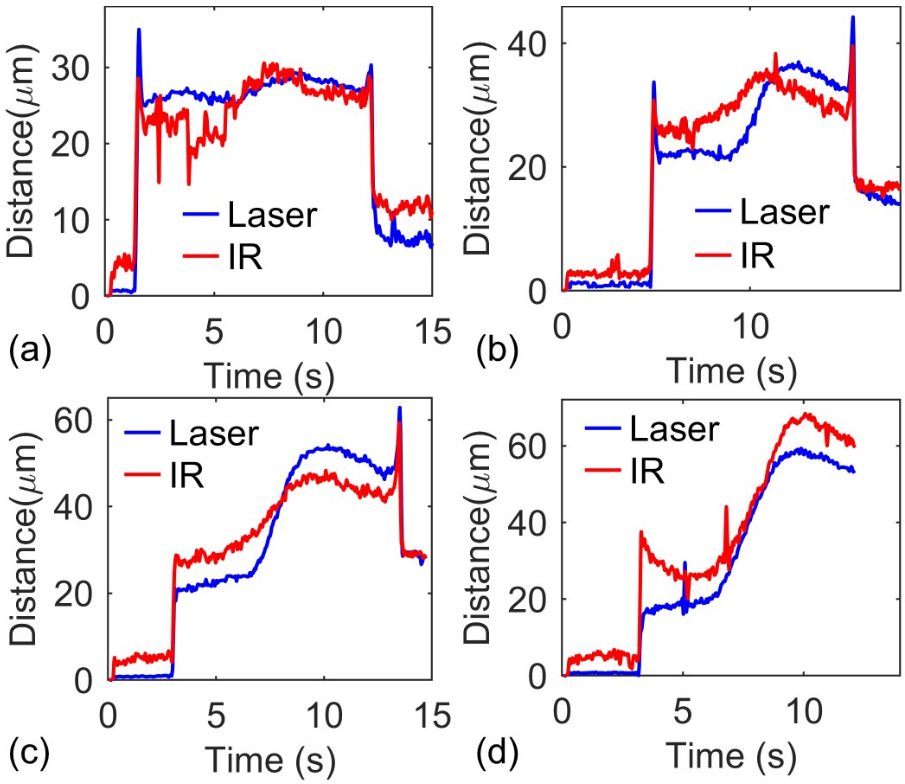

Figure 5.18: Dynamic measurement of part deformation, IR sensor vs Laser. a) $V = 125.6\ m/min$ b) $V = 172.7\ m/min$ c) $V = 219.8\ m/min$ d) $V = 314\ m/min$.

Chapter 6

SYNOPSES AND PERSPECTIVES

The work presented in this dissertation focuses on the problem of distortions of machined parts in the milling process. Different parts of this work address different issues in the modeling, analysis and monitoring of different aspects related to part distortions. New models based on analytical theory, FEM, and hybrid analytical-FEM techniques are proposed to efficiently predict the machining process's various aspects directly affecting the machined parts' distortion. The presented models are validated by performing experiments on commonly employed aerospace materials. The thesis aims to provide accurate tools for predicting part distortions so that proper process planning may be carried out and control measures can be taken. This chapter briefly summarizes the presented approaches, along with their future perspectives.

6.1 State of the art in distortion prediction and control

A detailed literature study is carried out to recognize the most prevalent causes of workpiece distortions in machining. Based on the identified reasons, the available prediction and control models are reviewed, and the strengths and weaknesses of each approach are discussed. Considering the shortcomings of these approaches, guidelines are stated for the improvement of the efficacy of the prediction models.

6.2 Analytical algorithm for the prediction of workpiece temperature in end milling

An efficient and accurate analytical model for predicting the temperature of the workpiece during end milling is proposed. The presented model is based on the oblique cutting mechanics theory and moving heat source models for temperature calculation. The drop in the temperature of the workpiece during non-engagement periods of the cutting tool is calculated by considering the workpiece as a first-order heat transfer system.

The validation experiments are performed on workpieces of Ti6Al4V, an important aerospace alloy. Compared to the tests, the temperature predictions by the model are quite promising. The model duly captures the rise in cutting temperature with the increase in feedrate and the cutting speed due to the increase in the intensity of heat sources. Similarly, the rise in temperature with an increase in radial depth of cut, primarily the result of the increased time constant of the system, is also accurately captured. Due to its analytical character, the proposed algorithm allows fast prediction of workpiece temperature. Further work may be carried out to integrate this temperature calculation algorithm with the algorithms for calculation of machining-induced residual stresses in milling.

6.3 Hybrid model to predict distortions in milling

A hybrid analytical-FEM model is put forth for fast prediction of distortions of milled thin-walled parts of large sizes. Considering the challenges of requirement of extensive computational time and power for machining simulations, a method is devised to precisely calibrate the cutting loads due to the machining process and apply them as moving loads on the surface of the FEM model of the part. The model takes into account the material's initial bulk stresses as well as the machining related boundary conditions.

The proposed approach is validated by performing distortion measurement experiments in milling of a large part of Al 7050-T7451, a common alloy for structural aerospace parts. The validation trial outcomes confirmed the proposed approach's efficacy in predicting the distortion of a large part. Future works may explore the efficacy of the presented model for complex shapes invoving ball end milling operations.

6.4 Machining process monitoring by an infrared sensor

Besides predicting workpiece distortions, monitoring different process attributes may allow for effective control measures to be taken to control these distortions and quality of the machined part in general. Monitoring of different machining process attributes is typically accomplished using commercial sensors. This research presents monitoring of machining based on a low-cost infrared sensor. The sensor data acquired during the machining process is analyzed in the time and frequency domain to characterize the various aspects of the process. The sensor used in the proposed approach can monitor multiple attributes of the machining process.

The efficacy of the proposed approach is validated by performing machining experiments on sample parts. It is shown by validation experiments that the employed sensor is on par with commercial sensors such as lasers, accelerometers, and microphones for the estimation of tool wear, chatter, and workpiece deformation. Due to the non-contact nature of the utilized sensor, it does not need to be installed on the workpiece or the machine spindle. Furthermore, its low cost makes it especially suitable for monitoring multiple aspects of the machining process at different locations of large workpieces, such as structural parts of the aerospace industry. Future works on the subject may include using the proposed method for online monitoring as well as control of the machining process using machine learning and artificial intelligence technologies.

BIBLIOGRAPHY

[1] S. Nervi, "A mathematical model for the estimation of the effects of residual stresses in aluminum plates," Ph.D. dissertation, Washington University in Saint Louis, Missouri, Jul. 2005.

[2] Y. Haichao, Q. Guohua, W. Huamin, Z. Dunwen, and H. Xiong, "A machining position optimization approach to workpiece deformation control for aeronautical monolithic components," *International Journal of Advanced Manufacturing Technology*, vol. 109, no. 1-2, pp. 299–313, 2020.

[3] D. Chantzis, S. Van-Der-Veen, J. Zettler, and W. M. Sim, "An industrial workflow to minimise part distortion for machining of large monolithic components in aerospace industry," *Procedia CIRP*, vol. 8, pp. 281–286, 2013. [Online]. Available: http://dx.doi.org/10.1016/j.procir.2013.06.103

[4] Z. Zhang, L. Li, Y. Yang, N. He, and W. Zhao, "Machining distortion minimization for the manufacturing of aeronautical structure," *International Journal of Advanced Manufacturing Technology*, vol. 73, no. 9-12, pp. 1765–1773, 2014.

[5] S. Dreier and B. Denkena, "Determination of residual stresses in plate material by layer removal with machine-integrated measurement," *Procedia CIRP*, vol. 24, no. C, pp. 103–107, 2014. [Online]. Available: http://dx.doi.org/10.1016/j.procir.2014.07.137

[6] L. D'Alvise, D. Chantzis, B. Schoinochoritis, and K. Salonitis, "Modelling of part distortion due to residual stresses relaxation: An aeronautical case study," *Procedia CIRP*, vol. 31, pp. 447–452, 2015. [Online]. Available: http://dx.doi.org/10.1016/j.procir.2015.03.069

[7] X. Cerutti and K. Mocellin, "Parallel finite element tool to predict distortion induced by initial residual stresses during machining of aeronautical parts," *International Journal of Material Forming*, vol. 8, no. 2, pp. 255–268, 2015.

[8] W. Saleem, H. Ijaz, M. Zain-ul Abdein, A. A. Taimoor, and Y. Wang, "Studying control strategies for dimensional precision in aerospace parts machining," *International Journal of Precision Engineering and Manufacturing*, vol. 18, no. 1, pp. 39–47, 2017.

[9] M. Werke, A. Wretland, P. Ottosson, J. Holmberg, M. Machens, and D. Semere, "Geometric distortion analysis using a combination of the contour method and machining simulation," *Procedia CIRP*, vol. 72, pp. 1481–1486, 2018. [Online]. Available: https://doi.org/10.1016/j.procir.2018.03.213

[10] X. LI, L. LI, Y. YANG, G. ZHAO, N. HE, X. DING, Y. SHI, L. FAN, H. LAN, and M. JAMIL, "Machining deformation of single-sided component based on finishing allowance optimization," *Chinese Journal of Aeronautics*, vol. 33, no. 9, pp. 2434–2444, 2020. [Online]. Available: https://doi.org/10.1016/j.cja.2019.09.015

[11] A. E. Rodríguez-Sánchez, E. Ledesma-Orozco, and S. Ledesma, "Part distortion optimization of aluminum-based aircraft structures using finite element modeling and artificial neural networks," *CIRP Journal of Manufacturing Science and Technology*, vol. 31, pp. 595–606, 2020.

[12] X. Huang, J. Sun, and J. Li, "Finite element simulation and experimental investigation on the residual stress-related monolithic component deformation," *International Journal of Advanced Manufacturing Technology*, vol. 77, no. 5-8, pp. 1035–1041, 2015.

[13] M. Gulpak, J. Sölter, and E. Brinksmeier, "Prediction of shape deviations in face milling of steel," *Procedia CIRP*, vol. 8, pp. 15–20, 2013. [Online]. Available: http://dx.doi.org/10.1016/j.procir.2013.06.058

[14] S. Masoudi, S. Amini, E. Saeidi, and H. Eslami-Chalander, "Effect of machining-induced residual stress on the distortion of thin-walled parts," *International Journal of Advanced Manufacturing Technology*, vol. 76, no. 1-4, pp. 597–608, 2014.

[15] C. Yao, J. Zhang, M. Cui, L. Tan, and X. Shen, "Machining deformation prediction of large fan blades based on loading uneven residual stress," *International Journal of Advanced Manufacturing Technology*, vol. 107, no. 9-10, pp. 4345–4356, 2020.

[16] J. K. Rai and P. Xirouchakis, "Finite element method based machining simulation environment for analyzing part errors induced during milling of thin-walled components," *International Journal of Machine Tools and Manufacture*, vol. 48, no. 6, pp. 629–643, 2008.

[17] H. Guo, D. W. Zuo, H. B. Wu, F. Xu, and G. Q. Tong, "Prediction on milling distortion for aero-multi-frame parts," *Materials Science and Engineering A*, vol. 499, no. 1-2, pp. 230–233, 2009.

[18] S. Jayanti, D. Ren, E. Erickson, S. Usui, T. Marusich, K. Marusich, and H. Elanvogan, "Predictive modeling for tool deflection and part distortion of large machined components," *Procedia CIRP*, vol. 12, pp. 37–42, 2013. [Online]. Available: http://dx.doi.org/10.1016/j.procir.2013.09.008

[19] Z. T. Tang, T. Yu, L. Q. Xu, and Z. Q. Liu, "Machining deformation prediction for frame components considering multifactor coupling effects," *International Journal of Advanced Manufacturing Technology*, vol. 68, no. 1-4, pp. 187–196, 2013.

[20] X. Jiang, Y. Wang, Z. Ding, and H. Li, "An approach to predict the distortion of thin-walled parts affected by residual stress during the milling process," *International Journal of Advanced Manufacturing Technology*, vol. 93, no. 9-12, pp. 4203–4216, 2017.

[21] Z. Wang, J. Sun, W. Chen, L. Liu, and R. Wang, "Machining distortion of titanium alloys aero engine case based on the energy principles," *Metals*, vol. 8, no. 6, 2018.

[22] Z. Zhang, M. Luo, K. Tang, and D. Zhang, "A new in-processes active control method for reducing the residual stresses induced deformation of thin-walled parts," *Journal of Manufacturing Processes*, vol. 59, no. November 2019, pp. 316–325, 2020. [Online]. Available: https://doi.org/10.1016/j.jmapro.2020.09.079

[23] S. Ratchev, S. Ã. Liu, W. Huang, and A. A. Becker, "Milling error prediction and compensation in machining of low-rigidity parts," *International Journal of Machine Tools & Manufacture*, vol. 44, pp. 1629–1641, 2004.

[24] S. Ratchev, S. Liu, and A. A. Becker, "Error compensation strategy in milling flexible thin-wall parts," *Journal of Materials Processing Technology*, vol. 162-163, pp. 673–681, 2005.

[25] W. Chen, J. Xue, D. Tang, H. Chen, and S. Qu, "Deformation prediction and error compensation in multilayer milling processes for thin-walled parts," *International Journal of Machine Tools and Manufacture*, vol. 49, no. 11, pp. 859–864, 2009. [Online]. Available: http://dx.doi.org/10.1016/j.ijmachtools.2009.05.006

[26] Y. yuan Gao, J. wei Ma, Z. yuan Jia, F. ji Wang, L. kun Si, and D. ning Song, "Tool path planning and machining deformation compensation in high-speed milling for difficult-to-machine material thin-walled parts with curved surface," *International Journal of Advanced Manufacturing Technology*, vol. 84, no. 9-12, pp. 1757–1767, 2016. [Online]. Available: http://dx.doi.org/10.1007/s00170-015-7825-4

[27] L. Si-meng, S. Xiao-dong, G. Xiao-bo, and W. Dou, "Simulation of the deformation caused by the machining cutting force on thin-walled deep cavity

parts," *International Journal of Advanced Manufacturing Technology*, vol. 92, no. 9-12, pp. 3503–3517, 2017.

[28] C. Yue, Z. Chen, S. Y. Liang, H. Gao, and X. Liu, "Modeling machining errors for thin-walled parts according to chip thickness," *International Journal of Advanced Manufacturing Technology*, vol. 103, no. 1-4, pp. 91–100, 2019.

[29] X. Hao, Y. Li, M. Li, and C. Liu, "A part deformation control method via active pre-deformation based on online monitoring data," *International Journal of Advanced Manufacturing Technology*, vol. 104, no. 5-8, pp. 2681–2692, 2019.

[30] A. Agarwal and K. Desai, "Tool and Workpiece Deflection Induced Flatness Errors in Milling of Thin-walled Components," *Procedia CIRP*, vol. 93, pp. 1411–1416, 2020. [Online]. Available: https://doi.org/10.1016/j.procir.2020.04.101

[31] Q. Song, Z. Liu, and X. Ai, "Influence of chatter on machining distortion for thin-walled component peripheral milling," *Advances in Mechanical Engineering*, vol. 2014, 2014.

[32] C. Liu, Y. Li, and X. Hao, "An adaptive machining approach based on in-process inspection of interim machining states for large-scaled and thin-walled complex parts," *International Journal of Advanced Manufacturing Technology*, vol. 90, no. 9-12, pp. 3119–3128, 2017.

[33] A. Agarwal and K. Desai, "Amalgamation of Physics-Based Cutting Force Model and Machine Learning Approach for End Milling Operation," *Procedia CIRP*, vol. 93, pp. 1405–1410, 2020. [Online]. Available: https://doi.org/10.1016/j.procir.2020.04.102

[34] Z. Zhao, Y. Li, C. Liu, and J. Gao, "On-line part deformation prediction based

on deep learning," *Journal of Intelligent Manufacturing*, vol. 31, no. 3, pp. 561–574, 2020. [Online]. Available: https://doi.org/10.1007/s10845-019-01465-0

[35] S. Nervi and B. A. Szabó, "On the estimation of residual stresses by the crack compliance method," *Computer Methods in Applied Mechanics and Engineering*, vol. 196, no. 37-40 SPEC. ISS., pp. 3577–3584, 2007.

[36] G. S. Schajer, Ed., *The Slitting Method*, 1st ed. John Wiley & Sons, Ltd., 2013.

[37] J. H. D.M. Bowden, "Aluminium reliability improvement program-final report 60606. Chicago, IL, USA: The Boeing Company." 2001.

[38] W. Akhtar, I. Lazoglu, and S. Y. Liang, "Prediction and control of residual stress-based distortions in the machining of aerospace parts: A review," *Journal of Manufacturing Processes*, vol. 76, no. March 2021, pp. 106–122, 2022. [Online]. Available: https://doi.org/10.1016/j.jmapro.2022.02.005

[39] Y. Wei and X. W. Wang, "Computer simulation and experimental study of machining deflection due to original residual stress of aerospace thin-walled parts," *International Journal of Advanced Manufacturing Technology*, vol. 33, no. 3-4, pp. 260–265, 2007.

[40] W.-m. Sim, "Residual Stress Engineering in Manufacture of Aerospace Structural Parts," in *3rd International Conference on distorsions engineering*, 2011, pp. 187–194.

[41] Z. Zhang, D. Zhang, M. Luo, and B. Wu, "A novel in-process machining deformation perception and control method," *IEEE/ASME International Conference on Advanced Intelligent Mechatronics, AIM*, vol. 2019-July, pp. 685–690, 2019.

[42] H. chuan Song, Y. du Zhang, Q. Wu, and H. jun Gao, "Low-stiffness spring element constraint boundary condition method for machining deformation simulation," *Journal of Mechanical Science and Technology*, vol. 34, no. 10, 2020.

[43] M. Casuso, R. Polvorosa, F. Veiga, A. Suárez, and A. Lamikiz, "Residual stress and distortion modeling on aeronautical aluminum alloy parts for machining sequence optimization," *International Journal of Advanced Manufacturing Technology*, vol. 110, no. 5-6, pp. 1219–1232, 2020.

[44] I. Llanos, J. L. Lanzagorta, and A. Beristain, "Part Distortion Modeling on Aluminum Slender Structural Components for Aeronautical Industry," *Procedia CIRP*, vol. 58, pp. 158–162, 2017. [Online]. Available: http://dx.doi.org/10.1016/j.procir.2017.03.213

[45] H. Gao, Y. Zhang, Q. Wu, and B. Li, "Investigation on influences of initial residual stress on thin-walled part machining deformation based on a semi-analytical model," *Journal of Materials Processing Technology*, vol. 262, no. March, pp. 437–448, 2018. [Online]. Available: https://doi.org/10.1016/j.jmatprotec.2018.04.009

[46] Z. Chen, C. Yue, Y. Xu, X. Liu, and S. Y. Liang, "An analytical machining deformation model of H-section multi-frame beam integral components," *Journal of Materials Processing Technology*, vol. 314, no. November 2022, p. 117907, 2023. [Online]. Available: https://doi.org/10.1016/j.jmatprotec.2023.117907

[47] N. P. Xue, Q. Wu, R. S. Yang, H. J. Gao, Z. Zhang, Y. D. Zhang, L. Li, and J. Guo, "Research on machining deformation of aluminum alloy rolled ring induced by residual stress," *International Journal of Advanced Manufacturing Technology*, vol. 125, no. 11-12, pp. 5669–5680, 2023. [Online]. Available: https://doi.org/10.1007/s00170-023-11068-y

[48] R. Bilkhu, S. Ayvar-Soberanis, C. Pinna, and T. McLeay, "Machining distortion in asymmetrical residual stress profiles," *Procedia CIRP*, vol. 82, pp. 395–399, 2019. [Online]. Available: https://doi.org/10.1016/j.procir.2019.04.346

[49] I. Cherif, J. Outeiro, D. Cotton, G. Poulachon, G. Charrondiere, and A. Brosse, "Effects of toolpath and clamping strategies in machining distortion of stainless-steel parts," *Procedia CIRP*, vol. 82, pp. 427–431, 2019. [Online]. Available: https://doi.org/10.1016/j.procir.2019.04.065

[50] L. Barcenas, E. Ledesma-Orozco, S. Van-der Veen, F. Reveles-Arredondo, and E. A. Rodríguez-Sánchez, "An optimization of part distortion for a structural aircraft wing rib: an industrial workflow approach," *CIRP Journal of Manufacturing Science and Technology*, vol. 28, pp. 15–23, 2020.

[51] J. GUO, H. FU, B. PAN, and R. KANG, "Recent progress of residual stress measurement methods: A review," *Chinese Journal of Aeronautics*, vol. 34, no. 2, pp. 54–78, 2021. [Online]. Available: https://doi.org/10.1016/j.cja.2019.10.010

[52] A. M. Pardowska, J. W. H. Price, and T. R. Finlayson, "Efficient use of available techniques to measure residual stresses in welded components ." *Int. Workshop on Thermal Forming and Welding Distortion (IWOTE08)*, pp. 1–12, 2008.

[53] M. Aurrekoetxea, L. N. López de Lacalle, O. Zelaieta, and I. Llanos, "Uncertainty Assessment for Bulk Residual Stress Characterization Using Layer Removal Method," *Experimental Mechanics*, vol. 63, no. 2, pp. 323–335, 2023. [Online]. Available: https://doi.org/10.1007/s11340-022-00918-7

[54] J. P. Davim, Ed., *Surface Integrity in Machining*. London: Springer, 2010.

[55] D. Ulutan, B. Erdem Alaca, and I. Lazoglu, "Analytical modelling of residual stresses in machining," *Journal of Materials Processing Technology*, vol. 183, no. 1, pp. 77–87, 2007.

[56] I. Lazoglu, D. Ulutan, B. E. Alaca, S. Engin, and B. Kaftanoglu, "An enhanced analytical model for residual stress prediction in machining," *CIRP Annals - Manufacturing Technology*, vol. 57, no. 1, pp. 81–84, 2008.

[57] W. Akhtar, J. Sun, and W. Chen, "Effect of Machining Parameters on Surface Integrity in High Speed Milling of Super Alloy GH4169/Inconel 718," *Materials and Manufacturing Processes*, vol. 31, no. 5, pp. 620–627, 2016. [Online]. Available: http://dx.doi.org/10.1080/10426914.2014.994769

[58] B. Denkena, C. Schmidt, and M. Krüger, "Experimental investigation and modeling of thermal and mechanical influences on shape deviations in machining structural parts," *International Journal of Machine Tools and Manufacture*, vol. 50, no. 11, pp. 1015–1021, 2010.

[59] E. Brinksmeier and J. Sölter, "Prediction of shape deviations in machining," *CIRP Annals - Manufacturing Technology*, vol. 58, no. 1, pp. 507–510, 2009.

[60] D. Ulutan and T. Ozel, "Machining induced surface integrity in titanium and nickel alloys: A review," *International Journal of Machine Tools and Manufacture*, vol. 51, no. 3, pp. 250–280, 2011. [Online]. Available: http://dx.doi.org/10.1016/j.ijmachtools.2010.11.003

[61] Z. Zhang, Z. Zhang, D. Zhang, and M. Luo, "Milling distortion prediction for thin-walled component based on the average MIRS in specimen machining," *The International Journal of Advanced Manufacturing Technology*, vol. 111, no. 11, pp. 3379–3392, 2020. [Online]. Available: https://doi.org/10.1007/s00170-020-06281-y

[62] L. Gang, "Study on deformation of titanium thin-walled part in milling process," *Journal of Materials Processing Technology*, vol. 209, no. 6, pp. 2788–2793, 2009.

[63] Y. Yang, M. Li, and K. R. Li, "Comparison and analysis of main effect elements of machining distortion for aluminum alloy and titanium alloy aircraft monolithic component," *International Journal of Advanced Manufacturing Technology*, vol. 70, no. 9-12, pp. 1803–1811, 2014.

[64] Z. Zhang, L. Wang, S. Wang, D. Zhang, and A. Jiang, "A novel deflection control method for the asymmetric thin-walled component by optimizing the feed rate of the finishing process," *International Journal of Advanced Manufacturing Technology*, pp. 3385–3395, 2023. [Online]. Available: https://doi.org/10.1007/s00170-023-11718-1

[65] O. Karsten, C. Grote, K. Schimanski, A. V. Hehl, and H.-w. Zoch, "Optimized Processing for Distortion Control in Milling of Al-Zn-Mg Alloys," in *Proceedings of the 12th International Conference on Aluminium Alloys*. Yokohama, Japan: The Japan Institute of Light Metals, 2010, pp. 1261–1266.

[66] B. Toubhans, F. Viprey, G. Fromentin, H. Karaouni, and T. Dorlin, "Study of phenomena responsible for part distortions when turning thin Inconel 718 workpieces," *Journal of Manufacturing Processes*, vol. 61, no. August 2020, pp. 46–55, 2021.

[67] A. Hussain and I. Lazoglu, "Distortion in milling of structural parts," *CIRP Annals - Manufacturing Technology*, vol. 68, no. 1, pp. 105–108, 2019. [Online]. Available: https://doi.org/10.1016/j.cirp.2019.04.053

[68] I. Lazoglu and A. Mamedov, "Deformation of thin parts in micromilling," *CIRP Annals - Manufacturing Technology*, vol. 65, no. 1, pp. 117–120, 2016. [Online]. Available: http://dx.doi.org/10.1016/j.cirp.2016.04.077

[69] O. Fergani, A. Mamedov, I. Lazoglu, J. G. Yang, and S. Y. Liang, "Prediction of residual stress induced distortions in micro-milling of Al7050 thin plate," *Applied Mechanics and Materials*, vol. 472, pp. 677–681, 2014.

[70] O. Fergani, I. Lazoglu, A. Mkaddem, M. El Mansori, and S. Y. Liang, "Analytical modeling of residual stress and the induced deflection of a milled thin plate," *International Journal of Advanced Manufacturing Technology*, vol. 75, no. 1-4, pp. 455–463, 2014.

[71] B. ZHAO, W. DING, Z. SHAN, J. WANG, C. YAO, Z. ZHAO, J. LIU, S. XIAO, Y. DING, X. TANG, X. WANG, Y. WANG, and X. WANG, "Collaborative manufacturing technologies of structure shape and surface integrity for complex thin-walled components of aero-engine: Status, challenge and tendency," *Chinese Journal of Aeronautics*, vol. 36, no. 7, pp. 1–24, 2023. [Online]. Available: https://doi.org/10.1016/j.cja.2023.02.008

[72] Z. S. Ma, Y. C. Zhou, S. G. Long, and C. Lu, "Residual stress effect on hardness and yield strength of Ni thin film," *Surface and Coatings Technology*, vol. 207, pp. 305–309, 2012.

[73] M. X. Yang, R. G. Li, P. Jiang, F. P. Yuan, Y. D. Wang, Y. T. Zhu, and X. L. Wu, "Residual stress provides significant strengthening and ductility in gradient structured materials," *Materials Research Letters*, vol. 7, no. 11, pp. 433–438, 2019. [Online]. Available: https://doi.org/10.1080/21663831.2019.1635537

[74] H. Y. Dong and Y. L. Ke, "Study on machining deformation of aircraft monolithic component by FEM and experiment," *Chinese Journal of Aeronautics*, vol. 19, no. 3, pp. 247–254, 2006. [Online]. Available: http://dx.doi.org/10.1016/S1000-9361(11)60352-X

[75] Y. B. Bi, Q. L. Cheng, H. Y. Dong, and Y. L. Ke, "Machining distortion pre-

diction of aerospace monolithic components," *Journal of Zhejiang University: Science A*, vol. 10, no. 5, pp. 661–668, 2009.

[76] B. Li, X. Jiang, J. Yang, and S. Y. Liang, "Effects of depth of cut on the redistribution of residual stress and distortion during the milling of thin-walled part," *Journal of Materials Processing Technology*, vol. 216, pp. 223–233, 2015. [Online]. Available: http://dx.doi.org/10.1016/j.jmatprotec.2014.09.016

[77] X. Huang, J. Sun, and J. Li, "Effect of initial residual stress and machining-induced residual stress on the deformation of aluminium alloy plate," *Strojniski Vestnik/Journal of Mechanical Engineering*, vol. 61, no. 2, pp. 131–137, 2015.

[78] D. Weber, B. Kirsch, C. R. D'Elia, B. S. Linke, M. R. Hill, and J. C. Aurich, "Concept to analyze residual stresses in milled thin walled monolithic aluminum components and their effect on part distortion," in *Proceedings of the 9th Congress of the German Academic Association for Production Technology (WGP)*, J. P. Wulfsberg, W. Hintze, and B.-A. Behrens, Eds. Hamburg: Springer Vieweg, 2019, pp. 287–296.

[79] M. Aurrekoetxea, L. N. L. de Lacalle, and I. Llanos, "Machining stresses and initial geometry on bulk residual stresses characterization by on-machine layer removal," *Materials*, vol. 13, no. 6, 2020.

[80] I. Del Sol, A. Rivero, L. N. L. de Lacalle, and A. J. Gamez, "Thin-wall machining of light alloys: A review of models and industrial approaches," *Materials*, vol. 12, no. 12, 2019.

[81] T. Aijun and L. Zhanqiang, "Deformations of thin-walled plate due to static end milling force," *Journal of Materials Processing Technology*, vol. 206, no. 1-3, pp. 345–351, 2008.

[82] Q. Wu, D. P. Li, L. Ren, and S. Mo, "Detecting milling deformation in 7075 aluminum alloy thin-walled plates using finite difference method," *Interna-*

tional Journal of Advanced Manufacturing Technology, vol. 85, no. 5-8, pp. 1291–1302, 2016.

[83] Z. Du, D. Zhang, H. Hou, and S. Y. Liang, "Peripheral milling force induced error compensation using analytical force model and APDL deformation calculation," *International Journal of Advanced Manufacturing Technology*, vol. 88, no. 9-12, pp. 3405–3417, 2017.

[84] M. Masmali and P. Mathew, "An Analytical Approach for Machining Thin-walled Workpieces," *Procedia CIRP*, vol. 58, pp. 187–192, 2017. [Online]. Available: http://dx.doi.org/10.1016/j.procir.2017.03.186

[85] L. Wang and H. Si, "Machining deformation prediction of thin-walled workpieces in five-axis flank milling," *International Journal of Advanced Manufacturing Technology*, vol. 97, no. 9-12, pp. 4179–4193, 2018.

[86] J. Fei, B. Lin, J. Xiao, M. Ding, S. Yan, X. Zhang, and J. Zhang, "Investigation of moving fixture on deformation suppression during milling process of thin-walled structures," *Journal of Manufacturing Processes*, vol. 32, pp. 403–411, 2018. [Online]. Available: https://doi.org/10.1016/j.jmapro.2018.03.011

[87] B. Li and S. N. Melkote, "Fixture Clamping Force Optimisation and its Impact on Workpiece Location Accuracy," *The International Journal of Advanced Manufacturing Technology*, vol. 17, pp. 104–113, 2001.

[88] M. Aurrekoetxea, I. Llanos, O. Zelaieta, and L. N. López de Lacalle, "Towards advanced prediction and control of machining distortion: a comprehensive review," *International Journal of Advanced Manufacturing Technology*, vol. 122, no. 7-8, pp. 2823–2848, 2022. [Online]. Available: https://doi.org/10.1007/s00170-022-10087-5

[89] R. Radulescu and S. G. Kapoor, "An analytical model for prediction of tool temperature fields during continuous and interrupted cutting," *Journal of*

Manufacturing Science and Engineering, Transactions of the ASME, vol. 116, no. 2, pp. 135–143, 1994.

[90] I. Lazoglu and Y. Altintas, "Prediction of tool and chip temperature in continuous and interrupted machining," *International Journal of Machine Tools and Manufacture*, vol. 42, no. 9, pp. 1011–1022, 2002.

[91] J. Saelzer, S. Berger, I. Iovkov, A. Zabel, and D. Biermann, "In-situ measurement of rake face temperatures in orthogonal cutting," *CIRP Annals*, vol. 69, no. 1, pp. 61–64, 2020. [Online]. Available: https://doi.org/10.1016/j.cirp.2020.04.021

[92] D. K. Aspinwall, A. L. Mantle, W. K. Chan, R. Hood, and S. L. Soo, "Cutting temperatures when ball nose end milling γ-TiAl intermetallic alloys," *CIRP Annals - Manufacturing Technology*, vol. 62, no. 1, pp. 75–78, 2013. [Online]. Available: http://dx.doi.org/10.1016/j.cirp.2013.03.007

[93] A. Byfut and A. Schröder, "A fictitious domain method for the simulation of thermoelastic deformations in NC-milling processes," *International Journal for Numerical Methods in Engineering*, vol. 113, no. 2, pp. 208–229, 2018.

[94] B. Denkena, A. Schmidt, P. Maaß, D. Niederwestberg, C. Niebuhr, and J. Vehmeyer, "Prediction of temperature induced shape deviations in dry milling," *Procedia CIRP*, vol. 31, pp. 340–345, 2015. [Online]. Available: http://dx.doi.org/10.1016/j.procir.2015.03.072

[95] M. Schweinoch, R. Joliet, P. Kersting, and A. Zabel, "Heat input modeling and calibration in dry NC-milling processes," *Production Engineering*, vol. 9, no. 4, pp. 495–504, 2015.

[96] I. Lazoglu and B. Bugdayci, "Thermal modelling of end milling," *CIRP Annals - Manufacturing Technology*, vol. 63, no. 1, pp. 113–116, 2014. [Online]. Available: http://dx.doi.org/10.1016/j.cirp.2014.03.072

[97] C. Islam, I. Lazoglu, and Y. Altintas, "A Three-Dimensional Transient Thermal Model for Machining," *Journal of Manufacturing Science and Engineering, Transactions of the ASME*, vol. 138, no. 2, 2016.

[98] U. Karaguzel, M. Bakkal, E. Budak, and P. M. Putz, "Modeling and measurement of cutting temperatures in milling," in *Procedia CIRP*, vol. 46. Elsevier B.V., 2016, pp. 173–176.

[99] R. Komanduri and Z. B. Hou, "Thermal modeling of the metal cutting process Part I - Temperature rise distribution due to shear plane heat source," *International Journal of Mechanical Sciences*, vol. 42, no. 1, pp. 1715–1752, 2000.

[100] M. Wan, X. Y. Ye, Y. Yang, and W. H. Zhang, "Theoretical prediction of machining-induced residual stresses in three-dimensional oblique milling processes," *International Journal of Mechanical Sciences*, vol. 133, no. September, pp. 426–437, 2017. [Online]. Available: http://dx.doi.org/10.1016/j.ijmecsci.2017.09.005

[101] R. Zhou and W. Yang, "Analytical modeling of residual stress in helical end milling of nickel-aluminum bronze," *The International Journal of Advanced Manufacturing Technology*, vol. 89, pp. 987–996, 2017.

[102] Y. Altintas, *Manufacturing Automation*, 2nd ed. Cambridge University Press, 2012.

[103] S. G. Waldorf, D. J., DeVor, R. E., & Kapoor, "A slip-line field for ploughing during orthogonal cutting," *Journal of Manufacturing Science and Engineering, Transactions of the ASME*, vol. 120, no. November 1998, pp. 693–699, 1998.

[104] G. Johnson, "Residual stress measurements using the contour method," *School of Materials*, vol. Ph.D, p. 244, 2008.

[105] P. Pagliaro, M. B. Prime, J. S. Robinson, B. Clausen, H. Swenson, M. Steinzig, and B. Zuccarello, "Measuring Inaccessible Residual Stresses Using Multiple Methods and Superposition," *Experimental Mechanics*, vol. 51, no. 7, pp. 1123–1134, 2011.

[106] M. B. Prime, "Experimental Procedure for Crack Compliance (Slitting) Measurements of Residual Stress," *Los Alamos National Laboratory*, vol. LA-UR-03-8, pp. 1–6, 2003.

[107] S. Dreier, J. Brüning, and B. Denkena, "Simulation based reduction of residual stress related part distortion," *Material Science and Technology*, vol. 47, no. 8, pp. 710–717, 2016.

[108] A. Madariaga, I. Perez, P. J. Arrazola, R. Sanchez, J. J. Ruiz, and F. J. Rubio, "Reduction of distortions in large aluminium parts by controlling machining-induced residual stresses," *International Journal of Advanced Manufacturing Technology*, vol. 97, no. 1-4, pp. 967–978, 2018.

[109] V. Schulze, P. Arrazola, F. Zanger, and J. Osterried, "Simulation of distortion due to machining of thin-walled components," *Procedia CIRP*, vol. 8, pp. 45–50, 2013. [Online]. Available: http://dx.doi.org/10.1016/j.procir.2013.06.063

[110] W. Akhtar and I. Lazoglu, "A novel analytical algorithm for prediction of workpiece temperature in end milling," *CIRP Annals - Manufacturing Technology*, vol. 71, no. 1, pp. 57–60, 2022. [Online]. Available: https://doi.org/10.1016/j.cirp.2022.03.039

[111] M. B. Prime and M. R. Hill, "Residual stress, stress relief, and inhomogeneity in aluminum plate," *Scripta Materialia*, vol. 46, no. 1, pp. 77–82, 2002.

[112] L. Lu, J. Sun, K. Guo, and J. Li, "Study on the Generation and Redistribution Mechanism of Residual Stress in Bilateral Rolling Correction Process for Thin-Walled Parts," in *International Manufacturing Science and Engineering*

Conference (Vol. 50725, p. V001T02A027). American Society of Mechanical Engineers., 2017.

[113] J. Chen, P. Hu, H. Zhou, J. Yang, J. Xie, Y. Jiang, Z. Gao, and C. Zhang, "Toward Intelligent Machine Tool," *Engineering*, vol. 5, no. 4, pp. 679–690, 2019. [Online]. Available: https://doi.org/10.1016/j.eng.2019.07.018

[114] W. Akhtar, J. Sun, P. Sun, W. Chen, and Z. Saleem, "Tool wear mechanisms in the machining of Nickel based super-alloys: A review," *Frontiers of Mechanical Engineering*, vol. 9, no. 2, pp. 106–119, 2014.

[115] D. Dimla, "Sensor signals for tool-wear monitoring in metal cutting operations—a review of methods," *International Journal of Machine Tools and Manufacture*, vol. 40, no. 8, pp. 1073–1098, 2000. [Online]. Available: http://linkinghub.elsevier.com/retrieve/pii/S0890695599001224

[116] Q. Hou, J. Sun, Z. Lv, P. Huang, G. Song, and C. Sun, "An online tool wear detection system in dry milling based on machine vision," *International Journal of Advanced Manufacturing Technology*, vol. 105, no. 1-4, pp. 1801–1810, 2019.

[117] Z. Li, R. Liu, and D. Wu, "Data-driven smart manufacturing: Tool wear monitoring with audio signals and machine learning," *Journal of Manufacturing Processes*, vol. 48, no. October 2018, pp. 66–76, 2019. [Online]. Available: https://doi.org/10.1016/j.jmapro.2019.10.020

[118] D. R. Salgado and F. J. Alonso, "An approach based on current and sound signals for in-process tool wear monitoring," *International Journal of Machine Tools and Manufacture*, vol. 47, no. 14, pp. 2140–2152, 2007.

[119] W. Huang, Y. Li, X. Wu, and J. Shen, "The wear detection of mill-grinding tool based on acoustic emission sensor," *International Journal of Advanced*

Manufacturing Technology, vol. 124, no. 11-12, pp. 4121–4130, 2023. [Online]. Available: https://doi.org/10.1007/s00170-022-09058-7

[120] Z. Li, X. Liu, A. Incecik, M. K. Gupta, G. M. Królczyk, and P. Gardoni, "A novel ensemble deep learning model for cutting tool wear monitoring using audio sensors," *Journal of Manufacturing Processes*, vol. 79, no. May, pp. 233–249, 2022.

[121] J. H. Zhou, C. K. Pang, Z. W. Zhong, and F. L. Lewis, "Tool wear monitoring using acoustic emissions by dominant-feature identification," *IEEE Transactions on Instrumentation and Measurement*, vol. 60, no. 2, pp. 547–559, 2011.

[122] W. Rmili, A. Ouahabi, R. Serra, and R. Leroy, "An automatic system based on vibratory analysis for cutting tool wear monitoring," *Measurement: Journal of the International Measurement Confederation*, vol. 77, pp. 117–123, 2016. [Online]. Available: http://dx.doi.org/10.1016/j.measurement.2015.09.010

[123] P. Twardowski, J. Czyżycki, A. Felusiak-Czyryca, M. Tabaszewski, and M. Wiciak-Pikuła, "Monitoring and forecasting of tool wear based on measurements of vibration accelerations during cast iron milling," *Journal of Manufacturing Processes*, vol. 95, no. December 2022, pp. 342–350, 2023.

[124] T. Kalvoda and Y. R. Hwang, "A cutter tool monitoring in machining process using Hilbert-Huang transform," *International Journal of Machine Tools and Manufacture*, vol. 50, no. 5, pp. 495–501, 2010. [Online]. Available: http://dx.doi.org/10.1016/j.ijmachtools.2010.01.006

[125] G. Dheeraj Simon and R. Deivanathan, "Early detection of drilling tool wear by vibration data acquisition and classification," *Manufacturing Letters*, vol. 21, pp. 60–65, 2019. [Online]. Available: https://doi.org/10.1016/j.mfglet.2019.08.006

[126] A. Al-Azmi, A. Al-Habaibeh, and J. Abbas, "Sensor fusion and the application of artificial intelligence to identify tool wear in turning operations," *International Journal of Advanced Manufacturing Technology*, pp. 429–442, 2023. [Online]. Available: https://doi.org/10.1007/s00170-023-11113-w

[127] T. Oshida, T. Murakoshi, L. Zhou, H. Ojima, K. Kaneko, T. Onuki, and J. Shimizu, "Development and implementation of real-time anomaly detection on tool wear based on stacked LSTM encoder-decoder model," *International Journal of Advanced Manufacturing Technology*, no. 0123456789, 2023. [Online]. Available: https://doi.org/10.1007/s00170-023-11497-9

[128] P. J. Bagga, B. Chavda, V. Modi, M. A. Makhesana, and K. M. Patel, "Indirect tool wear measurement and prediction using multi-sensor data fusion and neural network during machining," *Materials Today: Proceedings*, vol. 56, pp. 51–55, 2022. [Online]. Available: https://doi.org/10.1016/j.matpr.2021.12.131

[129] P. M. Huang and C. H. Lee, "Estimation of tool wear and surface roughness development using deep learning and sensors fusion," *Sensors*, vol. 21, no. 16, 2021.

[130] W. K. Wang, M. Wan, W. H. Zhang, and Y. Yang, "Chatter detection methods in the machining processes: A review," *Journal of Manufacturing Processes*, vol. 77, no. December 2021, pp. 240–259, 2022. [Online]. Available: https://doi.org/10.1016/j.jmapro.2022.03.018

[131] J. Kim, S. Lee, H. Chun, and C. B. Lee, "Compact curved-edge displacement sensor-embedded spindle system for machining process monitoring," *Journal of Manufacturing Processes*, vol. 64, no. December 2020, pp. 1255–1260, 2021. [Online]. Available: https://doi.org/10.1016/j.jmapro.2021.02.056

[132] Y. Shi, F. Mahr, U. Von Wagner, and E. Uhlmann, "Chatter frequencies of micromilling processes: Influencing factors and online

detection via piezoactuators," *International Journal of Machine Tools and Manufacture*, vol. 56, pp. 10–16, 2012. [Online]. Available: http://dx.doi.org/10.1016/j.ijmachtools.2011.12.001

[133] Z. Zhang, H. Li, G. Meng, X. Tu, and C. Cheng, "Chatter detection in milling process based on the energy entropy of VMD and WPD," *International Journal of Machine Tools and Manufacture*, vol. 108, pp. 106–112, 2016. [Online]. Available: http://dx.doi.org/10.1016/j.ijmachtools.2016.06.002

[134] J. H. Navarro-Devia, Y. Chen, D. V. Dao, and H. Li, *Chatter detection in milling processes—a review on signal processing and condition classification*. Springer London, 2023. [Online]. Available: https://doi.org/10.1007/s00170-023-10969-2

[135] G. Wu, G. Li, W. Pan, I. Raja, X. Wang, and S. Ding, "A state-of-art review on chatter and geometric errors in thin-wall machining processes," *Journal of Manufacturing Processes*, vol. 68, no. June, pp. 454–480, 2021.

[136] M. C. Yesilli, F. A. Khasawneh, and B. P. Mann, "Transfer learning for autonomous chatter detection in machining," *Journal of Manufacturing Processes*, vol. 80, no. October 2021, pp. 1–27, 2022. [Online]. Available: https://doi.org/10.1016/j.jmapro.2022.05.037

[137] E. Rivière-Lorphèvre, V. Stalon, O. Van den Abeele, E. Filippi, and P. Dehombreux, "Chatter detection techniques using microphone," *Seventh national congress on theoretical and applied mechanics 2006*, 2006.

[138] M. Q. Tran, M. K. Liu, and M. Elsisi, "Effective multi-sensor data fusion for chatter detection in milling process," *ISA Transactions*, vol. 125, pp. 514–527, 2022. [Online]. Available: https://doi.org/10.1016/j.isatra.2021.07.005

[139] M. H. Rahimi, H. N. Huynh, and Y. Altintas, "On-line chatter detection in milling with hybrid machine learning and physics-based model," *CIRP*

Journal of Manufacturing Science and Technology, vol. 35, pp. 25–40, 2021. [Online]. Available: https://doi.org/10.1016/j.cirpj.2021.05.006

[140] W. Akhtar and I. Lazoglu, “A novel hybrid model for prediction of distortions in milling,” *CIRP Annals*, vol. 00, pp. 4–7, 2023. [Online]. Available: https://doi.org/10.1016/j.cirp.2023.04.052

[141] E. Li, J. Zhou, C. Yang, J. Zhao, Z. Li, S. Zhang, and M. Wang, “Part machining deformation prediction based on spatial-temporal correlation learning of geometry and cutting loads,” *Journal of Manufacturing Processes*, vol. 92, no. February, pp. 397–411, 2023. [Online]. Available: https://doi.org/10.1016/j.jmapro.2023.02.042

[142] J. Loehe, M. F. Zaeh, and O. Roesch, “In-process deformation measurement of thin-walled workpieces,” *Procedia CIRP*, vol. 1, no. 1, pp. 546–551, 2012. [Online]. Available: http://dx.doi.org/10.1016/j.procir.2012.04.097

[143] I. Lazoglu and A. Mamedov, “Deformation of thin parts in micromilling,” *CIRP Annals - Manufacturing Technology*, vol. 65, no. 1, pp. 117–120, 2016. [Online]. Available: http://dx.doi.org/10.1016/j.cirp.2016.04.077

Appendix A

APPENDIX

A.1 Legendre functions

$$P_1(y) = 2y - 1 \tag{A.1}$$

$$P_2(y) = 6y^2 - 6y + 1 \tag{A.2}$$

$$P_3(y) = (2y - 1)(10y^2 - 10y + 1) \tag{A.3}$$

$$P_4(y) = 70y^4 - 140y^3 + 90y^2 - 20y + 1 \tag{A.4}$$

$$P_5(y) = (2y - 1)(126y^4 - 252y^3 + 154y^2 - 28y + 1) \tag{A.5}$$

$$P_6(y) = 924y^6 - 2772y^5 + 3150y^4 - 1680y^3 + 420y^2 - 42y + 1 \tag{A.6}$$

$$\begin{aligned} P_7(y) =& (2y - 1)(1716y^6 - 5148y^5 + 5742y^4 - 2904y^3 + 648y^2 - \\ & 54y + 1) \end{aligned} \tag{A.7}$$

$$\begin{aligned} P_8(y) =& 12870y^8 - 51480y^7 + 84084y^6 - 72072y^5 + 34650y^4 - 9240y^3 + \\ & 1260y^2 - 72y + 1 \end{aligned} \tag{A.8}$$

$$\begin{aligned} P_9(y) =& (2y - 1)(24310y^8 - 97240y^7 + 157300y^6 - 131560y^5 + \\ & 60346y^4 - 14872y^3 + 1804y^2 - 88y + 1) \end{aligned} \tag{A.9}$$

$$\begin{aligned} P_{10}(y) =& 184756y^{10} - 923780y^9 + 1969110y^8 - 2333760y^7 + \\ & 1681680y^6 - 756756y^5 + 210210y^4 - 34320y^3 + \\ & 2970y^2 - 110y + 1 \end{aligned} \tag{A.10}$$

$$\begin{aligned} P_{11}(y) =& (2y - 1)(352716y^{10} - 1763580y^9 + 3737110y^8 - 4366960y^7 + \\ & 3067480y^6 - 1325116y^5 + 346450y^4 - 52000y^3 + \\ & 4030y^2 - 130y + 1.0) \end{aligned} \tag{A.11}$$

$$\begin{aligned}P_{12}(y) =& 2704156y^{12} - 16224936y^{11} + 42678636y^{10} - 64664600y^{9} + \\ & 62355150y^{8} - 39907296y^{7} + 17153136y^{6} - 4900896y^{5} + \\ & 900900y^{4} - 100100y^{3} + 6006y^{2} - 156y + 1.0\end{aligned} \tag{A.12}$$

$$\begin{aligned}P_{13}(y) =& (2y-1)(5200300y^{12} - 31201800y^{11} + 81748716y^{10} - 122727080y^{9} + \\ & 116464110y^{8} - 72713760y^{7} + 30155280y^{6} - 8201616y^{5} + \\ & 1412700y^{4} - 144500y^{3} + 7830y^{2} - 180y + 1.0\end{aligned} \tag{A.13}$$

$$\begin{aligned}P_{14}(y) =& 40116600y^{14} - 280816200y^{13} + 878850700y^{12} - 1622493600y^{11} + \\ & 1963217256y^{10} - 1636014380y^{9} + 960269310y^{8} - 399072960y^{7} + \\ & 116396280y^{6} - 23279256y^{5} + 3063060y^{4} - 247520y^{3} + \\ & 10920y^{2} - 210y + 1\end{aligned} \tag{A.14}$$

$$\begin{aligned}P_{15}(y) =& (2y-1)(77558760y^{14} - 542911320y^{13} + 1694257740y^{12} - 3107699280y^{11} + \\ & 3719254560y^{10} - 3048415860y^{9} + 1747820830y^{8} - 703674880y^{7} + \\ & 196887880y^{6} - 37351720y^{5} + 4603396y^{4} - 343672y^{3} + 13804y^{2} - \\ & 238y + 1)\end{aligned} \tag{A.15}$$

$$\begin{aligned}P_{16}(y) =& 601080390y^{16} - 4808643120y^{15} + 17450721000y^{14} - 38003792400y^{13} + \\ & 55367594100y^{12} - 56949525360y^{11} + 42536373880y^{10} - 23371634000y^{9} + \\ & 9465511770y^{8} - 2804596080y^{7} + 597500904y^{6} - 88884432y^{5} + 8817900y^{4} - \\ & 542640y^{3} + 18360y^{2} - 272y + 1.0\end{aligned} \tag{A.16}$$